WL-TR-96-4057

THE INTERFEROMETRIC DETECTION OF ULTRAFAST PULSES OF LASER GENERATED ULTRASOUND

by

Curtis Jon Fiedler

A dissertation submitted to the Johns Hopkins University in
conformity with the requirements
for the degree of Doctor of Philosophy

Baltimore, Maryland

1996

FINAL REPORT 1 APRIL 1996

Approved for public release; distribution unlimited

FLIGHT DYNAMICS DIRECTORATE
WRIGHT LABORATORY
AIR FORCE MATERIEL COMMAND
WRIGHT-PATTERSON AIR FORCE BASE, OH 45433-7562

NOTICE

WHEN GOVERNMENT DRAWINGS, SPECIFICATIONS, OR OTHER DATA ARE USED FOR ANY PURPOSE OTHER THAN IN CONNECTION WITH A DEFINITELY GOVERNMENT-RELATED PROCUREMENT, THE UNITED STATES GOVERNMENT INCURS NO RESPONSIBILITY OR ANY OBLIGATION WHATSOEVER. THE FACT THAT THE GOVERNMENT MAY HAVE FORMULATED OR IN ANY WAY SUPPLIED THE SAID DRAWINGS, SPECIFICATIONS, OR OTHER DATA, IS NOT TO BE REGARDED BY IMPLICATION OR OTHERWISE IN ANY MANNER CONSTRUED, AS LICENSING THE HOLDER OR ANY OTHER PERSON OR CORPORATION, OR AS CONVEYING ANY RIGHTS OR PERMISSION TO MANUFACTURE, USE, OR SELL ANY PATENTED INVENTION THAT MAY IN ANY WAY BE RELATED THERETO.

THIS REPORT IS RELEASABLE TO THE NATIONAL TECHNICAL INFORMATION SERVICE (NTIS). AT NTIS, IT WILL BE AVAILABLE TO THE GENERAL PUBLIC, INCLUDING FOREIGN NATIONS.

THIS TECHNICAL REPORT HAS BEEN REVIEWED AND IS APPROVED FOR PUBLICATION.

CURTIS J. FIEDLER, Project Engineer
Nondestructive Evaluation Branch
Metals and Ceramics Division

for TOBEY M. CORDELL, Chief
Nondestructive Evaluation Branch
Metals and Ceramics Division

WALTER M. GRIFFITH, Asst. Chief
Metals and Ceramics Division
Materials Directorate

IF YOUR ADDRESS HAS CHANGED, IF YOU WISH TO BE REMOVED FROM OUR MAILING LIST, OR IF THE ADDRESSEE IS NO LONGER EMPLOYED BY YOUR ORGANIZATION, PLEASE NOTIFY, WL/MLLN, WRIGHT-PATTERSON AFB OH 45433-7817 TO HELP US MAINTAIN A CURRENT MAILING LIST.

COPIES OF THIS REPORT SHOUL.D NOT BE RETURNED UNLESS RETURN IS REQUIRED BY SECURITY CONSIDERATIONS, CONTRACTUAL OBLIGATIONS, OR NOTICE ON A SPECIFIC DOCUMENT.

REPORT DOCUMENTATION PAGE

FORM APPROVED
OMB NO. 0704-0188

1. AGENCY USE ONLY (Leave blank)	2. REPORT DATE	3. REPORT TYPE AND DATES COVERED
	01 APRIL 1996	FINAL 1 APR 1996

4. TITLE AND SUBTITLE
THE INTERFEROMETRIC DETECTION OF ULTRAFAST PULSES OF LASER GENERATED ULTRASOUND

5. FUNDING NUMBERS
PE - 62102F
PR - 2418
TA - 02
WU - 60

6. AUTHOR(S)
CURTIS J. FIEDLER

7. PERFORMING ORGANIZATION NAMES(S) AND ADDRESS(ES)
MATERIAL DIRECTORATE
WRIGHT LABORATORY
AIR FORCE MATERIEL COMMAND
WRIGHT PATTERSON AFB OH 45433-7734

8. PERFORMING ORGANIZATION REPORT NUMBER
WL-TR-96-4057

9. SPONSORING/MONITORING AGENCY NAMES(ES) AND ADDRESS(ES)
MATERIALS DIRECTORATE
WRIGHT LABORATORY
AIR FORCE MATERIEL COMMAND
WRIGHT PATTERSON AIR FORCE BASE OH 45433-7734

10. SPONSORING/MONITORING AGENCY REPORT NUMBER
WL-TR-96-4057

11. SUPPLEMENTARY NOTES

12a. DISTRIBUTION/AVAILABILITY STATEMENT
APPROVED FOR PUBLIC RELEASE; DISTRIBUTION IS UNLIMITED

12b. DISTRIBUTION CODE

13. ABSTRACT (Maximum 200 words)

A novel technique for nondestructively measuring the thickness and properties of thin coatings has been developed. High frequency pulses of ultrasound are generated in a coating using ultrafast (100 fs) pulses of laser light. These ultrasonic pulses are used to inspect thin coatings (30 nm - 500 nm) in a pulse-echo mode. Experimental results demonstrating the interferometer's capabilities are presented. The thickness of a 25 nm gold coating, a 67 nm aluminum coating, and a 170 nm molybdenum coating were measured using ultrasonic echoes. The frequency spectrum of the echoes from the gold coating extented up to 100 GHz for displacements as small as 4 pm. The piezoreflective detection technique is not suitable for materials which are weakly piezoreflective such as gold and molybdenum. The interferometric detection technique, which is not material dependent however, was able to detect multiple ultrasonic echoes in these two materials and therefore extends the utility of ultrafast techniques. The feasibility of this inspection technique for thin coatings has been demonstrated, and there is great potential for this technique to become important tool for characterizing the properties and morphologies of thin coatings.

14. SUBJECT TERMS	15. NUMBER OF PAGES
LASER GENERATED ULTRASOUND, THIN FILMS, NONDESTRUCTIVE INSPECTION, ULTRAFAST PHENOMENA	130
	16. PRICE CODE

17. SECURITY CLASSIFICATION OF REPORT	18. SECURITY CLASSIFICATION OF THIS PAGE	19. SECURITY CLASSIFICATION OF ABSTRACT	20. LIMITATION OF ABSTRACT
UNCLASSIFIED	UNCLASSIFIED	UNCLASSIFIED	SAR

NSN 7540-01-280-5500 COMPUTER GENERATED STANDARD FORM 298 (Rev. 2-89)
Prescribed by ANSI Std. Z39-18
298-102

TABLE OF CONTENTS

LIST OF FIGURES

LIST OF TABLES

ACKNOWLEGEMENTS

I wish to express my thanks to Dr. Wagner for his patient guidance, his visits to Dayton to observe the experiment and offer insight, and, especially for his idea of the delay line based pulsed interferometer.

I also wish to thank Tobey Cordell, Dr. Bob Crane, and Dr. Tom Moran and the Nondestructive Evaluation Branch, Metals and Ceramics Division, Wright-Patterson Materials Directorate, Wright Laboratory, US Air Force for their support and funding. Dr. Pramode Bhagat's advice and insight into instrumentation, and the nature of the signals was very helpful. Dr. Dale Chimenti's inspiration to expand into laser based nondestructive inspection techniques is also appreciated.

I would like to thank Dr. Humphrey Maris, Chris Morath and Guray Tas of Brown University for the gold and arsenic telluride specimens, and also their many helpful discussions. I also want to thank Scott Apt of Universal Energy Systems for the gold-palladium and aluminum specimens, and Peter Shull of Johns Hopkins University for the molybdenum specimens.

David Frink, Dave Fisher, Mike Nelson and Jennifer Foley were very helpful with their patient collection of data and their development of data acquisition routines and display software.

I am also grateful to Dr. Jim Gord of the Propulsion Lab for his assistance with the Ti:Sapphire laser.

Lastly, but most importantly, I wish to express my deepest thanks to my wife Barbara, who assisted with encouragement, trouble shooting and endless hours of proofreading, and to my daughters, Christine and Ingrid, for their patience and support.

1. INTRODUCTION

1.1 Thin Coatings

Thin films are widely used because of their remarkable mechanical, electrical, optical, and other properties. Applications of thin films for their mechanical properties include iridium films for lubricating bearings, titanium nitride and titanium carbide films for lubricating and extending the life of high speed steel tools, and hard carbon films for corrosion resistance. Many resistors, capacitors and inductors use the unique electrical properties of thin films. Semiconducting thin films are used to create diodes, transistors, and integrated circuits. Superconducting thin films are used to create Super-Conducting Quantum Interference Devices (SQUIDS), high speed memory for computers, and Josephson junctions for generating microwaves. Anti-reflection coatings, beam splitters, and anti-laser coatings for cockpit canopies use the unique optical properties of thin films (Eckertova, 1986).

Thin coatings are also crucial to the development new materials. Metal matrix composites, for example, require SCS-6 coatings to transmit loads from the matrix to the titanium fibers. Ceramic matrix composites require thin (100-200 nm) zirconia coatings to transmit loads from the matrix to the sapphire fibers. Carbon-carbon composites will disintegrate instantaneously in high temperature environments if not protected by an anti-oxidation coating. Nanomachines, an emerging technology, will depend on materials made from layers of thin films.

1.2 Thin Film Properties

In each of these applications it is the properties of the thin films which are critical. The mechanical, optical, and electrical properties of coatings typically depend on their thickness. Anti-oxidation coatings and fiber coatings rely on their bonding properties. Superconductive, electrical and optical coatings rely on the conductivity of the films.

The measurement of thin film properties is difficult. Classic inspection techniques measure bulk properties, and since the substrate comprises a much larger percentage of the overall bulk of the material, these techniques measure the properties of the substrate instead of the coating. Techniques to measure elastic properties rely on destructive tests, such as removing the coating from the substrate and placing it in a miniature tension testing machine. The current technique for measuring film adhesion measures the force required to lift the film off the substrate using a piece of Scotch tape (Eckertova, 1986). In addition to being only qualitative, this technique destroys the film in the process.

1.3 The Problem

An inspection technique is required which can nondestructively measure the thickness and elastic properties of thin films. Thin films are defined as optically opaque films ranging in thickness from 10 nm to 1000 nm. "Nondestructive"

implies that, not only is the film not destroyed by removing it from the substrate, but also that it is not contaminated by the inspection.

1.4 Laser Based Ultrasound

An effective way to nondestructively measure elastic properties is to use ultrasonic waves. Conventional methods for measuring elastic properties, such as tensile testing machines, require the removal of the coating from the substrate. Other testing methods, such as radiography and eddy currents do not measure elastic properties. Ultrasonic waves, because they are stress waves, can be used to measure elastic properties.

Conventional ultrasonic tests for thin coatings, such as acoustic microscopes, are not necessarily nondestructive because they require a coupling medium. Many thin coatings need to be contaminant free, and impurities in the coupling medium, or even the coupling medium itself, are enough to ruin the properties of the coating. To be nondestructive, the inspection technique must also be non-contact.

The laser based ultrasound (LBU) technique utilizes the surface of the specimen itself as an ultrasonic transducer, and is thus a non-contact nondestructive inspection method. This technique uses a short pulse of light to rapidly heat the surface of the specimen, and an ultrasonic wave is generated from the induced thermoelastic strain field (White,1963). This is shown schematically in Figure 1.

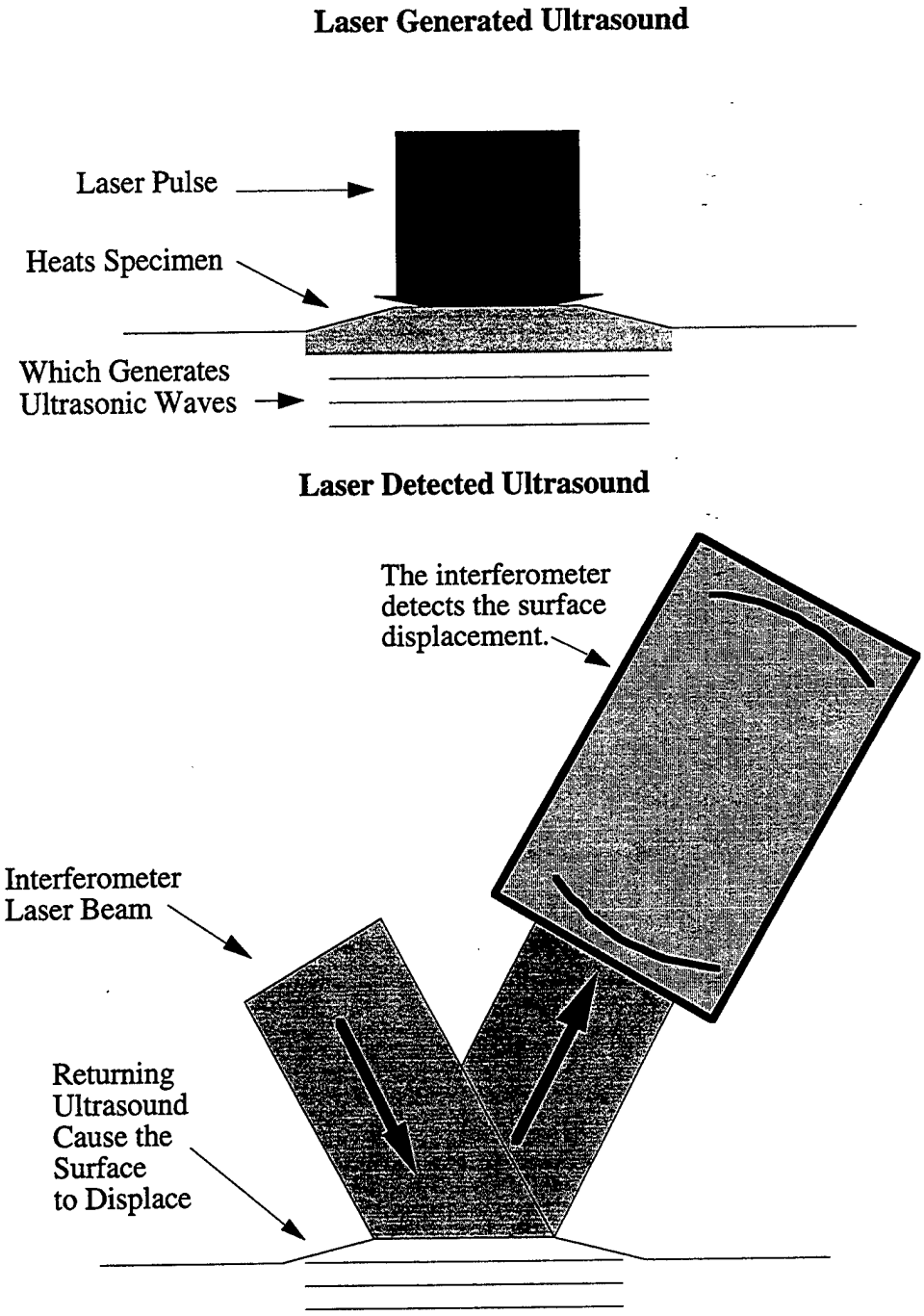

Figure 1. Generation, propagation, and detection of laser based ultrasound.

This wave then propagates through the specimen, and is reflected by the substrate. The wave then propagates back to the surface of the specimen, where it can be detected interferometrically by measuring the displacement of the surface of the specimen (Figure 1).

The thinnest inspectable layer using conventional LBU systems is limited by the pulse length of the Nd:YAG laser used to generate the ultrasound. A typical Nd:YAG laser has a pulse length of 20 ns which generates ultrasound at frequencies up to 20 MHz (Scruby, 1990). Using pulse-echo ultrasonics, and assuming that the layer being inspected must be at least as thick as the wavelength of the ultrasound, the thinnest inspectable layer of aluminum would be 0.32 mm. While conventional LBU is nondestructive, the ultrasound it generates has too long a wavelength to be useful for inspecting thin coatings.

1.5 Ultrafast Laser Generated Ultrasound

To generate high frequency ultrasound, a very short pulse of laser light is required. The frequency of ultrasound generated is then dependant upon the optical absorption coefficient of the material, not the pulse length. Ti:Sapphire lasers are capable of generating ultrafast pulses of laser light, with pulse lengths less than 100 femtoseconds (fs) long. These pulses, which are five orders of magnitude shorter than Nd:YAG pulses, generate ultrasound with frequencies which extend up to 200 GHz, four orders of magnitude higher. The ultrashort pulses of ultra-

sound propagate through the thin coating, are reflected by the substrate, and return to the surface of the coating.

Conventional piezoelectric transducers cannot be used to detect these high frequency ultrasonic echoes. These transducers require the sound to propagate through a coupling medium, and because the ultrasound is so high in frequency, it is attenuated before it reaches the transducer. The surface of the material itself will have to be used to detect the ultrashort pulses of ultrasound.

Conventional interferometers are capable of detecting high frequency ultrasound. Theoretically there is no frequency limit to the interferometer itself. The photodetector used to measure the light from the interferometer is, however, shot noise limited. The minimum detectable displacement of a shot noise limited interferometer is given by equation (1.1) (Wagner, 1990).

$$\delta = \sqrt{\frac{h\upsilon B}{\eta K^2 k^2 P_0} \frac{(1 + K\cos k(z_R - z_0))}{(\sin k(z_R - z_0))^2}} \tag{1.1}$$

δ is the minimum detectable displacement of the surface, $k = \frac{2\pi}{\lambda}$ is the wavenumber and λ is the wavelength of the light, h is Planck's constant, ν is the frequency of the light, B is the bandwidth of the detector, η is the quantum efficiency of the detector, and P_0 is the amount of light reaching the photodetector. K is the ratio of the signal beam intensity to the reference beam intensity for the interferometer, and for an ideal interferometer can approach 1. At the maximum signal to

noise ratio, $\sin k\,(z_R - z_0) = 1$, so equation (1.1) reduces to:

$$\delta = \sqrt{\frac{h\upsilon B}{\eta k^2 P_0}} \tag{1.2}$$

Assuming a 1 mW HeNe laser, and a bandwidth of 200 GHz, the minimum detectable displacement is 798 pm. For an aluminum coating, the displacement of the surface due to an ultrasonic wave is typically only 8 pm (see Section 4.6). Not only is the shot noise limited interferometer unable to detect displacements that small, but the problems of transmitting and measuring signals with 200 GHz bandwidths are formidable. Conventional interferometry is not practical for thin coatings.

Piezoreflective inspection methods are able to detect high frequency pulses of ultrasound (Thomsen, 1986). Piezoreflective detection uses the property that, for some materials, the reflectivity of the material is a function of the strain at the surface of the material. Ultrasonic waves, which are strain waves, can then be detected by measuring the change in reflectivity of the surface of the specimen.

To reduce the bandwidth of the signals which must be detected, part of the ultrafast pulse from the Ti:Sapphire laser is split off the heating beam, and used as a "probe" pulse (Figure 2). By varying the time at which the probe pulse hits the specimen after the heating pulse (by changing the length of the delay line), the strain at the surface of the specimen can be measured as a function of time. Figure 3 shows the reflectivity for an aluminum specimen as a function of time, and the

heating pulse (the rise in the piezoreflective signal at 30ps) and four ultrasonic echoes.

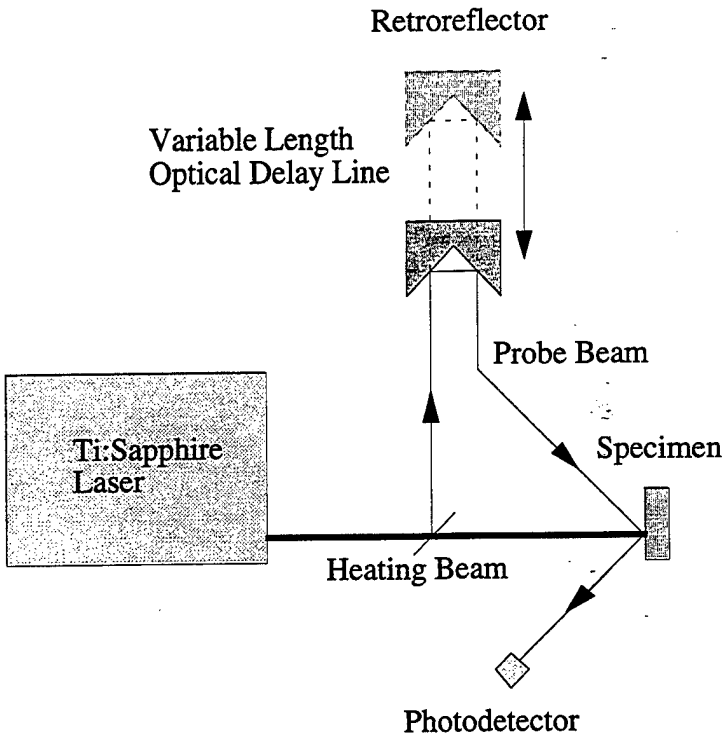

Figure 2. Piezoreflective detection of ultrafast pulses of ultrasound.

Piezoreflective detection requires the specimen to be piezoreflective. Gold, tin, and molybdenum are examples of materials which are so weakly piezoreflective that this technique fails to detect ultrasonic echoes. To inspect these materials piezoreflectively, it is necessary to place a thin "transducer" coating over the coating. Since this transducer layer cannot be removed, the technique is not nondestructive.

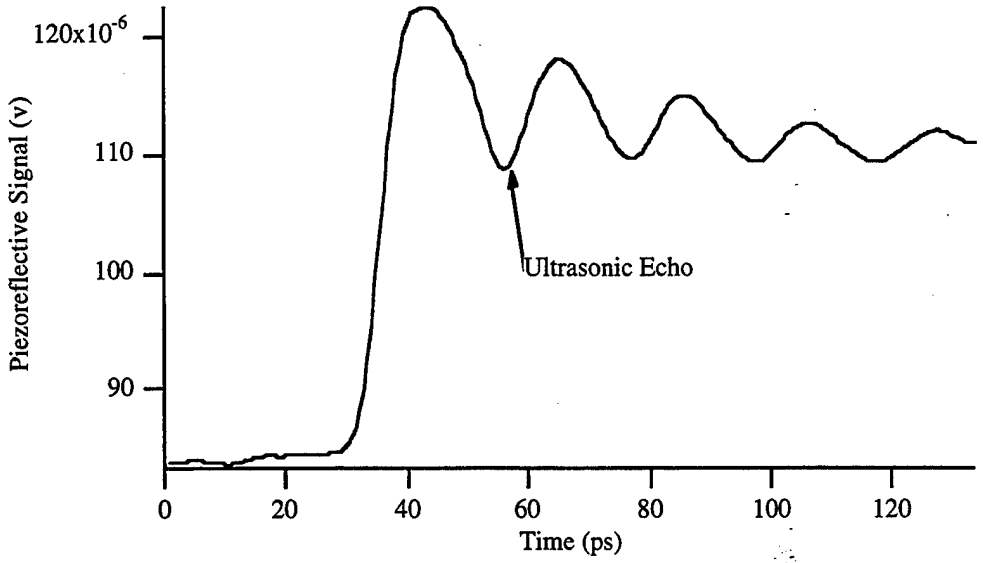

Figure 3. Piezoreflective signal for 200 nm of aluminum over 300 nm of gold-palladium on glass.

Interferometric detection of ultrafast laser generated ultrasound is, however, a nondestructive method for detecting ultrasonic echoes. The interferometer detects the displacement of the surface caused by the ultrasonic echoes whether the material is piezoreflective or not. To reduce the bandwidth of the signals which must be detected, the interferometer uses pulses of laser light split off from the heating beam, and an optical delay line (Figure 4).

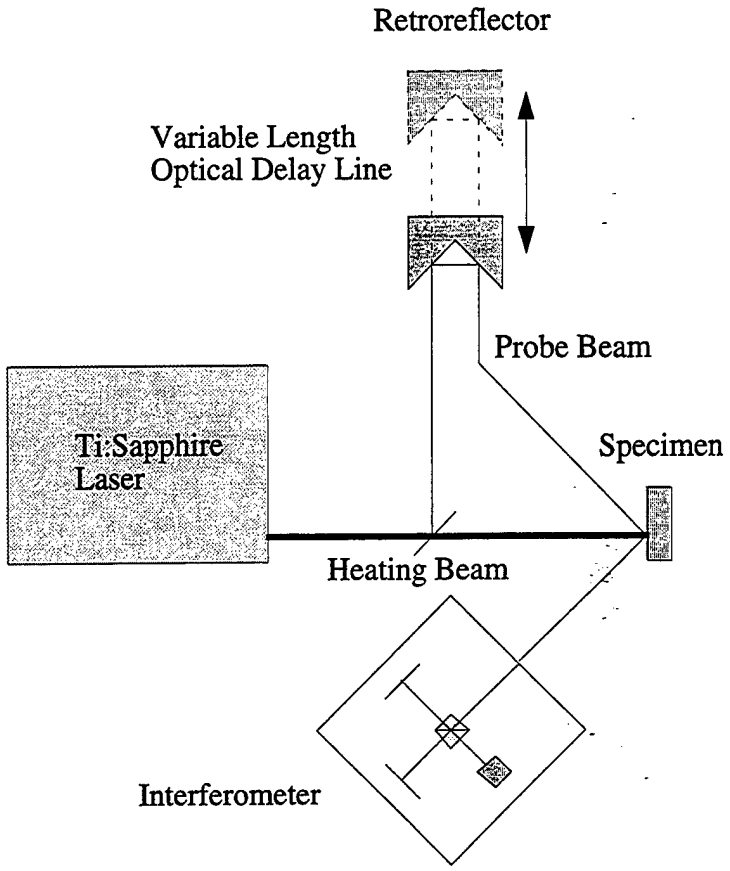

Figure 4. Interferometric detection of UFLGU.

1.6 Literature Review

Ultrafast laser generated ultrasound (UFLGU) was initially discovered as a perturbation on a pump and probe experiment (Thomsen, 1984). The photoinduced changes in the optical transmission of thin films of a-As_2Te_3 and cis-polyacetylene were being measured. The film was excited using an ultrafast pump light pulse, and the optical transmission of the film was measured with a delayed probe pulse which was delayed relative to the pump pulse. Oscillatory changes in

the optical transmission of the film were noticed, and it was speculated that these changes were due to ultrasound. Further experiments revealed that these oscillations varied linearly with film thickness as expected, and that the amplitudes of the oscillations were consistent with their model.

Similar changes in the reflectivity of thin films due to ultrasound were measured in semiconductor and metallic films (Thomsen, 1986). A theory which predicted the generation of ultrasonic strains and the piezoreflective detection of these strains was developed. This theory was validated on semiconductors (a-As_2Te_3) and metals (nickel). The ability of the ultrasonic technique to detect weak bonds of aluminum films on glass substrates was also demonstrated.

The generation and detection of phonons (ultrasound) in transparent coatings has been reported (Lin, 1990). The pump pulse passes through the transparent coating, and is absorbed by the substrate where it generates ultrasound. The ultrasound then propagates through the coating, and is detected as oscillations on the reflection signal. These oscillations were detected in fused quartz and borosilicate glass. The damping of the ultrasonic wave due to surface microcracks in sapphire was also demonstrated, an application of UFLGU which could be of importance to the manufacture of microelectronics.

In another application of ultrafast techniques to microelectronics problems, the detection of fluorocarbon contaminate layers as thin as 0.5 nm was demonstrated (Tas, 1992). Vibrations, at a frequency of 210 GHz, were excited in 15 nm

thick Al films. In films with a layer of fluorocarbon contaminates between the film and substrate the vibrations continued for 10 ps, while in films which had no contaminates and a good bond to the substrate the vibrations died out immediately. The detection of these thin interfacial layers by monitoring the thermoreflectance cooling curve was also demonstrated.

Other researchers have used the thermoreflectance curve to measure the thermal diffusivity of materials (Paddock, 1986). A finite difference model was used to describe the cooling of the thin coating, and a simplex fitting routine was used to deduce the thermal diffusivity. The diffusivity of thin films of nickel agreed with the literature value to within 6%.

Detection of ultrafast ultrasonic pulses using a bi-cell detector and surface deflection techniques was demonstrated by Wright. The vibrations of the surface of the specimen were measured by examining a change in the slope of the surface of the specimen (Wright, 1991).

2. THEORY

2.1 Generation of Ultrasound using Ultrafast Pulses of Laser Light

Ultrasound is generated by the sharp rise in temperature which occurs when a pulse of laser light is absorbed at the surface of a material. To describe the generation of ultrasound, it is necessary to be able to predict the temperature rise of the specimen due to the absorption of the laser pulse. Two theories which explicitly predict the temperature rise during the heating pulse will be presented, and will then be used to check the finite difference theory, which also predicts the cooling of the surface of the specimen after the heating pulse is finished.

2.1.1 Maris's Model

Maris assumed that the period of the ultrafast pulse would be so short that no heat conduction would occur (Thomsen, 1986). The temperature rise of the material is then given by the amount of energy deposited per unit volume, divided by the heat capacity of the material. This is expressed empirically as equation (2.1).

$$T(z) = (1-R)\frac{Q}{AC\zeta}e^{-z/\zeta} \tag{2.1}$$

T(z) is the temperature rise as a function of depth z into the material, R is the reflectivity of the specimen, Q is the energy in the heating pulse, A is the area of the laser beam, C is the specific heat per unit volume of the specimen, and ζ is the optical absorption length of the material. This is only a one dimensional descrip-

tion of the temperature profile, but since the width of the heating beam is significantly larger than then the thickness of the coating, the heat flow in the lateral direction is negligible.

2.1.2 Carslaw and Jaeger's Model

Carslaw and Jaeger's theory predicts the temperature rise due to a heat source which decays exponentially as a function of depth into the specimen (Carslaw, 1959). This theory was developed for the problem of a microwave heat source on an infinite half space, but it also applies to the problem of laser absorption by at the surface of a material (2.2).

$$T(z,t) = a + bz + \left(2b + \frac{2A_0}{K\alpha}\right)\sqrt{\kappa t}\,ierfc\left(\frac{z}{2\sqrt{\kappa t}}\right) - \frac{A_0}{\alpha^2 K}e^{-\alpha z} + \frac{A_0}{2\alpha^2 K}e^{\alpha^2\kappa t - \alpha x}erfc\left[\alpha\sqrt{\kappa t} - \frac{z}{2\sqrt{\kappa t}}\right] + \frac{A_0}{2\alpha^2 K}e^{\alpha^2\kappa t + \alpha x}erfc\left[\alpha\sqrt{\kappa t} + \frac{z}{2\sqrt{\kappa t}}\right] \quad (2.2)$$

$T(z,t)$ is the temperature rise, t is time, A_0 is the heat flux at the surface of the specimen and is given by the instantaneous power absorbed by the specimen divided by the area that is heated. The variables a and b represent the initial temperature distribution in the material, and are set to zero for the thin film. The thermal diffusivity κ is determined from the thermal conductivity of the specimen K, the specific heat of the specimen C, and the density of the specimen ρ.

$$\kappa = \frac{K}{\rho C} \tag{2.3}$$

The complementary error function *erfc* is related to the error function (*erf*) by (2.4).

$$erfc\,(x) = 1 - erf\,(x) \tag{2.4}$$

Carslaw and Jaeger's theory is an analytical solution to the heat conduction equation, and does account for heat conduction in the z direction during the heating cycle. While the model is based on the assumptions that lateral heat flows and heat flows into the air above the specimen are negligible, these assumptions are both valid for the short time scales while the ultrafast pulse is being absorbed. This model, at least in this form, does not describe the cooling of the specimen after the heating pulse is finished. It has been suggested that differentiating (2.2) would convert the model from the case of a step function heat source in time to an impulse function, and the model would then describe the cooling of the specimen (Spicer, 1996). This is left as an exercise for the reader.

2.1.3 Finite Difference Simulation

Rather than solving the heat conduction equation analytically, the finite difference method can be used to model it numerically. The temperature can then be predicted from the initial temperature distribution and the boundary conditions as a function of time.

The finite difference method starts with the classic heat conduction equation (2.5).

$$\nabla^2 T = \frac{1}{\kappa}\frac{\partial T}{\partial t} \tag{2.5}$$

Because the heating beam is much larger than the thickness of the coating, the heat flow in the lateral directions are negligible, which reduces (2.5) to a one dimensional equation (2.6).

$$\frac{\partial^2}{\partial z^2} T(z,t) = \frac{1}{\kappa}\frac{\partial T}{\partial t} \tag{2.6}$$

The classic definition of the first derivative of temperature with respect to z is given by (2.7).

$$\frac{\partial}{\partial z} T(z,t) = \lim_{\Delta z \to 0} \frac{T(z+\Delta z, t) - T(z,t)}{\Delta z} \tag{2.7}$$

Rather than letting Δz go to zero, the solid is divided into discrete points, and Δz is the distance between points. The forward difference derivative then becomes (2.8), and the backward difference derivative becomes (2.9) and the variables are shown in Figure 5.

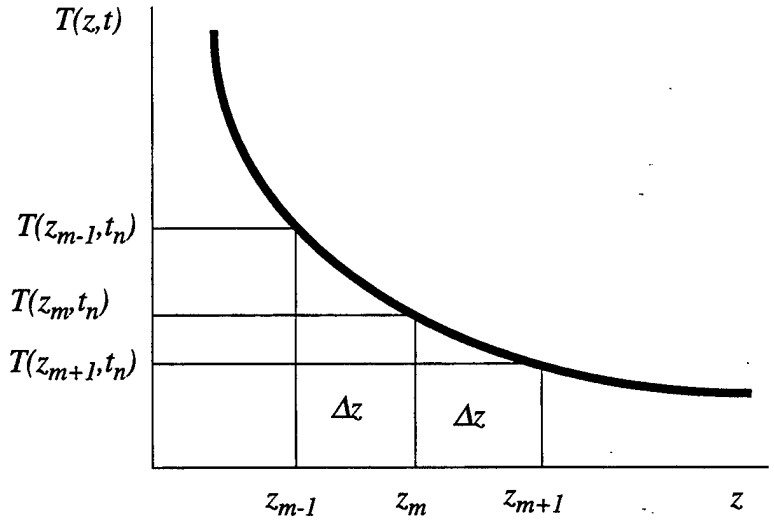

Figure 5. Finite difference variables.

$$\frac{\partial}{\partial z}T\left(z_{m+\frac{1}{2}}, t_n\right) = \frac{T(z_{m+1}, t_n) - T(z_m, t_n)}{\Delta z} \tag{2.8}$$

$$\frac{\partial}{\partial z}T\left(z_{m-\frac{1}{2}}, t_n\right) = \frac{T(z_m, t_n) - T(z_{m-1}, t_n)}{\Delta z} \tag{2.9}$$

Using forward and backward difference formulae, the second derivative can be expressed as (2.10).

$$\frac{\partial^2}{\partial z^2}T(z_m, t_n) = \frac{\frac{\partial}{\partial z}\left(\frac{\partial}{\partial z}T\left(z_{m+\frac{1}{2}}, t_n\right)\right) - \frac{\partial}{\partial z}\left(\frac{\partial}{\partial z}T\left(z_{m-\frac{1}{2}}, t_n\right)\right)}{\Delta z} \quad (2.10)$$

$$= \frac{T(z_{m+1}, t) - 2T(z_m, t) + T(z_{m-1}, t)}{\Delta z^2}$$

Similarly, the forward difference for t is:

$$\frac{\partial}{\partial t}T\left(z, t_{n+\frac{1}{2}}\right) = \frac{T(z, t_{n+1}) - T(z, t_n)}{\Delta t} \quad (2.11)$$

Equations (2.10) and (2.11) can then be used to solve the heat conduction equation for the temperature at the n+1 time step.

$$T(z_m, t_{n+1}) = T(z_m, t_n) + \kappa\frac{\Delta t}{\Delta z^2}(T(z_{m+1}, t_n) - 2T(z_m, t_n) + T(z_m, t_n)) \quad (2.12)$$

The heating of the specimen is modelled by adding temperature increases to the finite difference elements which absorb the laser light. The amount of heat absorbed by each element is calculated from the optical absorption coefficient of the material. The temperature rise is calculated by dividing the absorbed heat by the thermal capacity of the element. By adding the temperature rise at each time step, conduction of the heat during the heating of the specimen is modelled.

For the finite difference method to converge, the quantity $\kappa\frac{\Delta t}{\Delta z^2}$ must be less than 1.0, and should be less than 0.1.

This finite difference model describes both the heating and the cooling of the specimen, which allows the shape of the thermoreflectance cooling curves to be predicted.

2.2 Thermoelastic Stress Distribution Due to the Laser Pulse

The one dimensional linear thermoelastic theory is used to calculate the expansion, or strain in the specimen caused by the heating pulse (Thomsen, 1986).

$$\varepsilon(z) = -3\beta T(z) \tag{2.13}$$

ε is the strain in the z direction, β is the thermal expansion coefficient, and T is the temperature rise in the specimen due to the laser heating. The stress distribution is obtained by multiplying the strain distribution by B, the bulk modulus (2.14).

$$\sigma(z) = -3\beta BT(z) \tag{2.14}$$

2.3 Propagation of the Thermoelastic Stress Pulse

Once the initial stress distribution has been generated, half of the stress distribution propagates in the positive z direction, and the other half propagates in the negative z direction. This is described by (2.15) where v is the longitudinal speed of sound.

$$\eta(z,t) = \sigma(z-vt) + \sigma(z+vt) \tag{2.15}$$

This is shown schematically in Figure 6 where ultrasonic wave A propagates in the

positive z direction. Wave B, which propagates in the negative direction, is reflected by the free surface and changes from a compressive to a tensile wave (wave C). Wave B and wave C add together using superposition for $z > 0$ yielding wave D. The stress at the free surface due to wave B (shown by arrow 1) is the same in magnitude but opposite in sign to the stress due to wave C at $z = 0$ (shown by arrow 2).

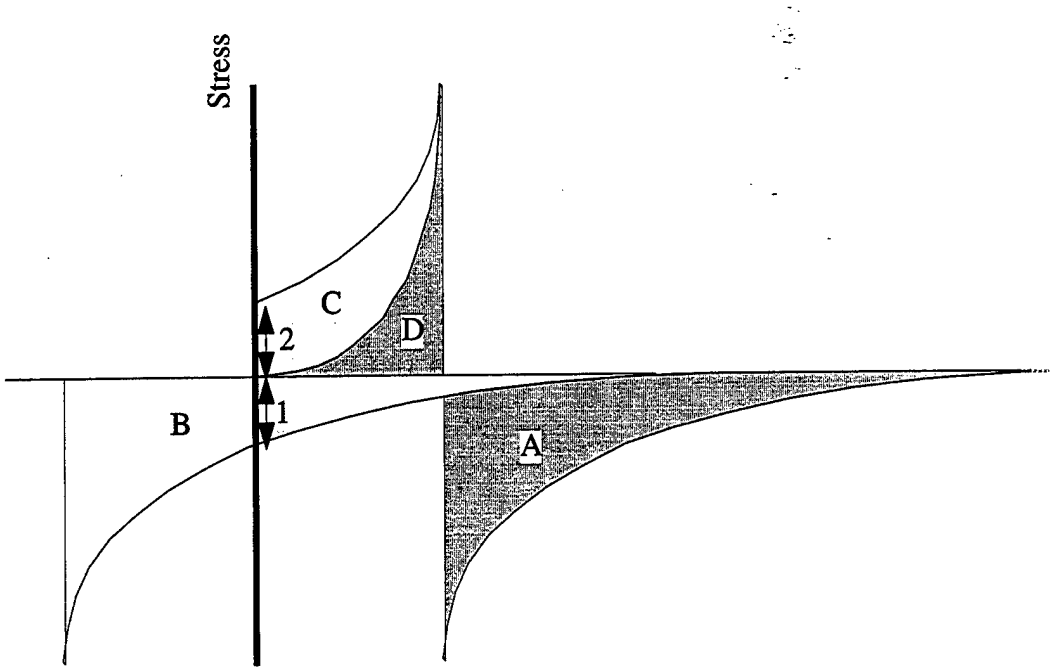

Figure 6. Propagation of the ultrasonic stress wave near the interface.

These two stresses will always sum to 0 at $z = 0$. The overall displacement of the surface (the sum of all the strains from $z = 0$ to $z = \infty$) will, however, be nonzero and the sum of the stresses B and C at $z > 0$ will of course be nonzero.

2.4 Thermal Waves

In addition to generating ultrasound, the heating beam also generates thermal waves because it is chopped. This chopping is necessary to use lock-in detection to observe the small changes in reflectivity on top of a large DC offset. Rosencwaig has demonstrated that thermal waves will modulate the reflectivity of the specimen at the chopping frequency (Rosencwaig, 1985), and can be used to determine the thermoreflectivity of a material. Knowing the thermoreflectivity of the material should make it possible to predict the thermal cooling curves from the ultrafast laser pulses. To do this, however, it is necessary to know the change in the surface temperature of the specimen caused by the thermal waves. Because of the difficulties inherent in measuring surface temperatures at high frequency, they were calculated instead.

One way to calculate the temperature increase of the specimen due to thermal waves is to assume that the specimen is a half space, and then calculate the temperature increase due to a heating beam which is turned on for half of the chopping cycle (2.16) (Carslaw, 1959).

$$T(z,t) = \frac{2F_0\sqrt{\kappa t}}{\kappa} ierfc\left(\frac{z}{2\sqrt{\kappa t}}\right) \tag{2.16}$$

Unfortunately the assumption that the coating can be treated as a half space is invalid. The distance for the temperature to drop to 50% of its value at the surface is 5 microns, which is much greater than the thickness of the coating. Because the thermal conductivity of glass substrates is 100 to 200 times less than that of the coating, it acts like an insulator.

This problem then becomes one of a layer heated with a constant flux on one side, and insulated on both sides. The solution to this problem is given by Carslaw and Jaeger (2.17) (Carslaw, 1959).

$$T(z,t) = \frac{F_0 t}{\rho c l} + \frac{F_0 l}{K}\left\{\frac{3x^2 - l^2}{6l^2} - \frac{2}{\pi^2}\sum_{n=1}^{\infty}\frac{(-1)^n}{n^2} e^{-\frac{\kappa n^2\pi^2 t}{l^2}} \cos\frac{n\pi z}{l}\right\} \tag{2.17}$$

The first term is merely the heat input divided by the thermal mass of the coating; the rest of the terms are corrections which vary across the thickness of the coating. At frequencies from 0.1 to 10 MHz the first term is at least an order of magnitude larger than the correction terms. This first term, where $t = \frac{1}{2f}$, also predicts a 1/f dependance on frequency, which has been observed experimentally.

The Rosencwaig-Gersho theory (2.18) also predicts a 1/f dependence for the surface temperature specimen in a photoacoustic cell (Rosencwaig, 1985).

$$T(0,t) = \frac{\beta I_0}{2\kappa(\beta^2-\sigma^2)} \left[\frac{(r-1)(b+1)e^{\sigma l} - (r+1)(b-1)e^{-\sigma l} + 2(b-r)e^{-\beta l}}{(g+1)(b+1)e^{\sigma l} - (g-1)(b-1)e^{-\sigma l}}\right] \quad (2.18)$$

where $\beta = \frac{1}{\zeta}$ is the optical absorption coefficient, ζ is the optical absorption length, $b = \frac{\kappa'' a''}{\kappa a}$, $g = \frac{\kappa' a'}{\kappa a}$, $a = \sqrt{\frac{\omega}{2\kappa}}$, $\omega = 2\pi f$, $\sigma = (1+i)a$, and $r = (1-i)\frac{\beta}{2a}$. The prime and double prime variables refer to the gas above the specimen, and the backing behind the specimen respectively. For the case when the thin coating is the specimen, air is the gas above the specimen, glass is the substrate material and neither air nor glass conduct heat as well as metals, so $b = g = 0$. This simplifies equation (2.18) to:

$$T(0,t) = \frac{\beta I_0}{2\kappa(\beta^2-\sigma^2)} \left[\frac{(r-1)e^{\sigma l} + (r+1)e^{-\sigma l} - 2re^{-\beta l}}{e^{\sigma l} - e^{-\sigma l}}\right] \quad (2.19)$$

At 1 MHz r>>1, so (2.19) reduces to:

$$T(0,t) = \frac{\beta I_0}{2\kappa(\beta^2-\sigma^2)} \left[\frac{re^{\sigma l} + re^{-\sigma l} - 2re^{-\beta l}}{e^{\sigma l} - e^{-\sigma l}}\right] \quad (2.20)$$

$e^{-\beta l} \cong 0$, and $\beta^2 \gg \sigma^2$, which leaves:

$$T(0,t) = \frac{I_0}{2\kappa\beta} \left[r\frac{e^{\sigma l} + e^{-\sigma l}}{e^{\sigma l} - e^{-\sigma l}}\right] \quad (2.21)$$

This equation reduces to:

$$T(0,t) = \frac{I_0}{2\kappa\beta}\left[r\frac{e^{2\sigma l}+1}{e^{2\sigma l}-1}\right] \tag{2.22}$$

Substituting for r and σ and simplifying gives:

$$T(0,t) = \frac{I_0}{4a\kappa}\left[(1-i)\frac{e^{2(1+i)al}+1}{e^{2(1+i)al}-1}\right] \tag{2.23}$$

Since $al \ll 1$, the following approximation is valid:

$$\frac{e^x+1}{e^x-1} = \frac{2}{x} \tag{2.24}$$

Which can be used to simplify (2.23):

$$T(0,t) = \frac{I_0}{4a^2\kappa l}\left[\frac{(1-i)}{-(1+i)}\right] \tag{2.25}$$

which reduces to:

$$T(0,t) = \frac{I_0\alpha i}{2\omega\kappa l} \tag{2.26}$$

Equation (2.26) is the solution for a layer which is optically thick and thermally thin. The 1/f (or $1/\omega$) dependence is obvious, and agrees with that found in the Carslaw and Jaeger theory.

2.5 Piezoreflective Strain Detection

The classic exposition of the reflectivity variation due to strain was performed by Thomsen and Maris (Thomsen, 1986). The change in the real (n) (2.27)

and imaginary (κ) (2.28) parts of the index of refraction are expressed in terms of η_{33}, the strain normal to the surface of the film.

$$\Delta n(z,t) = \frac{\partial n}{\partial \eta_{33}} \eta_{33}(z,t) \tag{2.27}$$

$$\Delta \kappa(z,t) = \frac{\partial \kappa}{\partial \eta_{33}} \eta_{33}(z,t) \tag{2.28}$$

The change in reflectivity due to strain is then calculated by solving Maxwell's equations inside the film when the optical properties vary as a function of position.

$$\frac{\partial^2 E_x}{\partial z^2} = -\frac{\omega^2}{c^2} [\varepsilon + \Delta\varepsilon(z,t)] E_x \tag{2.29}$$

where $\Delta\varepsilon(z,t)$ is the change in ε caused by the strain. The change in reflectivity is then given by:

$$\Delta R = \int_0^\infty f(z)\, \eta_{33}(z,t)\, dz \tag{2.30}$$

where:

$$f(z) = f_0 \left[\frac{\partial n}{\partial \eta_{33}} \sin\left(\frac{4\pi n z}{\lambda} - \phi \right) + \frac{\partial \kappa}{\partial \eta_{33}} \cos\left(\frac{4\pi n z}{\lambda} - \phi \right) \right] e^{-z/\zeta} \tag{2.31}$$

$$f_0 = 8 \frac{\omega \sqrt{n^2 (n^2 + \kappa^2 - 1)^2 + \kappa^2 (n^2 + \kappa^2 + 1)^2}}{c\,[(n+1)^2 + \kappa^2]^2} \tag{2.32}$$

$$\tan\phi = \frac{\kappa (n^2 + \kappa^2 + 1)}{n (n^2 + \kappa^2 - 1)} \tag{2.33}$$

Note that, for these equations, λ is the wavelength of light in free space, ζ is the optical absorption length, and ϕ lies between 0 and $\frac{\pi}{2}$. The sensitivity function f determines how strain at different depths below the surface of the film contributes to the change in reflectivity. For metals the quantities $\frac{\partial n}{\partial \eta_{33}}$ and $\frac{\partial \kappa}{\partial \eta_{33}}$ are not known, so it is typical to fit them to the experimental data.

Since there is not enough information about the change in refractive index as a function of temperature to use this theory in a model, (2.30) has been approximated with (2.34), where a is a complex constant.

$$\Delta R = a \int_0^d \eta_{33}(z, t)\, dz \tag{2.34}$$

2.6 Interferometric Detection

The interferometer used for this research is a pulsed variation of the classic Michelson interferometer. Instead of a continuous laser beam, ultrashort pulses of light are sent through the interferometer. The path length difference between the signal and reference arms of the interferometer is short enough so that each pulse interferes with itself. The theory then becomes the same as that for a conventional Michelson interferometer. The only difference is that the pulsed interferometer measures the interference at a specific point in time, which can be varied relative to the heating beam by changing the length of the delay line.

The Michelson interferometer is shown schematically in Figure 7. The coherent light from the laser is split by the beamsplitter into reference and signal beams. The reference beam reflects off mirror M1, and the signal beam reflects off the surface of the specimen. Both beams recombine and interfere at the beamsplitter, and the amplitude of the interference signal is measured with a photodetector.

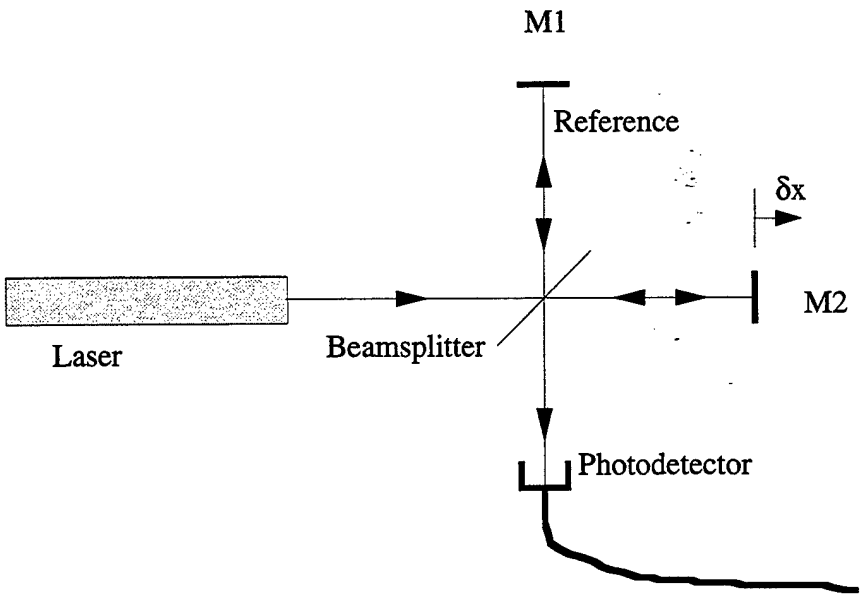

Figure 7. Classic Michelson interferometer.

Following the notation and derivation of Scruby, the laser beams can be described using cosines:

$$E_1 = E_{10}\cos(2\pi\nu t + \phi_1) \quad E_2 = E_{20}\cos(2\pi\nu t + \phi_2) \qquad (2.35)$$

where E_{10} and E_{20} are the amplitudes of the electric fields and ϕ_1 and ϕ_2 are their phases (Scruby, 1990). The resultant after the fields are summed at the photo-

detector is given by:

$$E_t = E_1 + E_2 = (E_{10}\cos\phi_1 + E_{20}\cos\phi_2)\cos(2\pi\nu t) - (E_{10}\sin\phi_1 + E_{20}\sin\phi_2)\sin(2\pi\nu t) \quad (2.36)$$

The square of the amplitude of the resultant is given by summing the squares of the sine and cosine terms giving:

$$E_{To}^2 = E_{10}^2 + E_{20}^2 + 2E_{10}E_{20}\cos(\phi_1 - \phi_2) \quad (2.37)$$

The light intensity (as measured by a photodetector) is proportional to the square of the electric field:

$$I_t = I_1 + I_2 + 2\sqrt{I_1 I_2}\cos(\phi_1 - \phi_2) \quad (2.38)$$

Equation (2.38) predicts that the photodetector signal should change sinusoidally as the signal mirror is displaced linearly. The change in phase as a function of displacement is given by (2.39), and a typical interference curve is shown in Figure 8.

$$\phi_2 = \frac{4\pi x}{\lambda} \quad (2.39)$$

The sensitivity of the interferometer (change in voltage at the photodetector for a given change in displacement) is the derivative of the interference curve and is also shown on Figure 8.

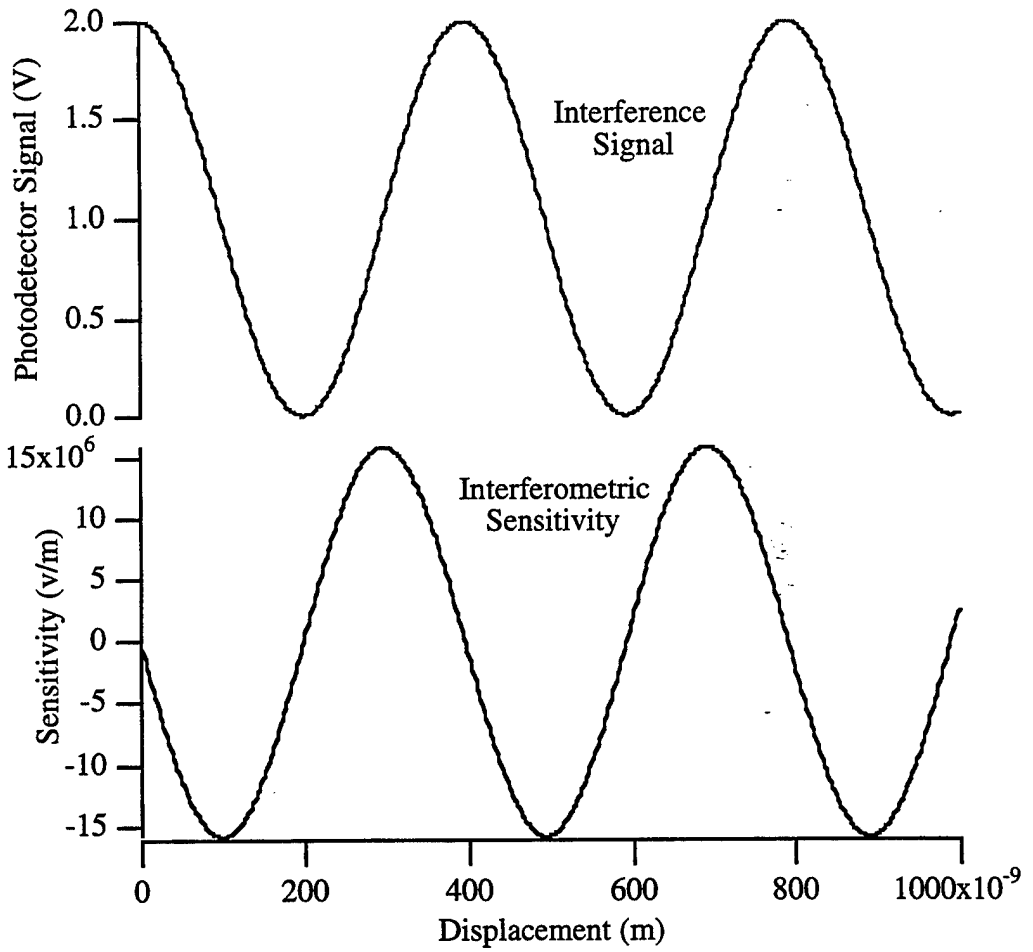

Figure 8. Interference signal and interferometric sensitivity for a Michelson interferometer as a function of displacement for light with a wavelength of 790 nm.

2.7 Combined Interferometric and Piezoreflective Detection

Both the piezoreflective and the interferometric signals will be at the same frequency, so both will be detected by the lock-in amplifier. The two signals will not have the same phase, however. According to J. Pease of Palo Alto Research Inc., (Pease, 1994), the lock-in amplifier will sum these two signals vectorially.

Consider the following piezoreflective (S_p) and interferometric (I_p) signals:

$$S_I(t) = A_I e^{i(\omega t + \phi_I)} \tag{2.40}$$

$$S_p(t) = A_p e^{i(\omega t + \phi_p)} \tag{2.41}$$

These signals are added vectorially by the lock-in amplifier, resulting in:

$$S_i + S_p = (A_i e^{i\phi_i} + A_p e^{i\phi_p})\, e^{i\omega t} \tag{2.42}$$

Because $e^{i\omega t}$ occurs in all the terms, it can be ignored. The real and imaginary parts of the signal measured by the lock-in S_l are:

$$S_l = (A_i \cos\phi_i + A_p \cos\phi_p) + (A_i \sin\phi_i + A_p \sin\phi_p)\, i \tag{2.43}$$

The magnitude and phase as measured by the lock-in are the standard magnitude and phase which are used in complex analysis. To obtain the interferometric signal, S_i, it is necessary to convert the lock-in signal and the piezoreflective signal into their real and imaginary parts, and then vectorially subtract the piezoreflective signal from the total signal, and then convert back to the magnitude and phase domain.

2.8 Thermoreflective Detection

The optical reflectance of materials is a function of temperature (Rosencwaig, 1985 and Cardona, 1969). The reflectivity is then given by:

$$R = R_0 + \frac{dR}{dT}\Delta T = R_0 + \Delta R \tag{2.44}$$

where R_0 is the sample reflectivity at temperature T_0 and $\frac{1}{R_0}\frac{dR}{dT}$ is the temperature coefficient of reflectivity, and ΔT the variation of the temperature of the sample surface from T_0. Typical values of $\frac{1}{R_0}\frac{dR}{dT}$ are on the order of 10^{-4}-10^{-5} °C. Rosencwaig notes that the thermoreflectivity signal is the same order of magnitude as the thermal wave deflection signal.

3. EXPERIMENTAL CONFIGURATION

3.1 Heating Beam

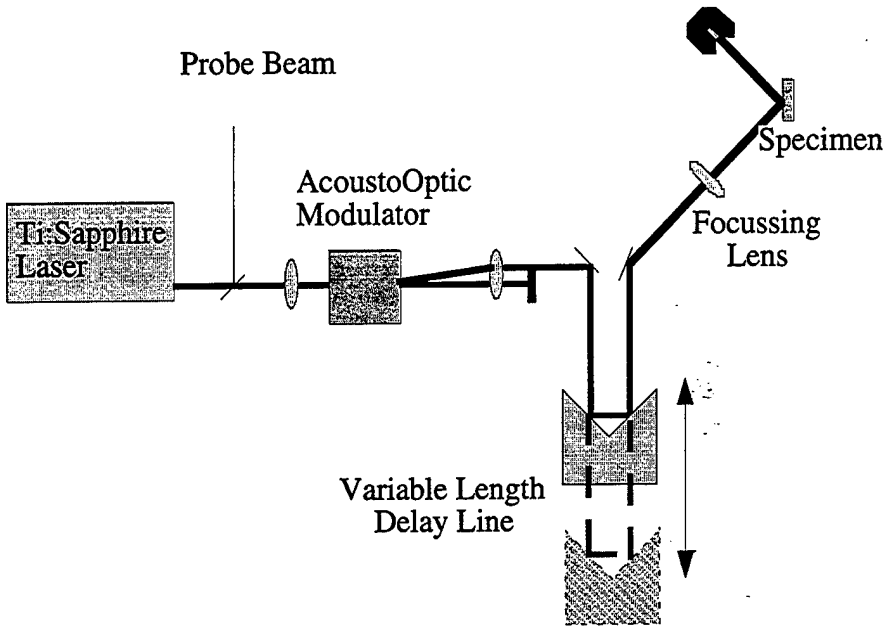

Figure 9. Heating beam schematic.

3.1.1 Ti:Sapphire Laser

The Ti:Sapphire laser is pumped with a Spectra Physics BeamLok 2080-12W Argon Ion laser. The Argon Ion laser is capable of producing 20 watts of power, but was operated at 8 watts because that power level produced the optimal Ti:Sapphire laser beam quality.

The Ti:Sapphire laser is a Spectra Physics Tsunami Model 3960-L1S, operated with the standard optics set in the femtosecond mode. The laser has a repetition rate of 82 MHz, and has less than 2% noise on the laser beam from 10 Hz to 2

MHz. The laser beam is less than 2 mm in diameter ($1/e^2$ points), and leaves the laser vertically polarized.

The wavelength of light produced by the laser can be varied between 710 nm to 850 nm, and the pulse length can be varied by changing the amount of dispersive glass in the laser cavity. Figure 10 shows how the output power of the laser (as measured using a silicon photodetector based power meter with wavelength calibration) and pulse length (measured using a Femtochrome FR-103 autocorrelator) varies as a function of wavelength (measured with an Oriel 77440 125 mm monochromator).

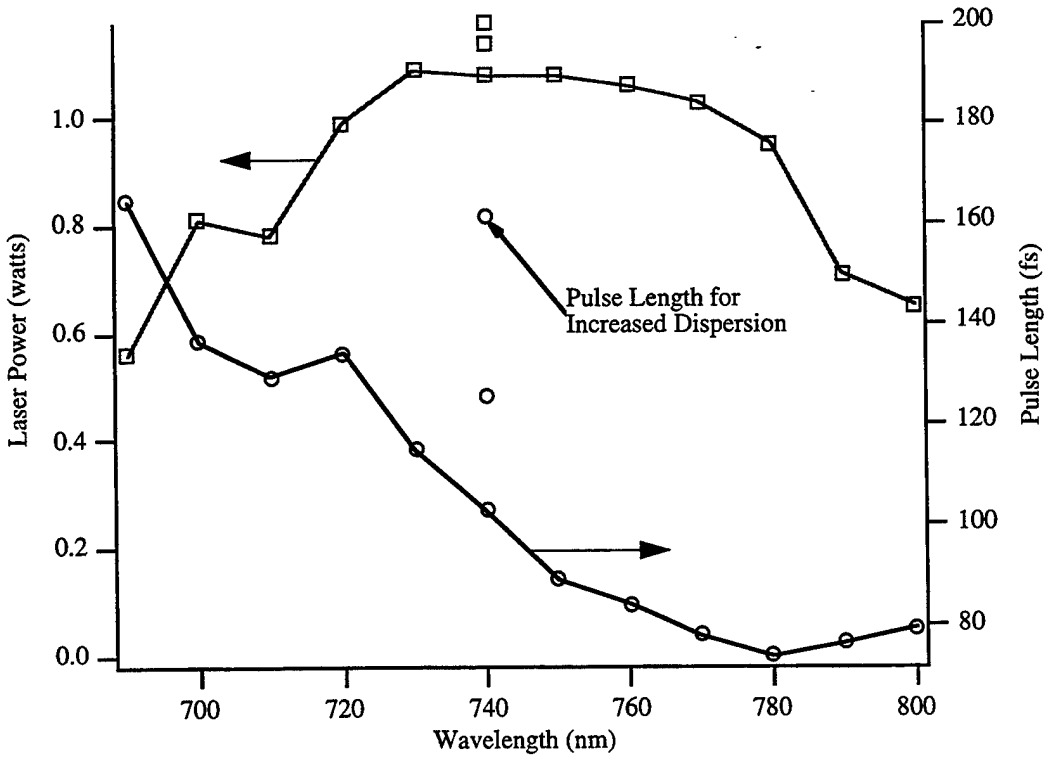

Figure 10. Ti:sapphire laser power and pulse length vs. wavelength.

The experimental results reported in Chapter 5 were acquired with the Ti:sapphire laser generating 1.5 watts of average power at 760 nm and a pulse length between 100 and 120 fs.

3.1.2 Acousto-Optic Modulator

The acousto-optic modulator (AOM) was used to chop the heating beam at frequencies ranging from 10 Hz to 10 MHz. The AOM is a NEOS 35085-3 AOM driven with a NEOS N310815 driver.

To chop at frequencies above 1 MHz it was necessary to focus the laser beam as it passes through the AOM. Focussing the beam, however, reduces the efficiency of the AOM because the light is no longer collimated as it passes through the AOM. A 400 mm focal length lens was used to allow the chopping frequency to go up to 10 MHz while maximizing the efficiency of the AOM. The efficiency of the AOM drops to 50%, which gives an average optical power at the specimen of 250 mW.

3.1.3 Delay Line

The delay line consists of a CVI 63.5 mm diameter retroreflector with gold mirrors mounted on an Aerotech ATS6000 translation stage. The laser beam reflects off three mirrors in the retroreflector which each have a 90% reflectivity.

3.1.4 Heating Beam Focussing

The heating beam is focussed onto the specimen using a 125 mm focal length lens. The diameter of the heating beam on the specimen is calculated from

equation (3.1).

$$w_0 = \frac{4\lambda f}{\pi D} \tag{3.1}$$

The beam waist at the specimen is 60.0 μm, and the area of the beam on the specimen is 2.83×10^{-9} m^2.

The energy per pulse, and the average instantaneous power of the laser to the specimen can be calculated from fact that the average power at the specimen is 0.2 W, and the repetition rate of the laser is 82 MHz. The unchopped laser beam must have twice as much average power as the chopped laser beam, 0.4 W, so that each laser pulse must have an energy of 4.87 nJ. The instantaneous power for a 100 fs pulse is 48.7 kW, and the instantaneous power density is 1.69×10^{13} W/m^2. A typical Nd:YAG laser, with a pulse width of 4 ns, a pulse energy of 20 mJ and focussed to a 1mm spot size has an instantaneous power of 5 MW, and an instantaneous power density of 6.36×10^{12} W/m^2. The instantaneous power density, the quantity which determines the amplitude of the generated ultrasound, is larger for the Ti:sapphire laser than the Nd:YAG laser, which suggests that the Ti:sapphire laser should be better at generating ultrasound.

3.1.5 Heating Beam Properties

The laser beam properties are summarized in Table 1, and will be used in the models in Chapter 4.

Table 1. Laser Beam Properties

Property		units
Average power Generated by the Laser	1.5	w
Average power to Specimen	0.2	w
Power to Specimen before Chopping	0.4	w
Energy per Laser Pulse to Specimen	4.9	nJ
Instantaneous Laser Power during Pulse	49	kw
Heating beam focussing lens focal length	125	mm
Focussed Heating Beam Diameter	60.0	μm
Focussed Heating Beam Area	2.8×10^{-9}	m^2
Instantaneous Laser Power Density	1.7×10^{13}	w

3.2 Probe Beam

The probe beam, which is split off the heating beam, is shown schematically in Figure 11.

3.2.1 Optics

The 100 fs pulses of light are so short in time, that they are composed of a range of wavelengths (due to the Hiesenberg uncertainty principle). Because the pulses are not monochromatic, they are subject to broadening due to dispersion. Reflecting these pulses off conventional multilayer broad band dielectric mirrors can lengthen the pulses from 100 fs to 200 fs. To prevent pulse broadening, single

layer Ti:Sapphire mirrors from CVI optics (PTS-767-2037-45-S) were used to preserve the beam quality.

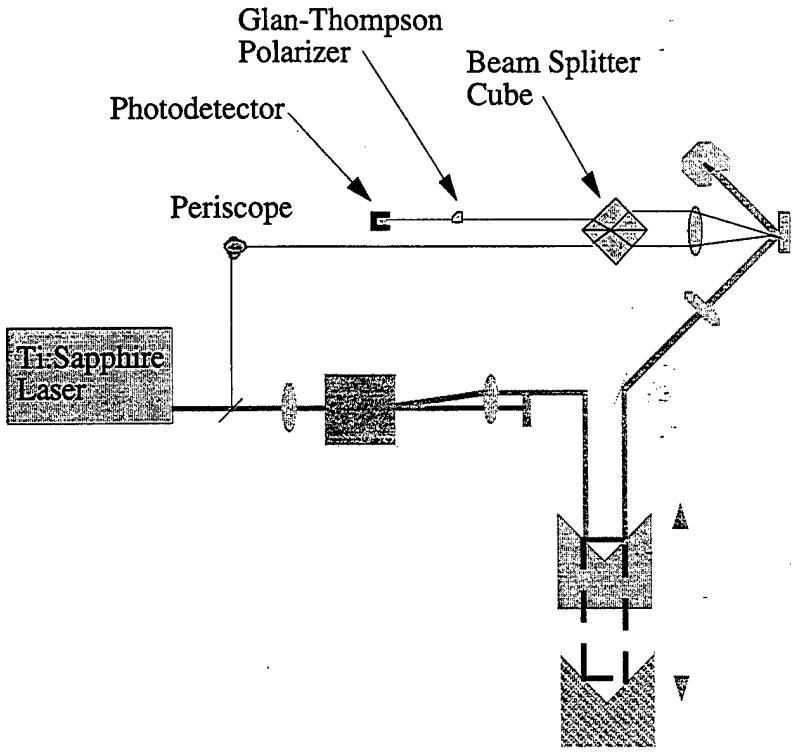

Figure 11. Probe beam path.

3.2.2 Polarization Sensitive Detection

One of the standard checks to ensure that the experiment is operating properly is to block the probe beam and verify that the lock-in signal goes to zero. On a number of specimens with rough surfaces it was found that there was still a significant signal, even though the probe beam was blocked. After much experimentation, it was determined that, because the changes in reflectivity that the

experiment detected were so small, even a minute amount of the heating beam scattered into the probe beam path by the specimen would generate a significant signal at the photodetector.

Polarization sensitive detection was used to ameliorate this problem. The laser beam exits the laser vertically polarized. A periscope (see Figure 11) is used to rotate the polarization of the probe beam. The light reflected off the specimen is then directed through a Glan-Thompson polarizer. The polarizer lets the horizontally polarized probe beam light pass on to the photodetector, while blocking scattered heating beam light with an extinction ratio of 10,000 to 1.

3.2.3 The Interferometer

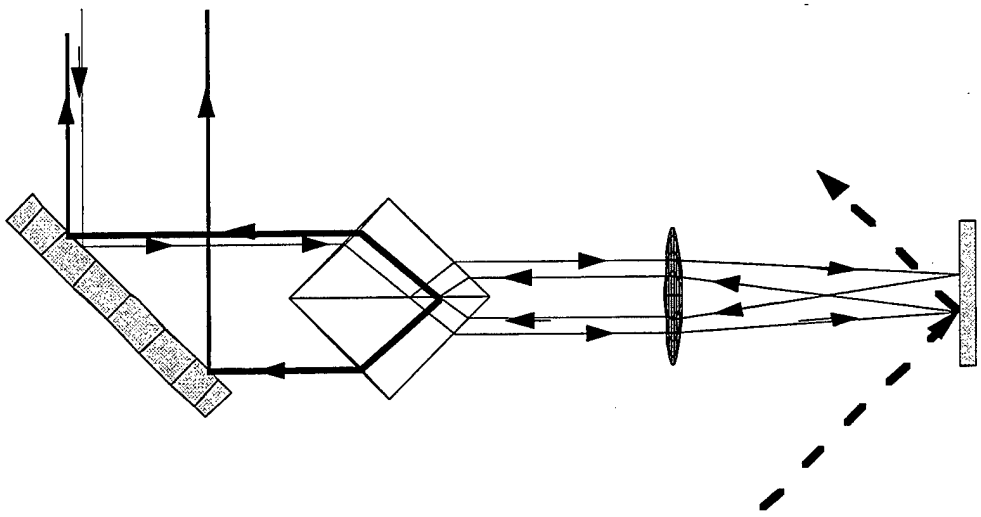

Figure 12. Schematic showing the ultrafast pulsed interferometer

The interferometer, shown schematically in Figure 12 and in a digital

image in Figure 13, is based on a 50/50 non-polarizing beam splitter cube. Light enters the beam splitter cube (the thin line) and is split at the interface into two beams. Each beam travels through the focusing lens, to the specimen, and then reflects back to the beam splitter cube. Light from each path then interferes with light from the other path (the heavy lines in Figure 12).

Since the laser beam is incident normal to the face of the beam splitter cube, it is acting as a 60/40 beam splitter instead of a 50/50 beam splitter. When the beams recombine at the interface, the same effect happens, so that one of the two sets of interfering beams from the beam splitter cube always has complete extinction of the fringes, and the other never has complete extinction.

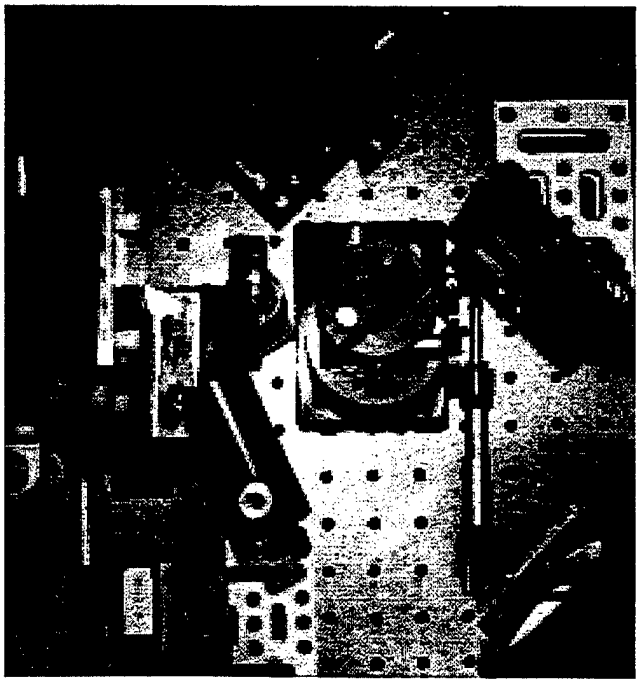

Figure 13. Digital image of the interferometer.

To set up the interferometer, it is necessary to start with the incident laser beam parallel to the dielectric interface. When the two beams emerge from the beam splitter cube, the lens focuses them onto the same spot on the specimen.

It is necessary to separate where these beams hit the specimen, so that the heating beam can be focussed onto only one of the spots. There are a number of ways to separate the beams. The tilt angle of the lens can be adjusted, the beam splitter cube can be rotated or the angle of the beam incident upon the beam splitter cube can be varied. The problem is, if the wrong adjustment is made, the laser beams will only interfere at a single point along the beam path. A spreadsheet based ray tracing analysis demonstrated that, if only the angle of the incoming laser beam to the beam splitter cube is adjusted, the laser beams will continue to interfere along their entire length.

3.2.4 Tilt Scans

The relative phase difference between the arms of a conventional interferometer can be varied by changing position of the reference mirror. With the setup shown in Figure 12, this is accomplished by tilting the specimen. By varying this tilt, it should be possible to generate the classic interference signals shown in Section 2.6.

3.3 Instrumentation

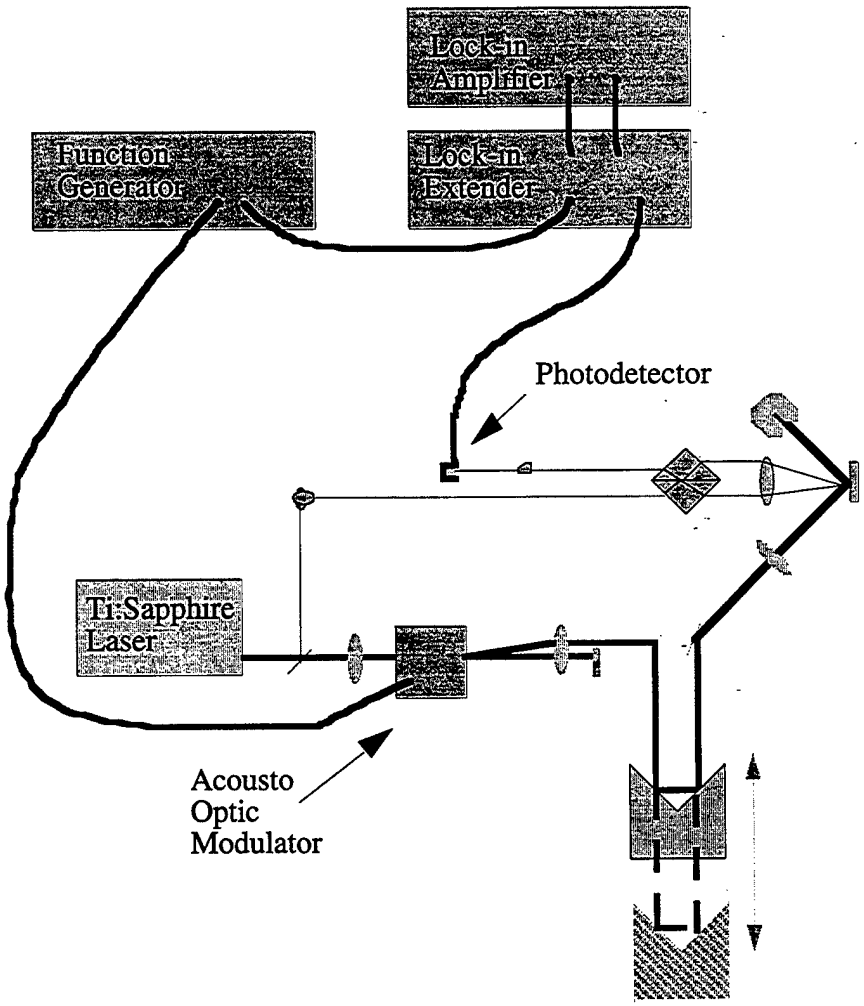

Figure 14. Instrumentation schematic.

3.3.1 Photodetector

The probe beam light is detected using a New Focus 1801 DC to 125 MHz amplified photodetector. The photodetector has a $2.4\times10^{4}\frac{V}{W}$ conversion gain, and a noise equivalent power of $3.3\frac{pW}{\sqrt{Hz}}$.

3.3.2 Lock-in Extender

The lock-in extender transforms high frequency signals (up to 10 MHz) down to 1 kHz so that the magnitude and phase of the signal can be measured with a conventional lock-in amplifier. A Palo Alto Research Corporation PAR100 lock-in extender was used for the experiments in this thesis, and was typically used with a gain of 40 db.

3.3.3 Lock-in Amplifier

A Stanford Research Systems SRS530 lock-in amplifier was used to measure the magnitude and phase of the signals coming from the lock-in extender. The lock-in amplifier takes the experimental signal, $V_s \cos(\omega_s t + \varnothing)$, and mixes it with the cosine and sine of a reference signal in Phase Sensitive Detectors (PSDs).

$$\begin{aligned} V_{psd1} &= V_s \cos(\omega_r t)\cos(\omega_s t + \varnothing) \\ &= \frac{V_s}{2}\cos[(\omega_r + \omega_s)t + \varnothing] \\ &\quad + \frac{V_s}{2}\cos[(\omega_r - \omega_s)t + \varnothing] \end{aligned} \tag{3.2}$$

$$V_{psd2} = V_s \sin(\omega_r t) \cos(\omega_s t + \varnothing) \tag{3.3}$$
$$= \frac{V_s}{2} \sin[(\omega_r + \omega_s) t + \varnothing]$$
$$+ \frac{V_s}{2} \sin[(\omega_r - \omega_s) t + \varnothing]$$

The sum frequency component of V_{psd} is attenuated with a low pass filter, and only the difference frequency components will be passed on to the DC amplifiers. For signals which are in phase with the reference signal, the output of PSD1 will be a maximum, and the output of PSD2 will vanish. The magnitude and phase of the signal are given by:

$$R = \sqrt{V_{psd1}^2 + V_{psd2}^2} \tag{3.4}$$
$$= \sqrt{\left[\frac{V_s}{2} \cos[(\omega_r - \omega_s) t + \varnothing]\right]^2 + \left[\frac{V_s}{2} \sin[(\omega_r - \omega_s) t + \varnothing]\right]^2}$$
$$= V_s$$

$$\varnothing = arctan\left(\frac{V_{psd2}}{V_{psd1}}\right) \tag{3.5}$$

3.4 Data Acquisition

The entire experiment is automated, allowing all important parameters of the experiment (chopping frequency, translation stage movement, and interferometric/piezoreflective beam block) to be controlled automatically, and the data from the lock-in amplifier and voltmeter to be collected via the computer. The

instrumentation in the experiment is interfaced to a Macintosh computer using an IEEE 488 instrumentation bus.

The programs to control the experiment and acquire data were written using Labview, an icon based data acquisition programming language developed by National Instruments Inc. This programming language was so easy to use that it reduced the time to develop new experiments from a few days to a few hours.

All the plots and many of the models for this research were produced using Igor, a plotting package written by Wavemetrics. In addition to a wide range of plotting features, Igor has a programming language which automates repetitive plotting tasks. The programming language was also used to model the data, so that the model could be compared directly to the experimental data. Igor reduced the time to plot the experimental data from the multiple tilt scans from over an hour to a few minutes.

3.5 Interferometer Alignment Procedure

Because the configuration of the interferometer is critical for reproducing the experimental results, a step by step procedure to align it is given.

1. Align the probe beam so that it is perpendicular to the front face of the specimen with the beam splitter cube and the focussing lens removed. This is accomplished by adjusting the beam steering mirror (BSM) until the laser beam reflected from the specimen lines up with the incoming beam. A notecard with a

hole for the incoming beam, placed 300 mm from the BSM is ideal for alignment purposes.

2. Insert the beam splitter cube (BSC) back into the probe beam such that two beams emerging from the BSC are as close as possible without changing the shape of the beams.

3. Adjust the rotation angle of the BSC so that the interfering beams at A reflect back along the path of the incoming laser beam. Once this is accomplished do not change this rotation angle, and the interfering beams will remain collinear and interfering along their entire path.

4. The beams at B in Figure 15 will now be interfering such that there is complete extinction at the nulls of the interference pattern. Adjust the tilt (in both planes) of the beam splitter cube to minimize the number of fringes. The minimum number of fringes which has been achieved was 3 horizontal fringes.

5. Place the focussing lens (FL) in the beam path such that interfering beams at A are colinear with the incoming beam.

6. Adjust the tilt on the BSM to separate the spots of light on the specimen. This separation is nominally 5 mm. It is typically necessary to adjust the position of the BSM after tilting it to ensure that the beams which emerge from the BSC are undistorted. This also causes the set of interfering beams at A, which now exhibit complete extinction to emerge from the BSC at a different angle than the incoming beams.

7. Place a beam pick-off mirror such that the fringes at A are reflected into the photodetector. Optimize the pointing of this mirror by maximizing the DC voltage from the photodetector when a beam block is placed in the reference arm of the interferometer.

8. Adjust the tilt on the BSC, and the position and tilt of the FL to minimize the number of interference fringes at the photodetector.

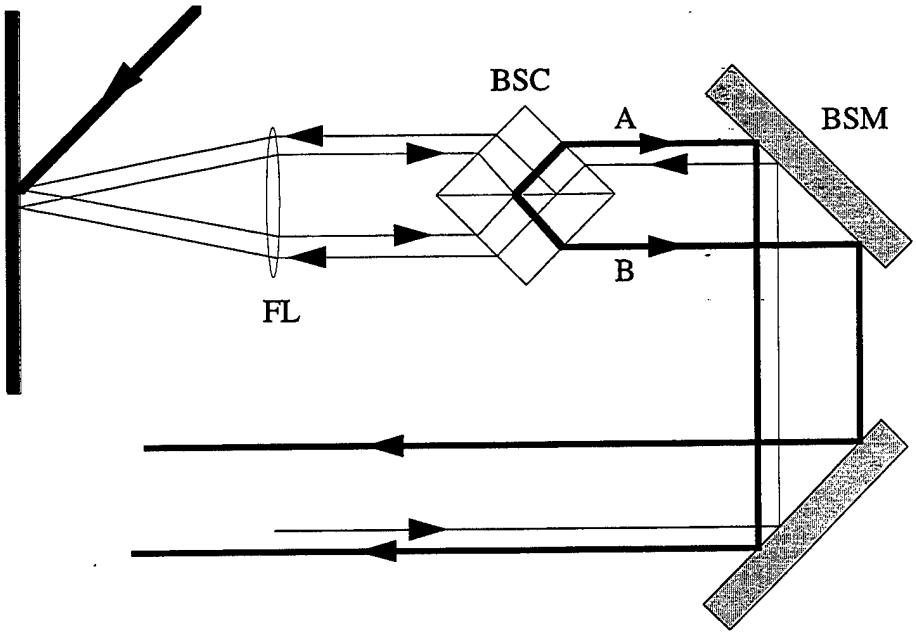

Figure 15. Interferometer alignment schematic.

9. Insert a cylindrical lens to expand the fringe pattern on the photodetector, so that the fringes are much larger than the photodetector.

10. Focus the heating beam on the same spot where the signal arm of the interferometer is focussed. Do this by adjusting the horizontal and vertical posi-

tioning of the heating beam focussing lens.

11. Optimize the focussing of the heating beam by blocking the reference arm of the interferometer and reducing the chopping frequency of the heating beam to 1 kHz. The experiment is now sensitive to the thermal-reflectance signal from the specimen. The width of the specimen which is affected by the thermal-reflectance signal is inversely proportional to the chopping frequency (Rosencwaig, 1980). By setting the chopping frequency at 1 kHz, the heated zone of the specimen is easy to locate. The chopping frequency is then increased first to 10 kHz, and then to100 kHz and the position of the heating beam is optimized at each frequency.

12. Increase the chopping frequency to 2 MHz, and verify that the heating beam is not leaking into the photodetector past the Glan-Thompson polarizer. To do this, block the incoming probe beam to the interferometer, and verify that the lock-in signal goes to zero.

13. If the experimental configuration has changed significantly, it may necessary to run a piezoreflective scan to determine where time zero is. This occurs when the heating and probe beams both hit the specimen at the same time. A typical plot, calibrated in terms of delay line displacement, is shown in Figure 16.

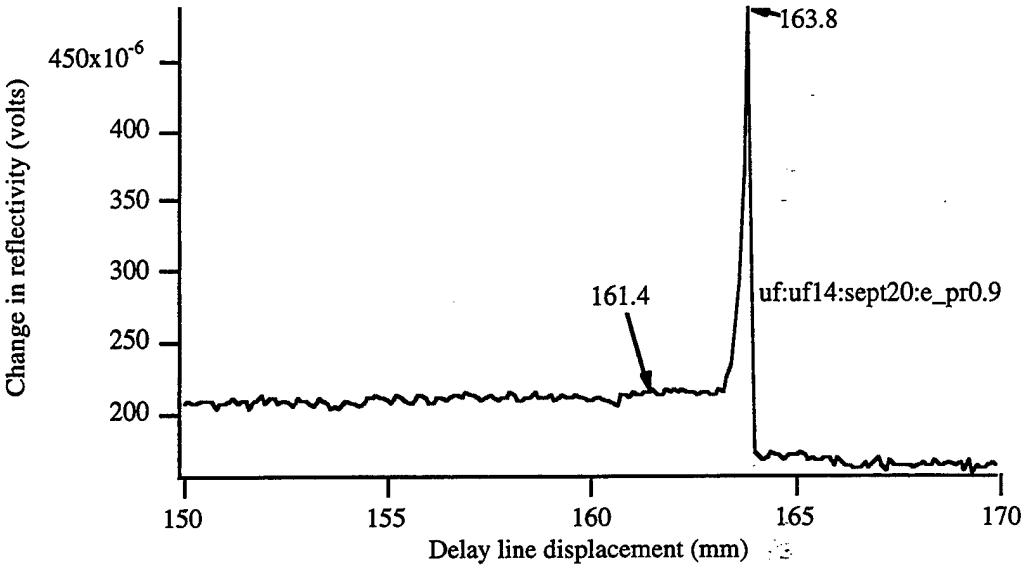

Figure 16. Piezoreflective scan showing time zero at 163.8 mm.

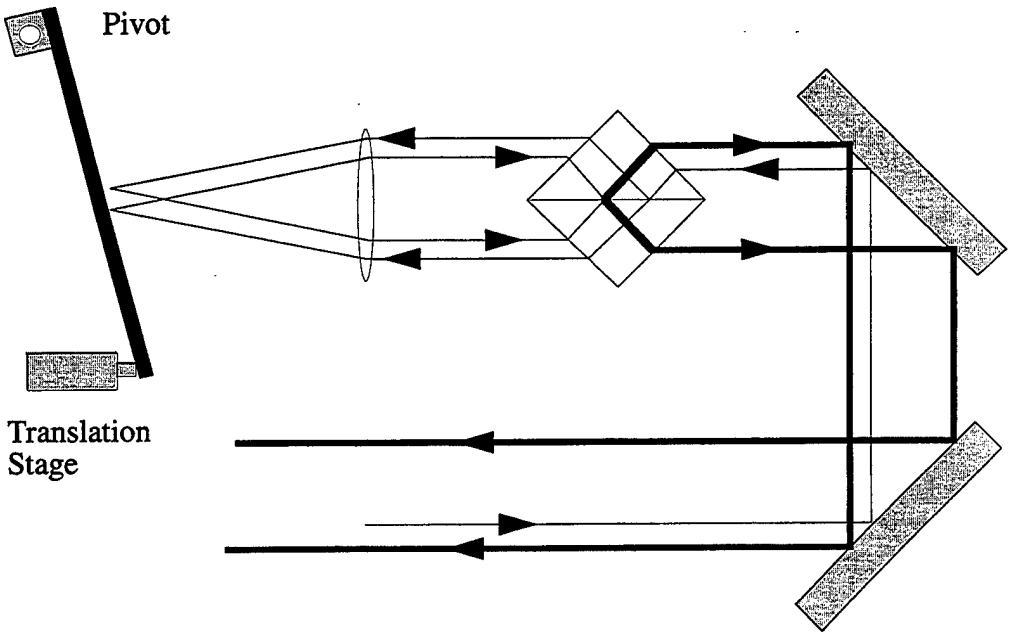

Figure 17. Interferometer path length variation caused by tilting the specimen.

14. The photodetector signal as a function of interferometer path length difference is measured by tilting the specimen. This is shown schematically in Figure 17. As the specimen is tilted, the length of one arm of the interferometer changes more than the length of the other arm. This causes the photodetector signal to vary between its minimum and maximum value, as shown in Figure 18. The voltage is measured with a digital voltmeter, not the lock-in.

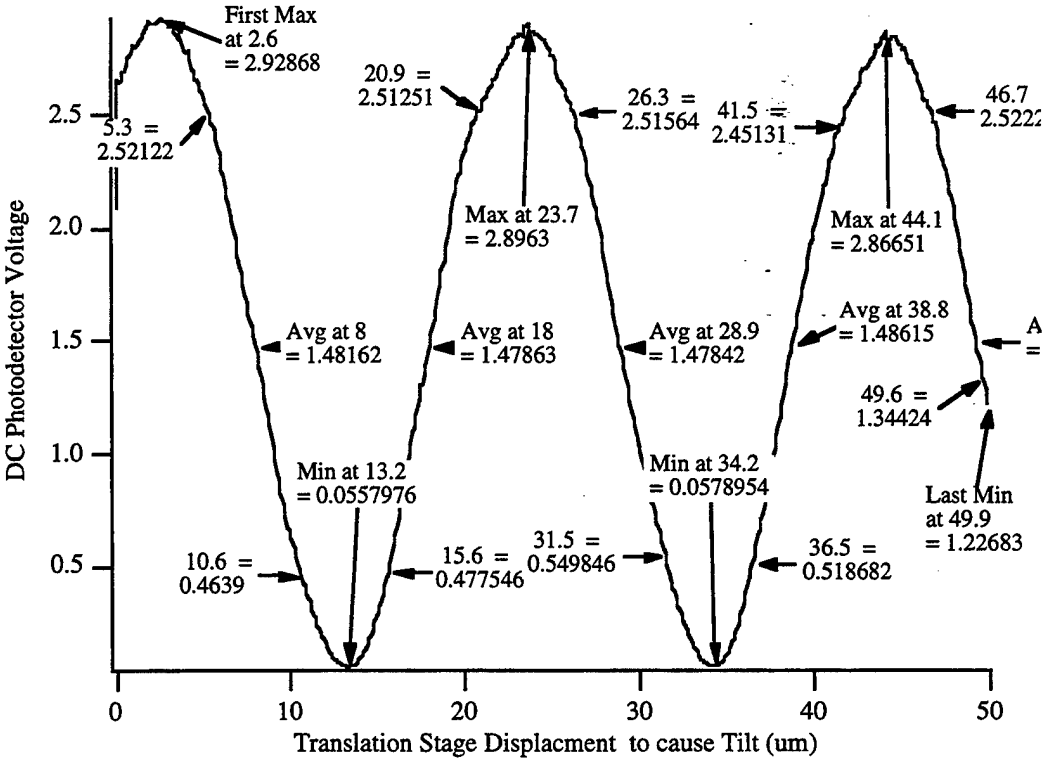

Figure 18. DC interferometer signal as a function of translation stage displacement to cause specimen tilt.

It is important to measure the minimum and maximum signal because it will allow the calculation of absolute displacements from the lock-in measurements.

15. It is now necessary to measure the interferometric signal as a function of tilt for the specimen before the heating pulse hits, after the heating pulse hits, and when an echo hits. Typical plots are shown in Figure 19.

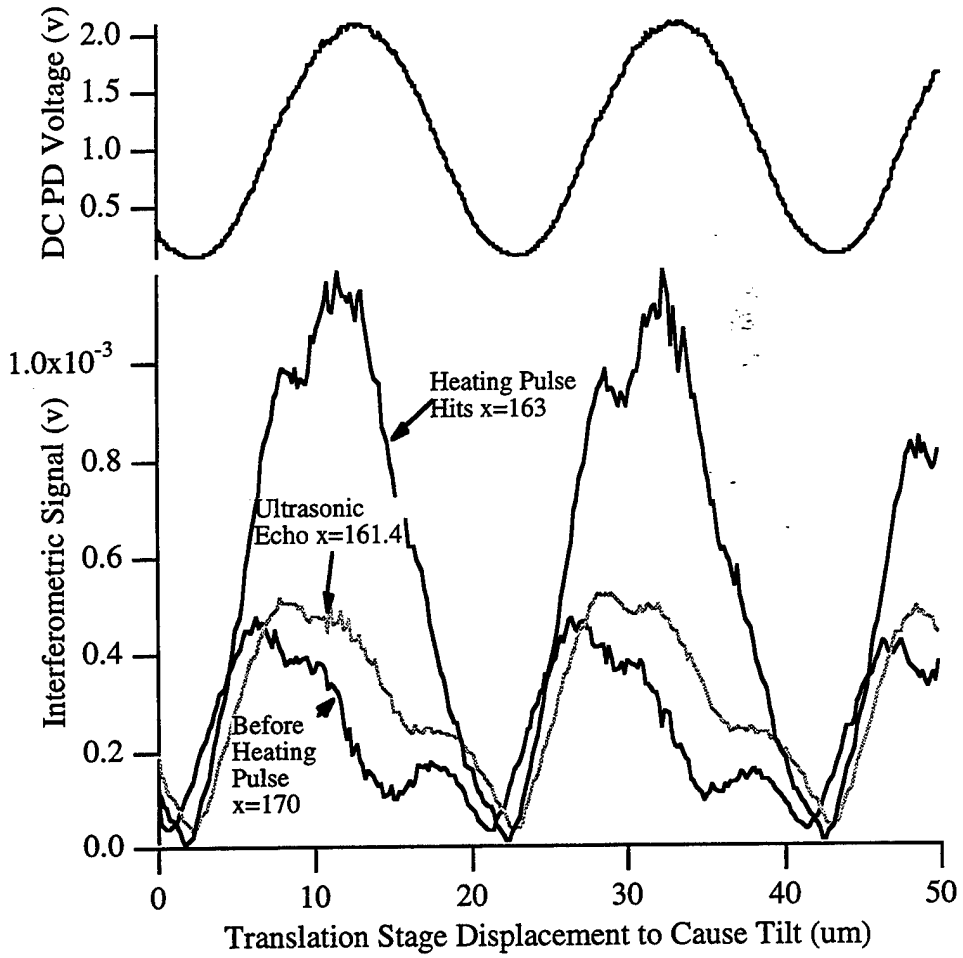

Figure 19. Interferometer signal as a function of tilt.

The interferometer signal vanishes when the DC interferometer signal is a minimum. The interferometer signal should also vanish when the DC interferometer signal is a maximum, because the slope of the DC curve is zero. This does not

happen, however, because there is also a piezoreflective signal.

16. It is necessary to characterize the piezoreflective signal as a function of tilt. The reference beam of the interferometer is blocked, and the tilt of the specimen is scanned. A typical plot is shown in Figure 20 along with the corresponding interferometric signal.

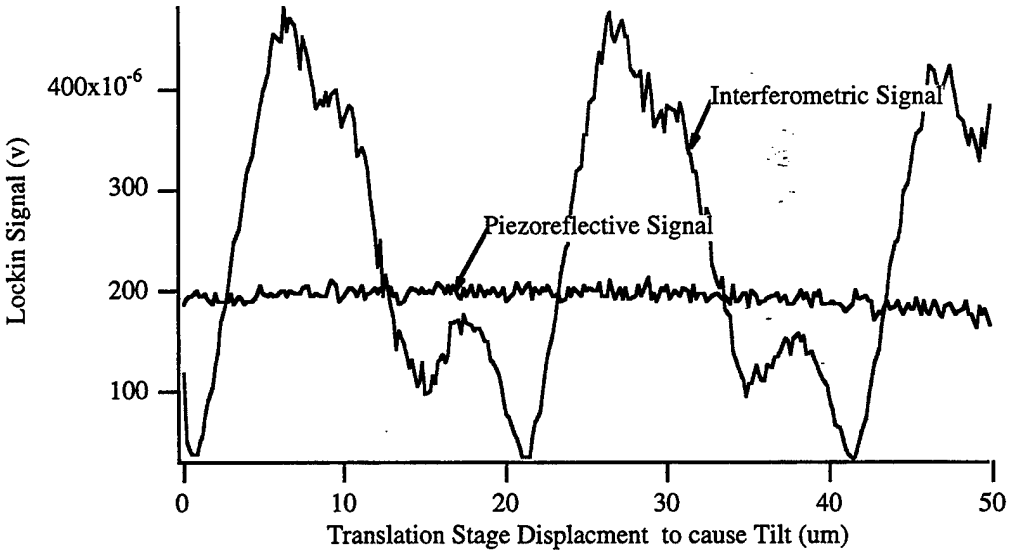

Figure 20. Piezoreflective signal as a function of specimen tilt, and the corresponding interferometric signal.

17. Now, at last, the interferometric response of the specimen can be measured. The program is automated such that both the magnitude and phase can be recorded for different tilt angles.

4. MODEL

4.1 Heating Beam Absorption by the Specimen

To predict the temperature rise of the specimen due to the absorption of the ultrafast laser pulse, and hence the magnitude of the ultrasonic wave which is generated, it is necessary know how much of the incident laser pulse will be absorbed by the specimen. The optical properties and reflection coefficients necessary to calculate how much light will be absorbed are tabulated in Table 2 (Born, 1970 and Gray, 1973).

Table 2. Optical Properties of Metals at 589.3 nm.

Material	n	nk	R	d nm
Aluminum	1.80	7.12	0.877	8.5
Gold	0.14	4.26	0.971	14.2
Iron	3.69	3.94	0.606	15.3
Magnesium	0.48	3.71	0.880	16.3
Molybdenum	1.03	1.22	0.265	49.6
Nickel	2.37	4.21	0.674	14.3
Tin	1.48	5.25	0.830	11.5
Zinc	3.75	4.62	0.650	13.1

4.2 Temperature Rise of the Specimen

The increase in the temperature of a specimen due to the absorption of a given amount of light depends on the thermal properties of the material. The thermal properties (Gray, 1973, Kakac, 1993 and Ozisik, 1980), temperature increases (using the finite difference method) and melting points (Kittel, 1986) are tabulated in Table 3.

Table 3. Thermal Properties of Metals

Material	Density kg/m^3	Specific Heat $J/m^3°C$	K W/mK	Maximum Temperature °C	Melting point °C
Aluminum	2692	900	222	8.50	660
Gold	18880	130	297	1.24	1065
Iron	7860	460	75	11.77	1538
Magnesium	1740	1040	159	6.33	649
Molybdenum	10200	251	135	9.72	2622
Nickel	8900	440	92	9.55	1455
Tin	7300	225	67	14.20	232
Zinc	6920	382	112	15.69	419

To validate the finite difference calculation, the temperature rise as a function of distance into the specimen is plotted in Figure 21 along with the results Maris's and Carslaw and Jaeger's theories. These theories agree except at the very surface of the specimen where the temperature gradient is the highest. This dis-

crepancy between Maris's theory and the other theories is due to the fact that Maris's theory does not take into account heat conduction. When the thermal conductivity of the material is set to zero, all three theories predict the same temperature. The overall conclusion then, is that all three of the theories are consistent with each other, and that the finite difference model is equivalent to the analytical theories. Once the heating pulse is finished, however, only the finite difference simulation can predict the subsequent decrease in the temperature of the specimen, which is necessary to model the thermoreflectance cooling curves.

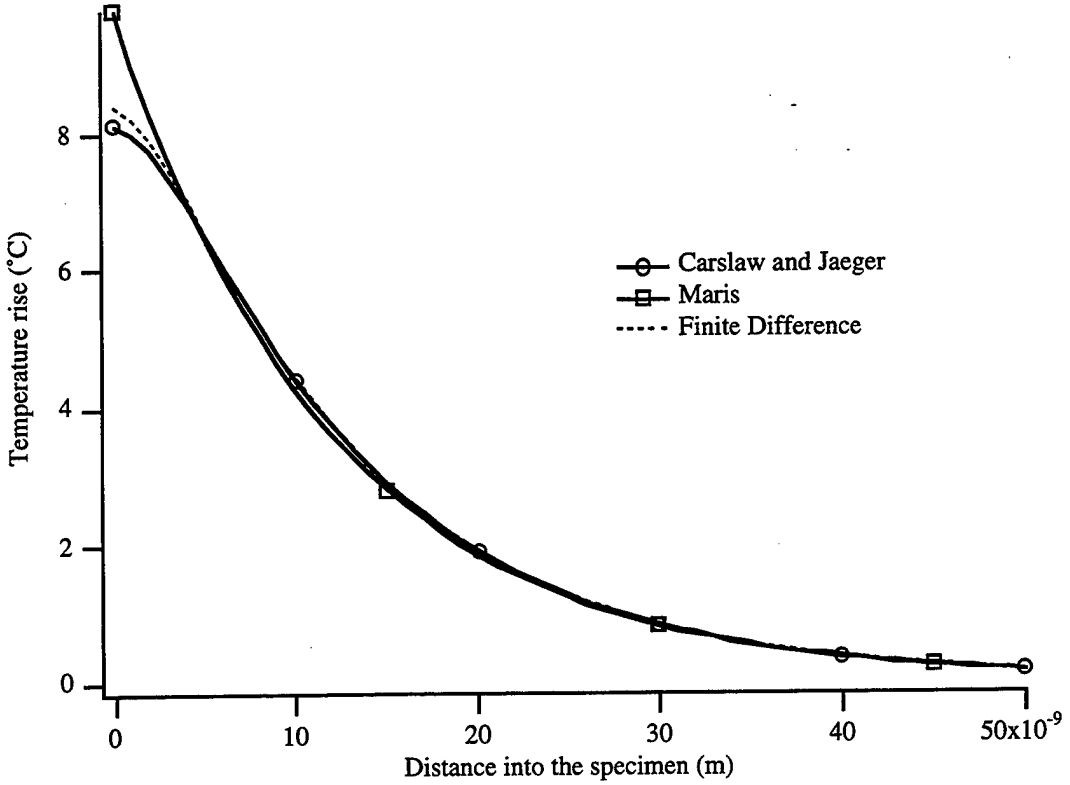

Figure 21. Temperature rise as a function of depth into the material for Al at the end of a 100 fs heating cycle.

The second conclusion to be drawn from Figure 21 is that the frequency of the ultrasound which is generated will depend upon the optical absorption coefficient of the material, not the pulse length. For Nd:YAG lasers, where the pulse length is longer than 10 ns, there is sufficient time for the heat to propagate, and lower frequency ultrasound is generated. For ultrashort pulses of light, virtually no conduction of heat occurs while the heating pulse is still on, a conclusion which is validated by Thomsen (Thomsen, 1986). Since conduction does not determine the ultrasonic pulse length, it must instead be determined by the shape of the initial temperature profile, which is determined by the optical absorption length of the material.

The temperature profiles for different metals are plotted in Figure 22. The laser properties were taken from Table 1, and the optical and thermal properties for the different materials were taken from Tables 2 and 3. The sharp temperature gradients of aluminum and nickel suggest that these materials will generate higher frequency ultrasound than gold or molybdenum.

The finite difference temperature profiles showing the cooling of an aluminum specimen as a function of time are shown in Figure 23. These temperature profiles behave as expected, with the heat diffusing into the bulk of the specimen as time passes.

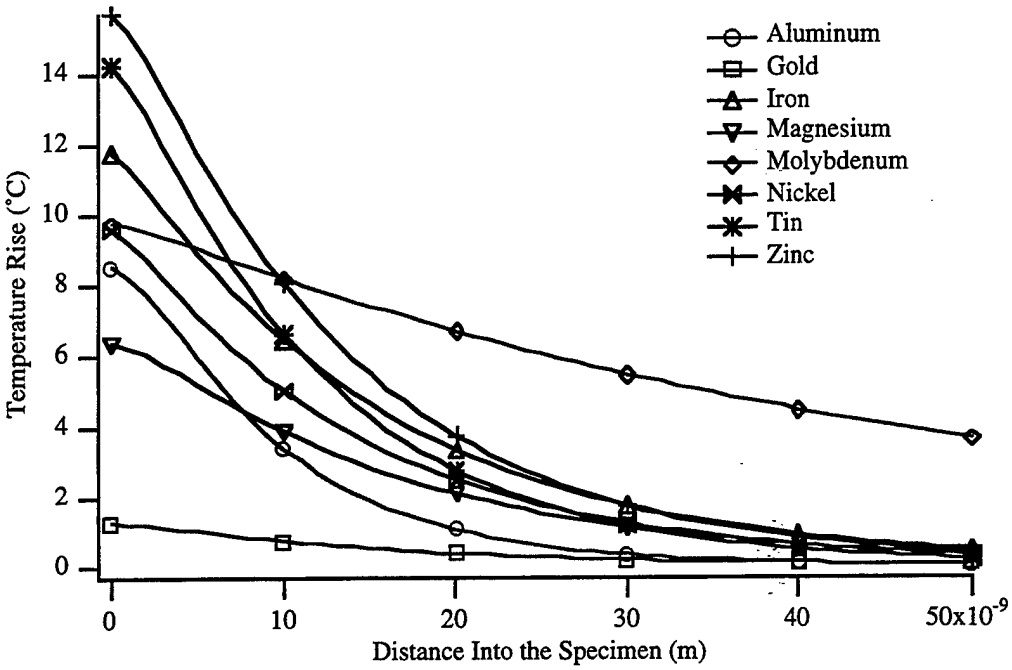

Figure 22. Temperature Rise as a function of material and distance into the specimen. These profiles were calculated using the values in Tables 2 and 3.

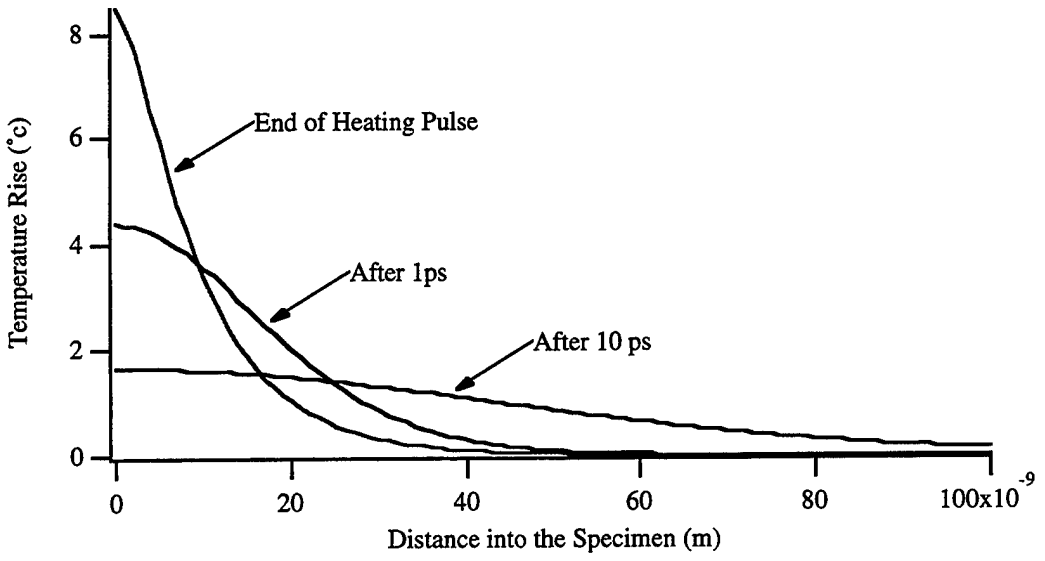

Figure 23. Temperature rise in an aluminum specimen as a function of depth into the specimen and time after the heating pulse ended.

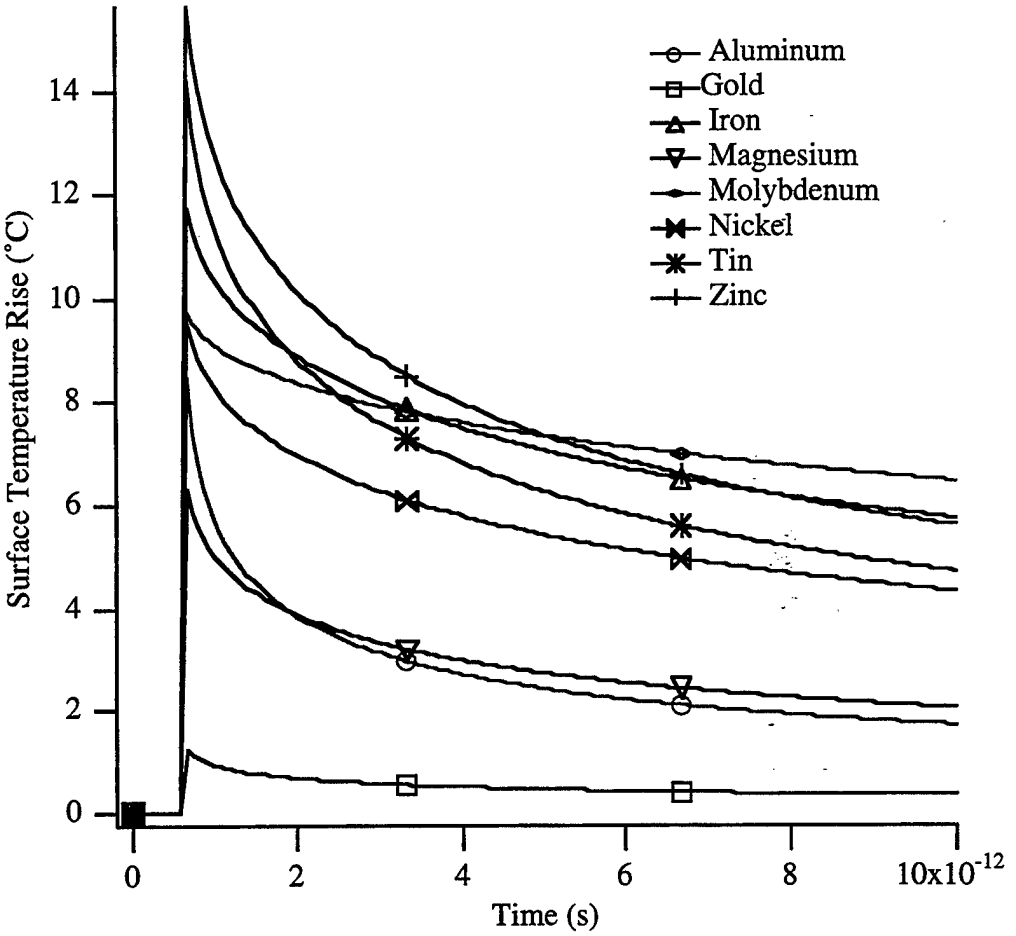

Figure 24. Surface temperatures as a function of time.

What is more interesting is to plot the surface temperature as a function of time, because it should have the same shape as the experimental thermoreflectance curves. Eesley demonstrated that, for nickel coatings, the thermoreflectance signal is linear with respect to the surface temperature of the specimen as calculated using a finite difference theory (Paddock, 1986). The surface temperature as a function of time after the heating pulse is plotted in Figure 24.

4.3 Generation of Ultrasound

The initial stress wave generated by the heating beam was calculated from the temperature profile at the end of the heating pulse using the equations of section 2.2. The bulk modulus and linear elastic expansion coefficients are given in Table 4 (Bolz, 1973 and Gray, 1972).

Table 4. Elastic Properties of Metals

Material	Bulk Modulus GPa	Thermal Expansion Coefficient μm/m	Maximum Stress MPa	Yield Stress MPa
Aluminum	77.6	23.0	43.54	41
Gold	169.0	14.2	8.74	
Iron	167.7	11.7	66.32	131
Magnesium	36.4	26.0	17.52	90
Molybdenum	272.5	5.0	39.33	
Nickel	21.7	13.3	7.92	103
Tin	41.8	23.0	39.08	24
Zinc	70.0	29.7	93.93	

4.4 Propagation of Ultrasound

The initial stress distribution propagates in both directions. The wave going in the negative direction reflects off the free surface and then propagates in the positive direction. This is shown in Figure 25 for three different times.

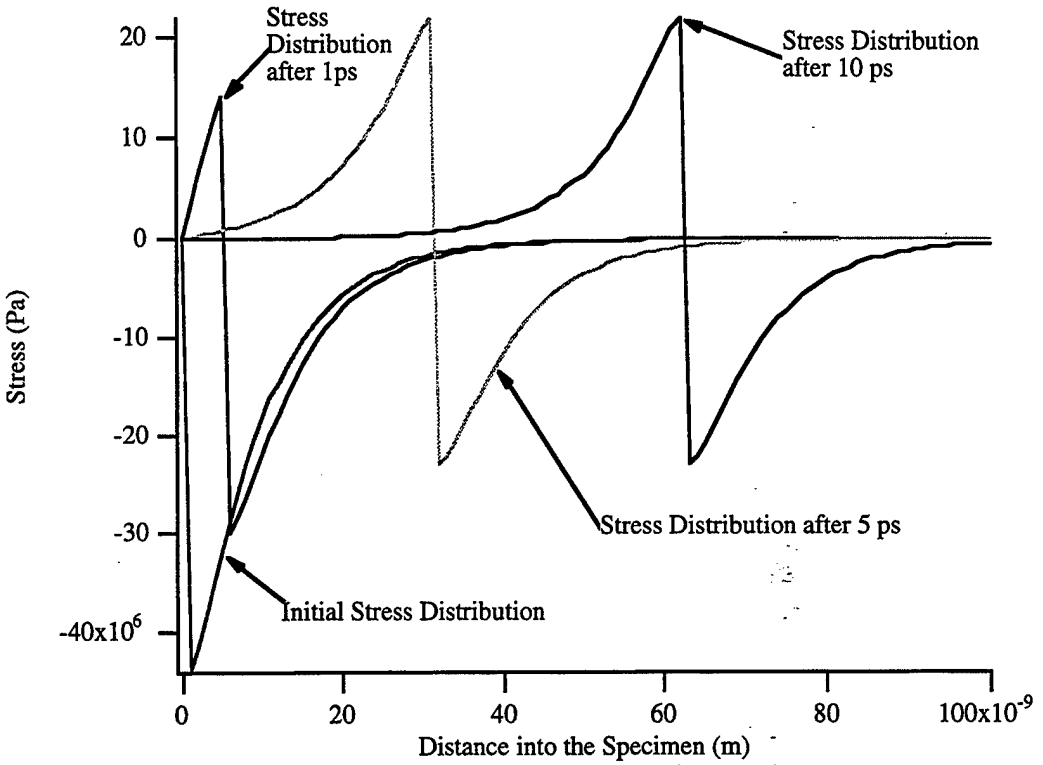

Figure 25. Propagation of the ultrasonic stress wave in aluminum.

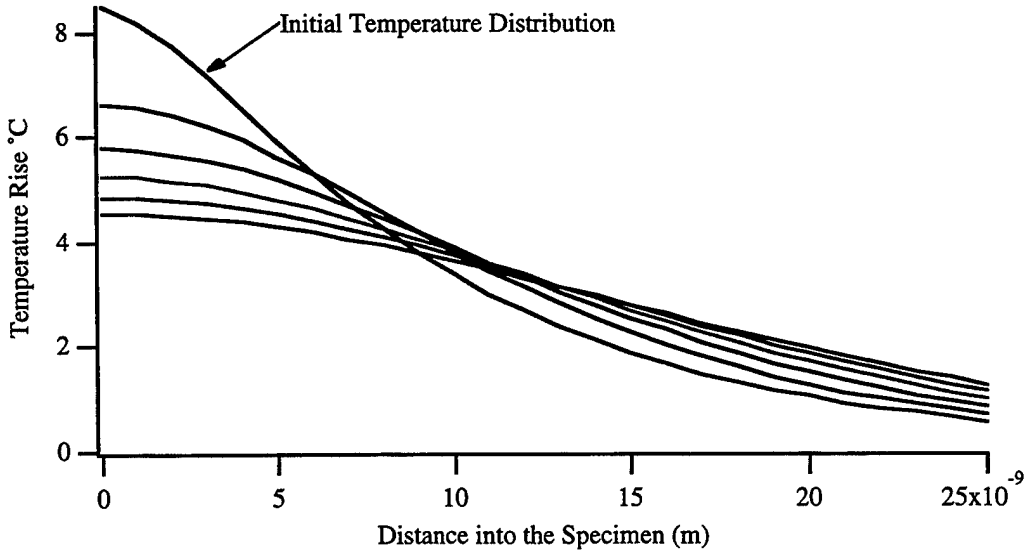

Figure 26. Temperature profiles for an aluminum specimen as the ultrasonic wave propagates in 1nm steps.

Note how, after the initial stress pulse is generated, the stress at the surface, z = 0, is always zero, as was predicted by the theory in Section 2.3.

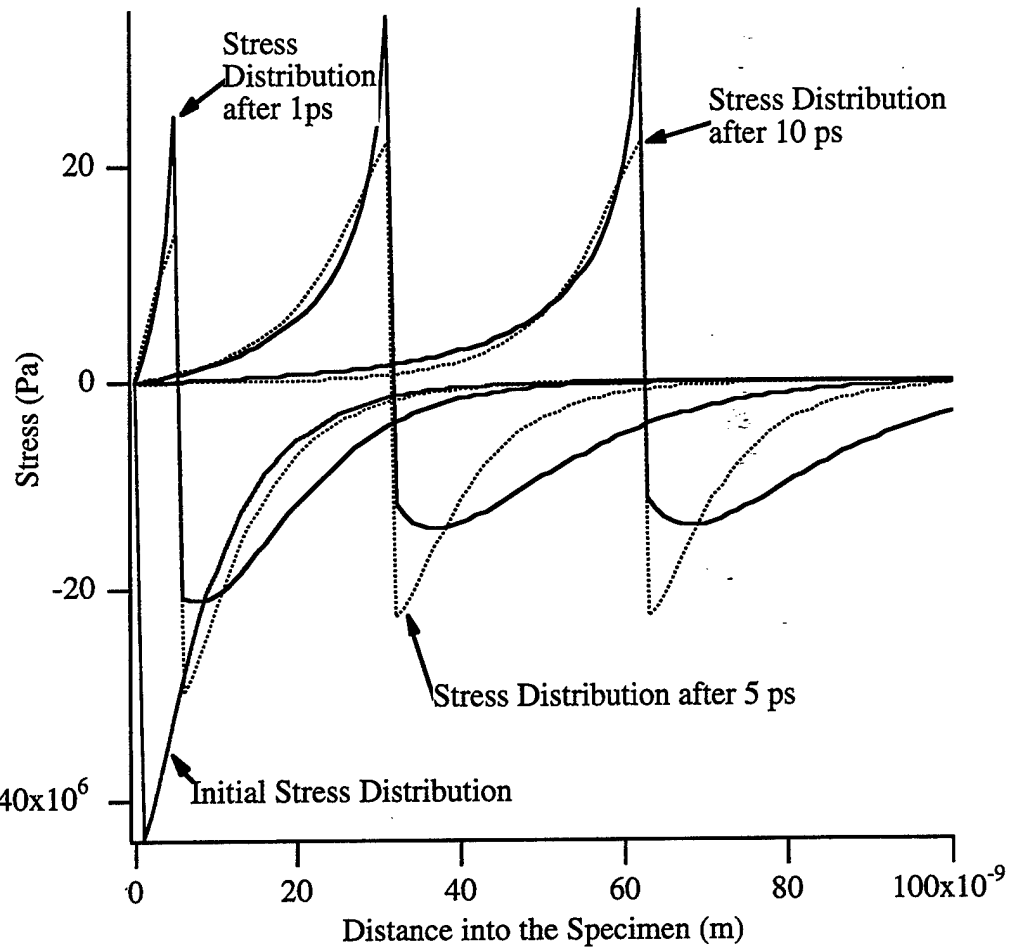

Figure 27. Comparison of ultrasonic waves generated by assuming minimal cooling (dotted curves) and the cooling which would be expected in aluminum (solid curves) for ultrasonic waves at 0, 1, 5 and 10 ps.

Experimentally, however, the bipolar waveforms shown in Figure 25 have not been observed. The model needs to be refined, and the obvious improvement is to remove the assumption that cooling of the surface is negligible.

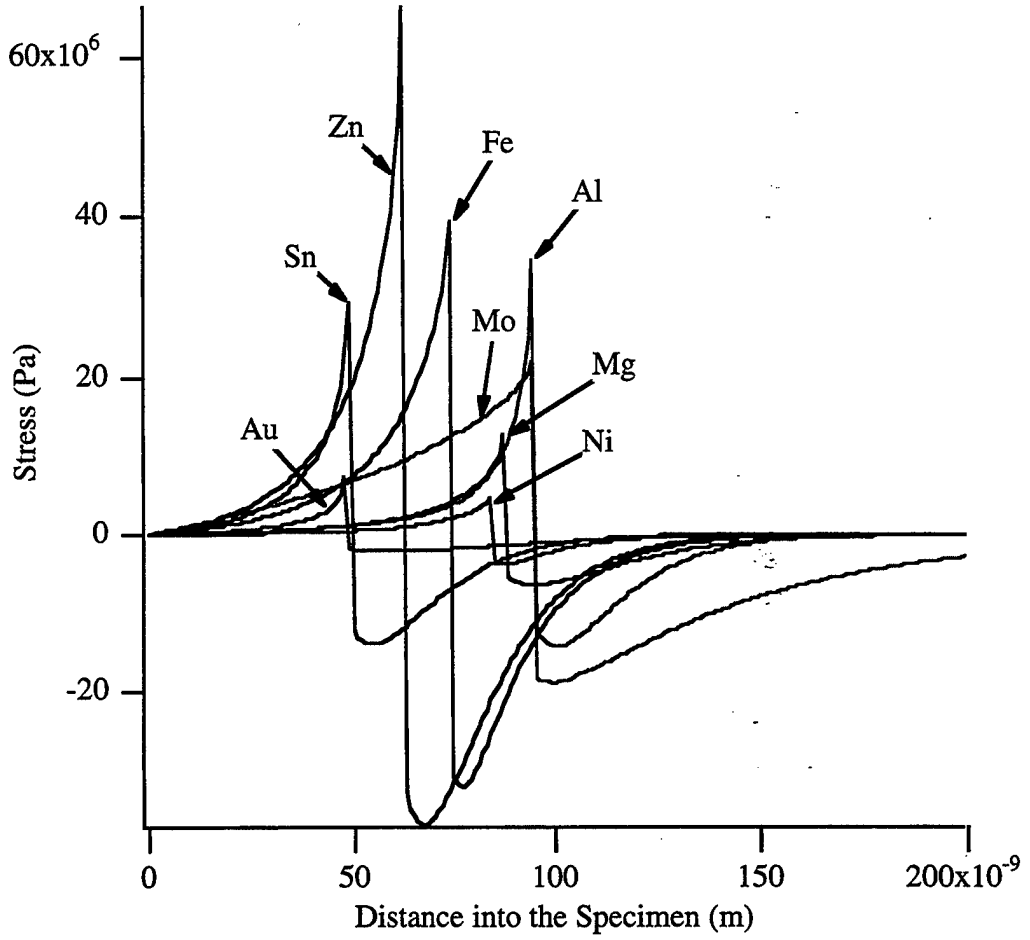

Figure 28. Stresses after the ultrasonic waves have propagated for 15 ps.

Figure 26 shows that the temperature profile changes significantly as the ultrasonic wave propagates 5 nm in 1 ps. The temperature drop as the wave propagates the first nanometer is 20% as large as the initial temperature rise. When these temperature drops are included in the model for the generation of ultrasound, the waveforms shown in Figure 27 are obtained. These waveforms approach the unipolar shape which has been observed experimentally.

The ultrasonic waveforms for eight metals are shown in Figure 28. Molybdenum and zinc, which both have low thermal conductivities, approach the bipolar waveforms predicted in Figure 25, while aluminum and gold, both good conductors, approach a unipolar pulse.

4.5 Attenuation of Ultrasound

Ultrashort pulses of ultrasound are attenuated by both absorption during propagation, and by transmission into the substrate as it is encountered. The absorption of ultrasound depends on the material and how it was processed. It is not possible to predict this specimen dependant absorption. The attenuation due to transmission of the ultrasonic energy into the substrate can, however, be calculated from the acoustic impedances of the coating and substrate (Auld, 1973). The longitudinal velocity of sound (Chimenti, 1979), the density (Gray, 1972), acoustic impedances, and reflection coefficients between metal coatings and substrates are given in Table 5.

Notice that only 14% of the amplitude of an ultrasonic wave incident on glass substrate from an aluminum coating is reflected. This much energy loss in the reflected wave makes it difficult to detect the ultrasonic waves. If instead, a layer of gold is placed between the aluminum and glass, the reflection coefficient increases to 57%, and the ultrasonic echoes are detectable.

Table 5. Ultrasonic Reflection Coefficients.

Material	Acoustic Velocity m/s	Density kg/m^3	Acoustic Impedance $10^6 kg/m^2s$	Reflection Coef. Glass	Reflection Coef. Gold
Aluminum	6320	2629	16.62	-0.14	0.57
Gold	3240	18880	61.17	-0.66	0.00
Iron	5000	7860	39.30	-0.52	0.22
Magnesium	5820	1740	10.13	0.10	0.72
Molybdenum	6290	10200	64.16	-0.68	-0.02
Nickel	5630	8900	50.11	-0.60	0.10
Tin	3320	7300	24.24	-0.32	0.43
Zinc	4170	6920	28.86	-0.40	0.36

4.6 Ultrasonic Surface Displacements

The displacement of the surface of a thin coating is modelled by adding the strains in all the finite difference elements together. For an elastic wave which has as much compressive strain, shown by area A in Figure 29, as tensile strain B, the strains cancel each other and there is no net displacement. If the ultrasonic wave is in the process of being reflected by the specimen surface as shown in Figure 30, the compressive strain C is larger than the tensile strain F and a net displacement of the surface of the specimen results. The strain F was obtained using superposition to add together the part of the ultrasonic wave going in the negative direction which has already reflected off the free surface, area E, and the part of the wave

which has not yet reflected, area D.

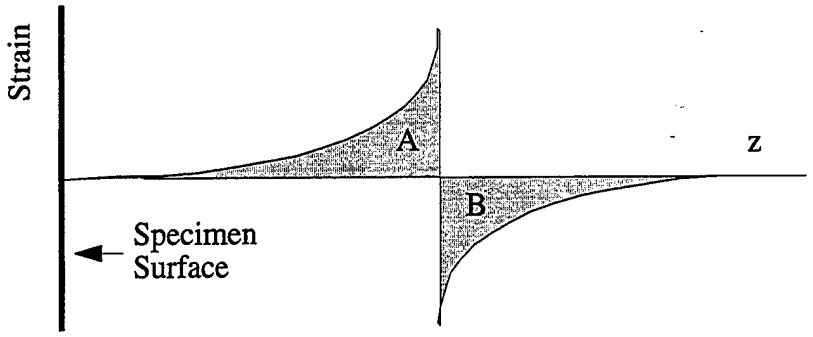

Figure 29. Strains before an ultrasonic wave reaches the free surface.

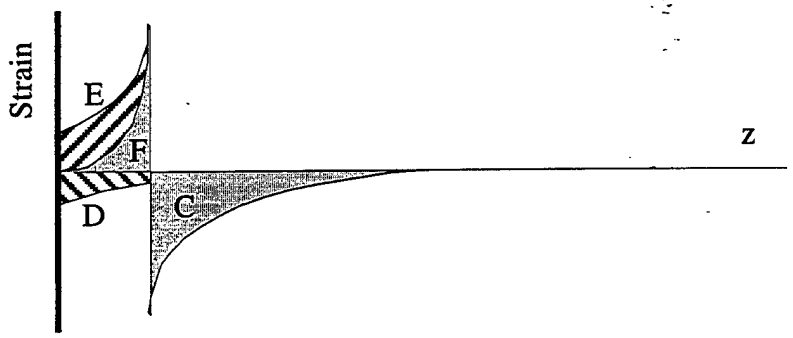

Figure 30. Strains as an ultrasonic wave is reflected by a free surface.

Ultrasonic waves which are unipolar will always have a net displacement, which changes from a net positive displacement to a net negative displacement after the wave reflects off a free surface.

The displacement of the coating surface as function of time while the ultrasonic waves are in the process of being reflected is plotted in Figure 31 for eight metals. Each point along this plot is the total displacement of the coating, and the peaks in the displacements are caused when the strains in the ultrasonic wave sum

together constructively. The plot for zinc is a good example of the overall change from an overall negative displacement of the coating before the wave is reflected to an overall positive displacement after the wave has been reflected.

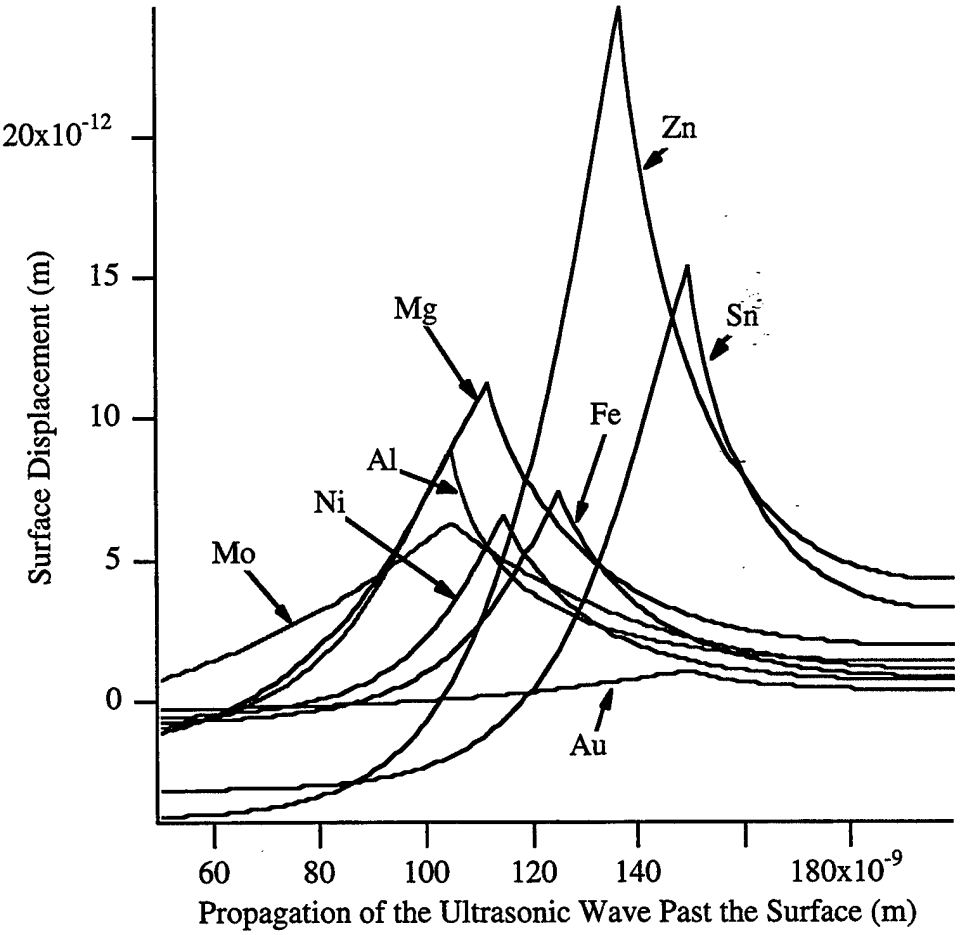

Figure 31. Displacement of the surface of the specimen as the ultrasonic wave passes the interface.

4.7 Thermal Wave Generation

The heating beam must be chopped in order to use lock-in detection to measure small changes in reflectivity. A chopped heating beam, however, generates thermal waves. Three different theories to predict the temperature distribution due to thermal waves were developed in Section 2.4. The assertion was made that, because the coating was thin relative to the time it took to conduct heat across the coating, the temperature did not vary significantly over the thickness of the coating. To validate this assertion, the temperature as a function of depth into the coating is plotted in Figure 32 for a relatively thick coating (500 nm) of aluminum. All three theories show a negligible change in the temperature across the coating.

The temperature rise due to constant heat flux on an infinite half space is much lower than the rise predicted by both the Carslaw and Jaeger heat flux on a layer theory or by the Rosencwaig theory. This is to be expected, however, because the heat does not hit an insulating boundary, and can therefore be absorbed by a lot more material. As the chopping frequency is increased, however, the heat does not have enough time to diffuse to the edge of the coating, and the three theories converge as shown in Figure 33. Note that the solution for the half space shows the classic $\frac{1}{\sqrt{f}}$ dependence which is typically observed in thermal wave experiments. It is only when the coating is thin enough for the heat to diffuse all the way through it that a $\frac{1}{f}$ dependence is observed.

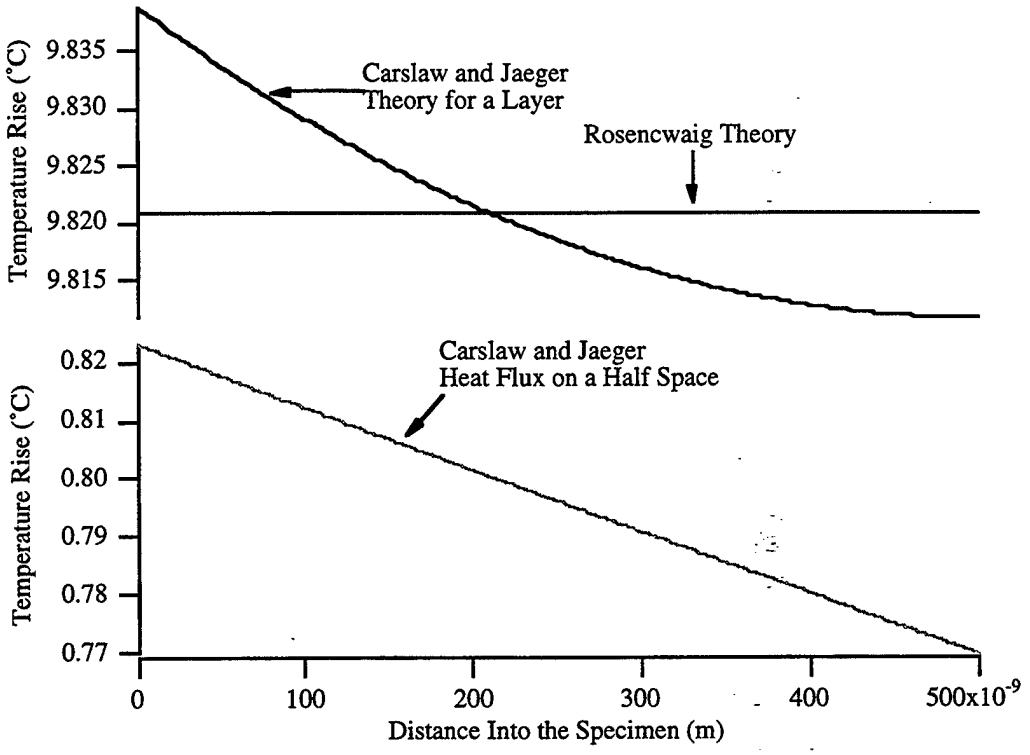

Figure 32. Thermal wave temperature as a function of distance into the coating.

If the chopping frequency is increased even further, so that the period of a heating cycle approaches the time period of the ultrafast laser pulse, the theory for a prescribed heat flux does approach the theories for the ultrafast pulse.

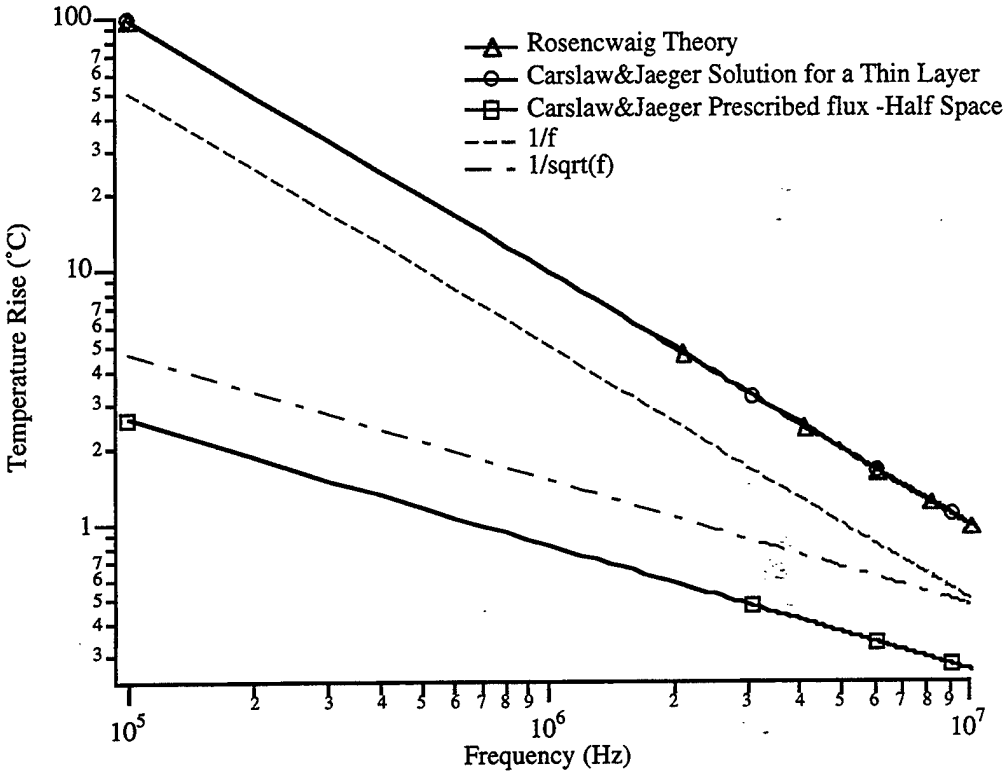

Figure 33. Thermal wave temperature rise as a function of frequency.

4.8 Summary

The UFLGU inspection process is modelled using the theories developed in Chapter 2. The temperature rise of the specimen as a function of time and position is modelled using the finite difference algorithms. The generation of the ultrasonic wave is modelled using the linear thermal expansion coefficient, and the attenuation of the wave

The theories developed in Chapter 2 have been used to simulate the UFLGU inspection process. The temperature of the specimen due to the absorp-

tion of the heating pulse and subsequent cooling is modelled using the finite difference simulation. The thermal stresses which generate the ultrasonic pulse are modelled using the linear thermoelastic theory, and the magnitude of the stress waves are predicted. The displacement of the surface of the specimen due to the ultrasonic wave is predicted by summing all of the strains, and the displacements which will be seen experimentally are predicted.

These models will be compared to actual data in the next chapter.

5. EXPERIMENTAL RESULTS

5.1 Interferometer with Piezoelectric Excitation

Interferometers capable of resolving picometers of displacement have been constructed (Scruby, 1990), and pulsed interferometers have been constructed (McKie,1994), but no known interferometer using Ti:sapphire ultrafast pulses has been reported. To demonstrate that interferometry is possible with Ti:sapphire pulses, the interferometer was first tested on a specimen which was excited with a conventional piezoelectric transducer. The experimental configuration, showing the transducer located to excite only the signal beam of the interferometer, is shown in Figure 34.

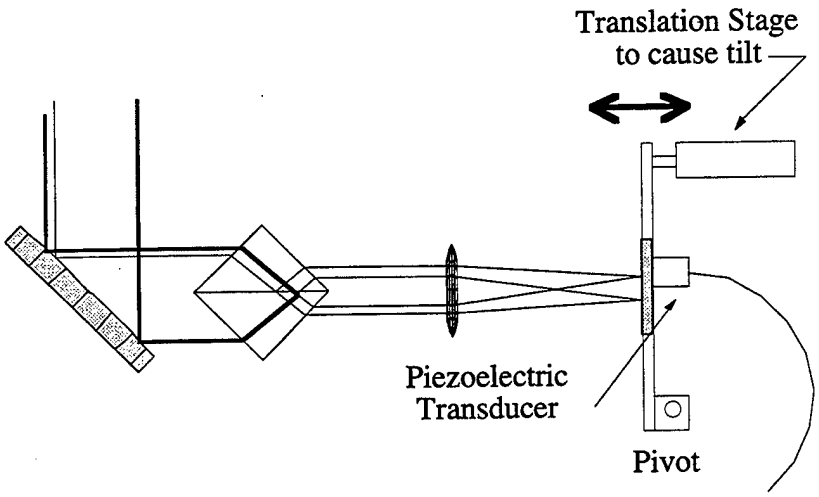

Figure 34. Interferometric detection of ultrasound generated with a piezoelectric transducer.

The piezoelectric transducer was a 1 MHz, 0.5 inch diameter, Panametrics transducer, which was designed to be used with polystyrene wedges. The speci-

men was a glass microscope slide coated with a thick coating (approximately 600 μm) of aluminum. The transducer was placed in a jig which pressed it against the microscope slide, and ultrasonic grade honey was used to couple the longitudinal waves from the transducer into the slide. The transducer was excited with a 1 MHz sine wave from the function generator.

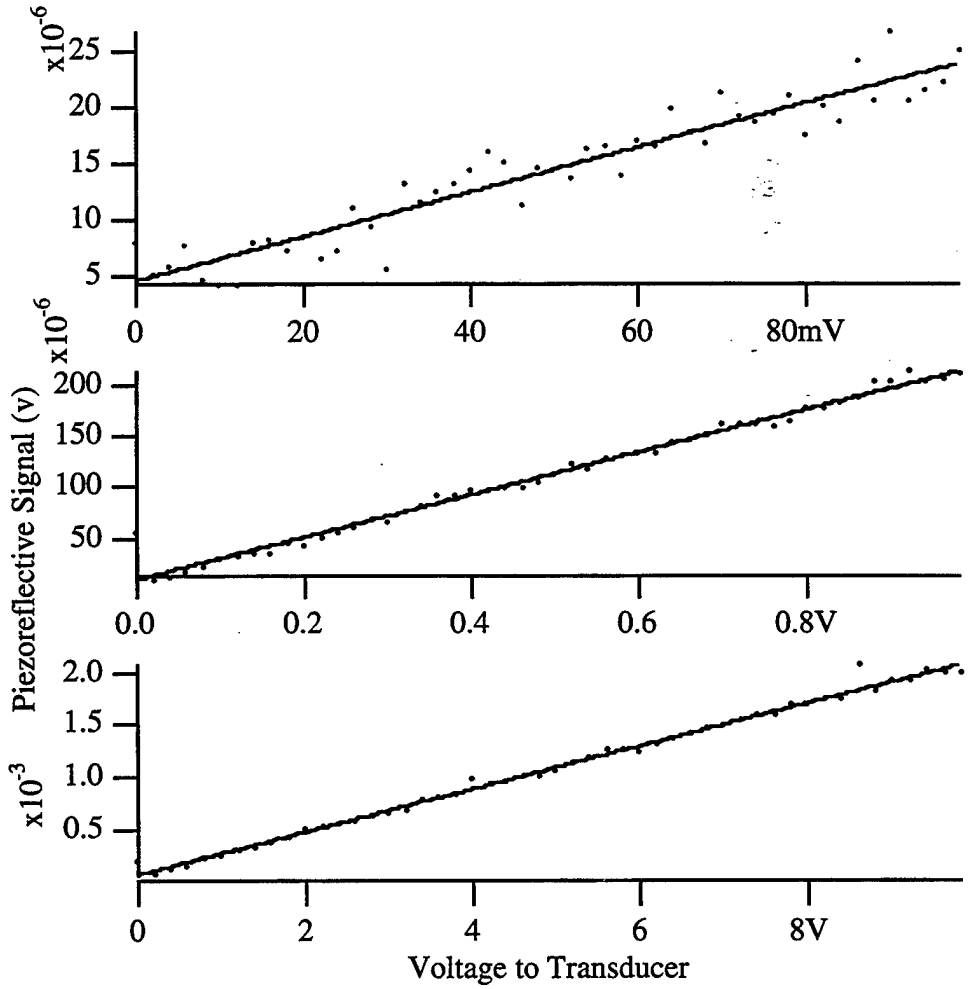

Figure 35. Piezoreflective signal as a function of voltage to the piezoelectric transducer.

The interferometer was converted to piezoreflective detection by blocking the reference beam. The piezoreflective signal from the aluminum coating remained linear as the voltage to the transducer was varied from 10 mV to 10 V (Figure 35).

The interferometer was converted back to interferometric detection, and the sensitivity of the interferometer was measured as a function of phase difference between the reference and signal arms. This relative phase change is accomplished for an interferometer in this configuration by tilting the specimen. The interference signal, and the magnitude and phase of the interferometer signal are plotted in Figure 36. The interference curve exhibits the classic $(1 + \cos\delta)$ dependence. Since the excitation of the transducer, and therefore the displacement of the surface of the specimen, remains constant as the specimen is tilted, the interferometric signal will be proportional to the sensitivity of the transducer. This sensitivity is proportional to the slope of the interference curve, which shows that the interferometer is operating as a classic Michelson interferometer. More importantly, this result demonstrates that the light in Ti:sapphire laser pulses is coherent enough to use for interferometry.

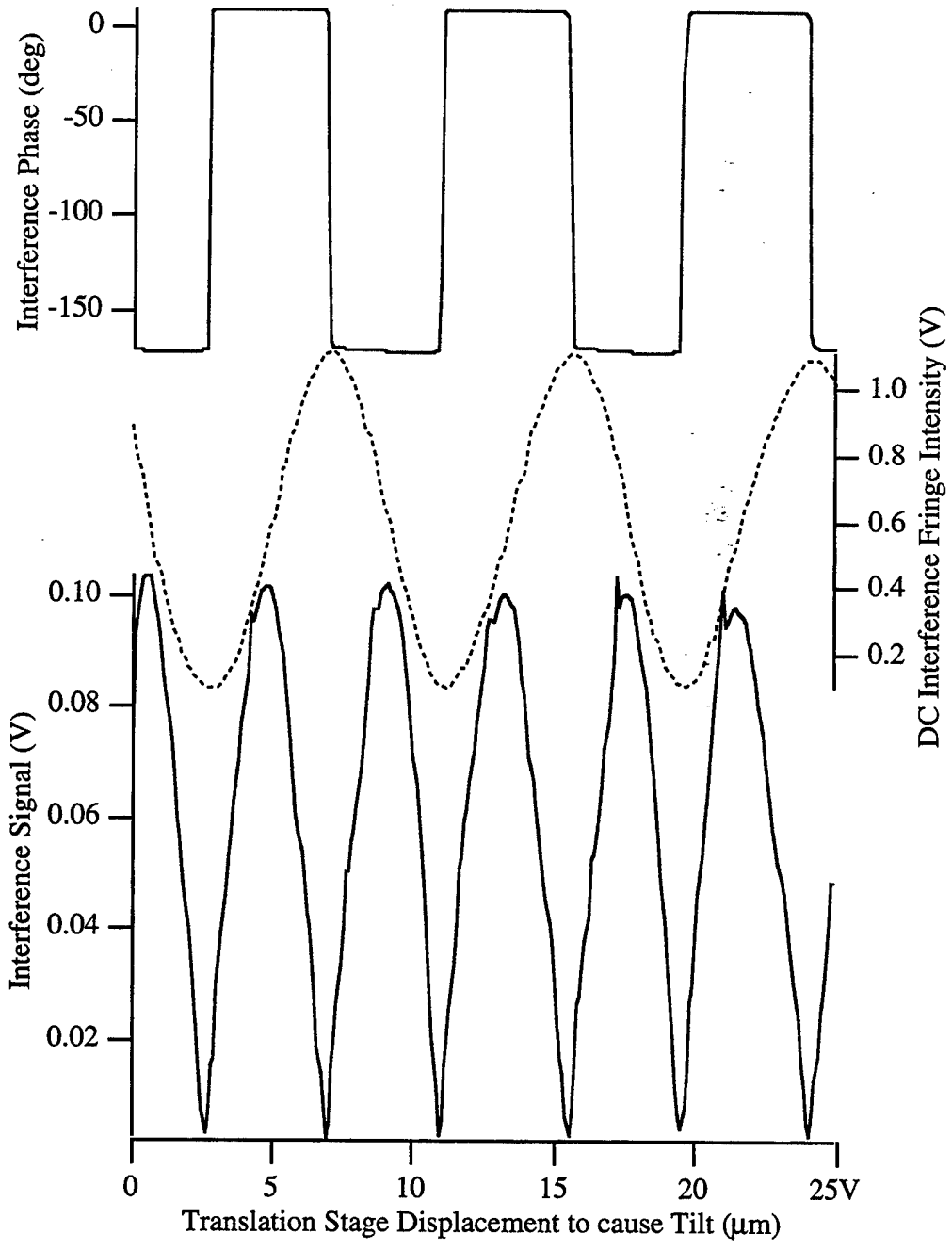

Figure 36. Interferometric signal as a function of phase delay between arms of the interferometer. The excitation was a 1 MHz piezoelectric transducer driven by 10V p-p sinusoid.

5.2 Thermoreflective Detection of Thermal Waves

The thermoreflectivity, the change in reflectance for a given change in temperature, will be measured using the thermal wave signal. The temperature change due to thermal waves can be calculated from the Rosencwaig model, and the change in reflectance will be measured experimentally. These thermoreflectivities can then be used with the finite difference model to predict the shape of the thermoreflectance cooling curve.

The interferometer is converted to piezoreflective detection by blocking the reference beam as shown in Figure 37.

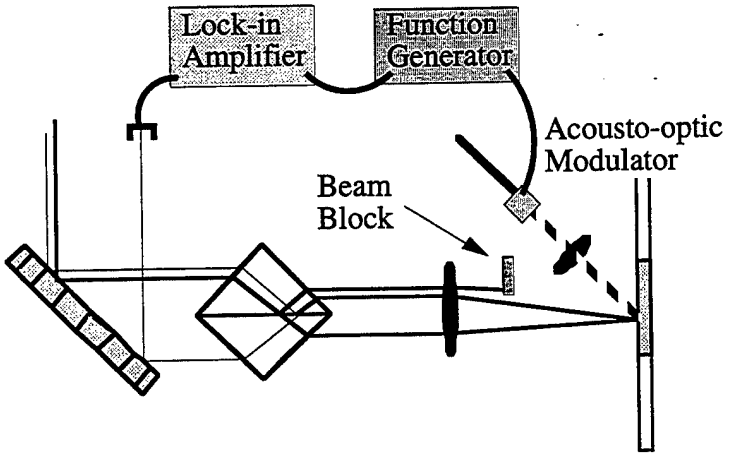

Figure 37. Experimental configuration for the thermoreflectance experiment.

The delay line is set such that the probe pulse arrives before the heating pulse, so that any transient effects from the previous ultrafast pulse will have died out by the time the probe pulse arrives.

The data for an aluminum coating, shown in Figure 38, exhibit the $\frac{1}{f}$ dependence which was predicted by the thermal wave model. At frequencies below 50 kHz the heat has time to propagate through the coating, so that the thermal waves are measuring the properties of both the coating and the substrate.

The temperature increase due to the thermal waves was modelled using Rosencwaig's theory. Recall that the temperature rise is given by:

$$T(0,t) = \frac{I_0 \alpha i}{2\omega\kappa l} \tag{5.1}$$

The change in signal S is then given by (5.2):

$$S = T\tau S_{DC} = \frac{I_0 \alpha i}{2\omega\kappa l}\tau S_{DC} \tag{5.2}$$

The temperature profile is plotted in Figure 39, and for 1 MHz the model predicts a temperature rise of 9.8 °C. The data for a 200 nm thick aluminum coating were also plotted, and the thermoreflectance coefficient τS_{DC} was found to be $8\text{x}10^{-7}$ V/°C, and $\tau = 3.63\text{x}10^{-7}\ \frac{\Delta R}{R} C$. This value of τ is significantly less than the 10^{-5} to 10^{-4} range that Rosencwaig cites as typical for most materials (Rosencwaig, 1985). Of course, the reference Rosencwaig cites (Gray, 1972), is dealing with the refractive index of special crystals and glasses, and that data may not extrapolate to metals.

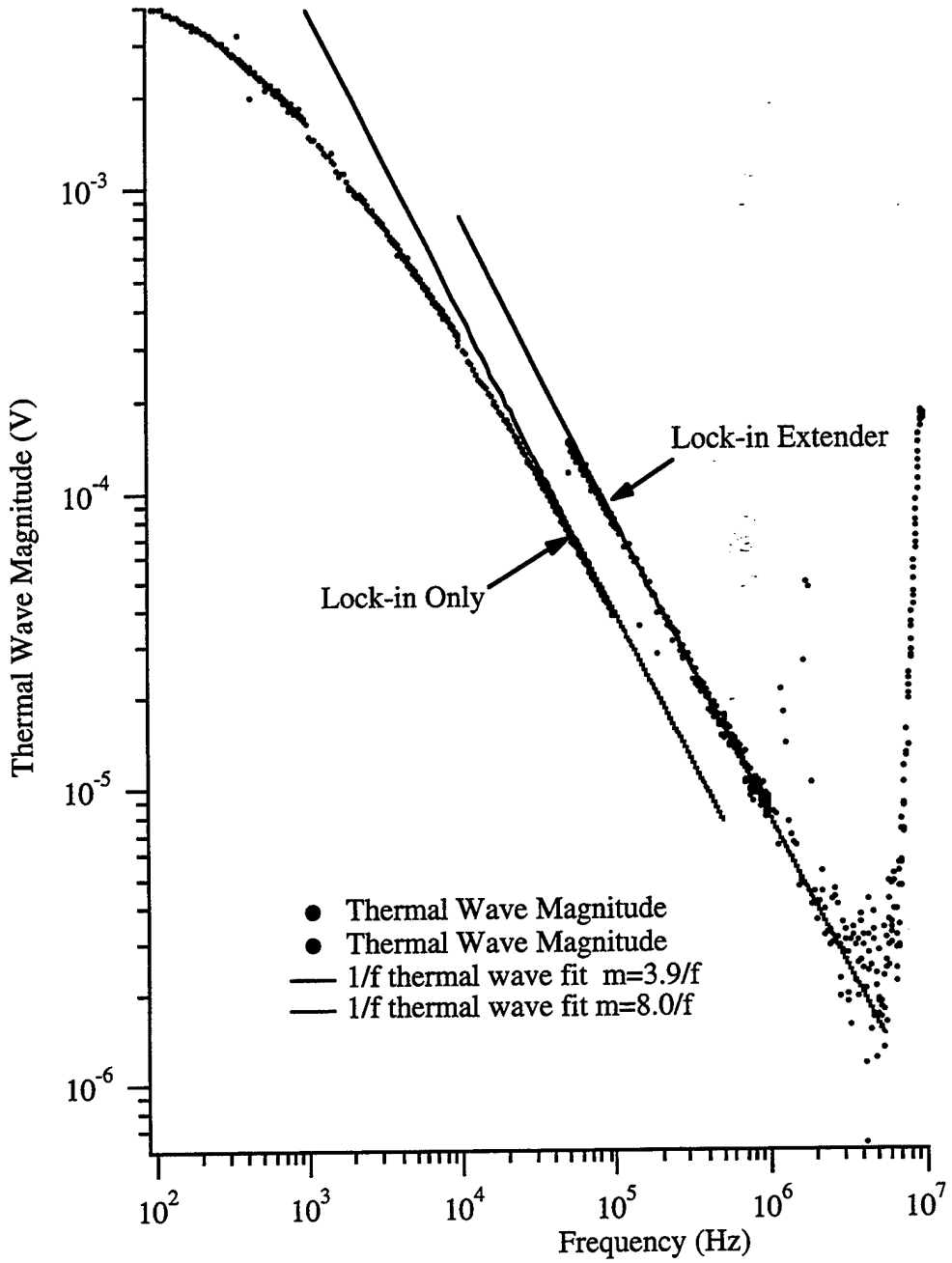

Figure 38. Thermoreflectance signal for a 200 nm thick layer of Al over 300 nm of AuPd. The lower frequency data were taken with just the lock-in amplifier, and the high frequency data were taken using the lock-in extender also.

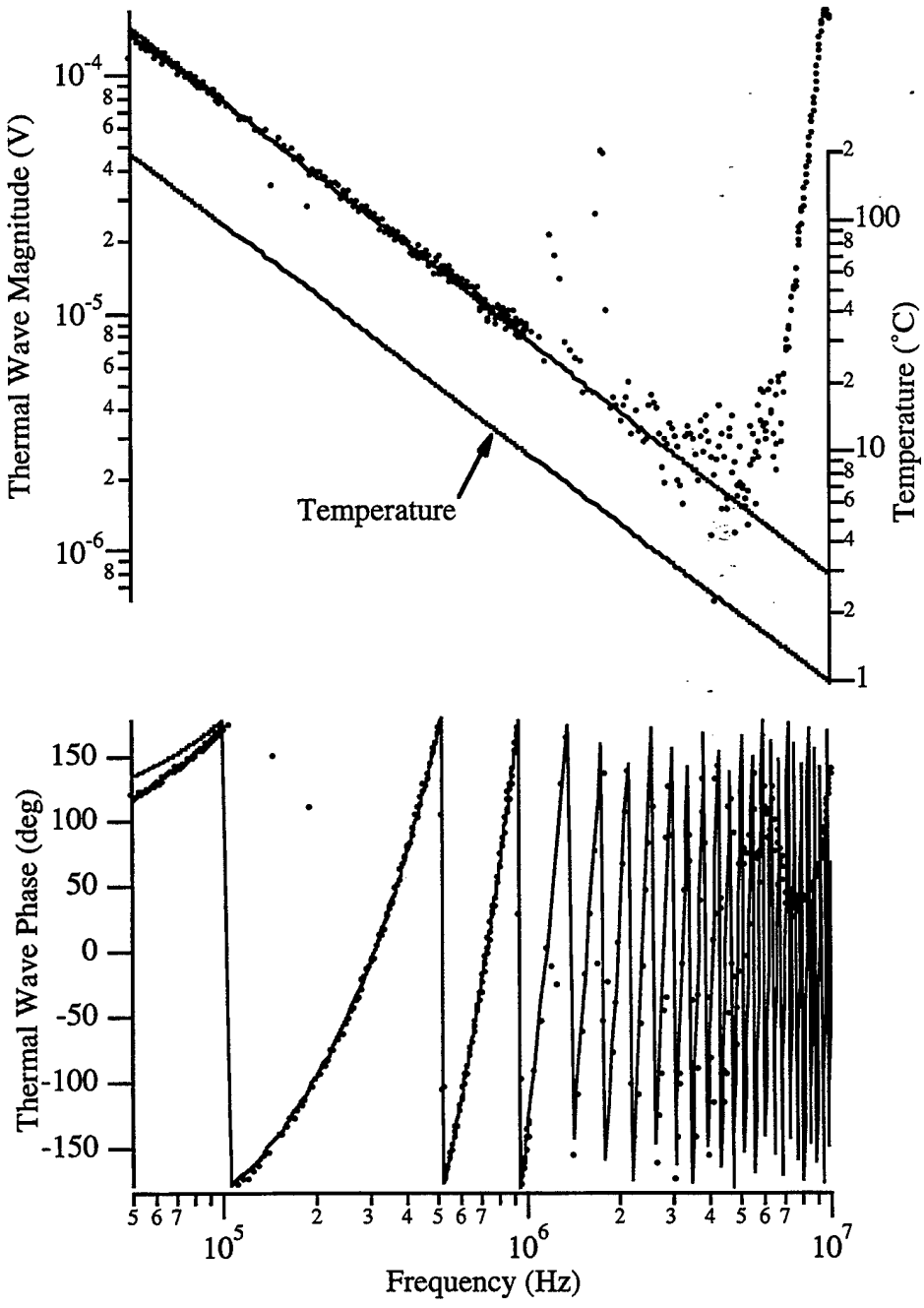

Figure 39. Modelling of the detection of thermal waves for a 200 nm thick layer of Al over AuPd.

The phase signal in Figure 39 varies linearly with frequency at a rate of 8.6×10^{-4} deg/Hz. This behavior could be due to a fixed time delay in the system response.

The magnitude signal in Figure 39 shows transmission line peaks and nulls starting at 2 MHz. It is suspected that these effects were due to the cable between the photodetector and the lock-in. Later work will be directed at reducing this effect so that experiments can be conducted at frequencies up to 10 MHz, which will allow the thermal wave component of the signals to be reduced even further.

5.3 Interferometric Detection of Thermal Waves.

5.3.1 Molybdenum

Typically interferometers only measure the displacement of the surface of the specimen because the reflectivity of the specimen does not vary significantly, and the intensity of the interferometer beams remains constant. For these experiments, however, the interferometer is sensitive both to surface displacements and to changes in the reflectivity of the specimen. Because both the displacement signal and thermoreflectance signals have the same frequency but different phases, the lock-in amplifier will add the two signals vectorially. To demonstrate that this pulsed interferometer is equivalent to a Michelson interferometer for measuring thermal wave displacements it is necessary to minimize the thermoreflectance sig-

nal. In order to do this, a molybdenum specimen, which is only very weakly thermoreflective, was used.

A 200 nm layer of molybdenum was sputtered onto glass by Peter Shull at Johns Hopkins University. The piezoreflective signal for this specimen is shown in Figure 40, and has a value which is only 10% as high as the interference peaks. Although the difference in height between successive peaks is not large, it is still about twice as high as the piezoreflective signal. If the piezoreflective signal is subtracted off the interferometric signal (vectorially, of course), successive peaks should have the same height, and this is indeed the case as shown in Figure 41.

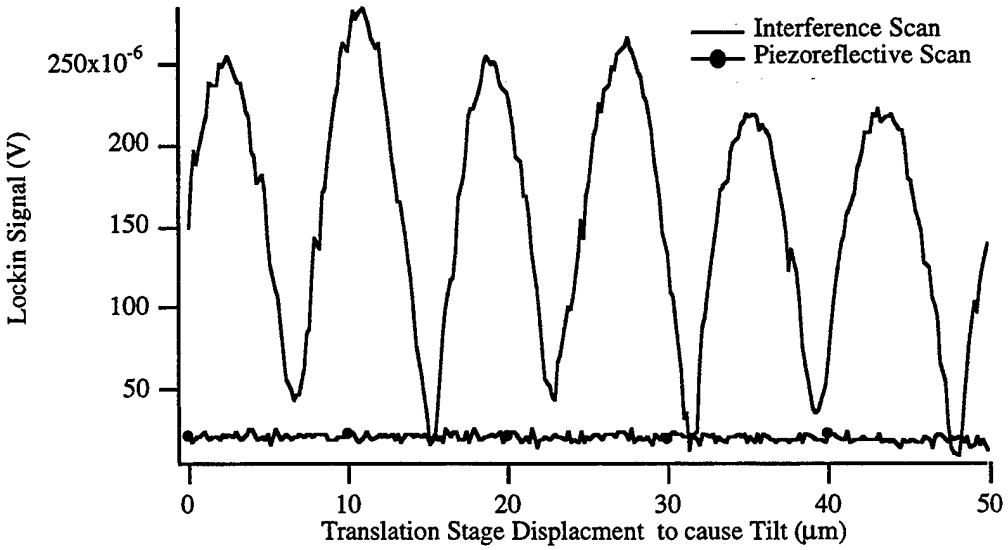

Figure 40. Interferometric and piezoreflective signals from molybdenum as a function of tilt.

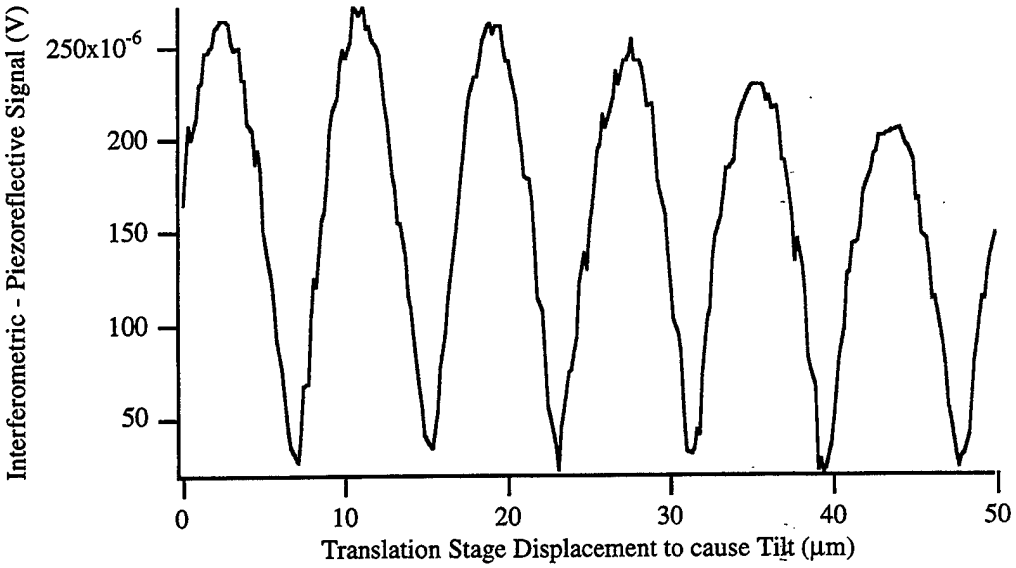

Figure 41. Magnitude of the interferometric signal after subtracting out the piezoreflective signal as a function of tilt.

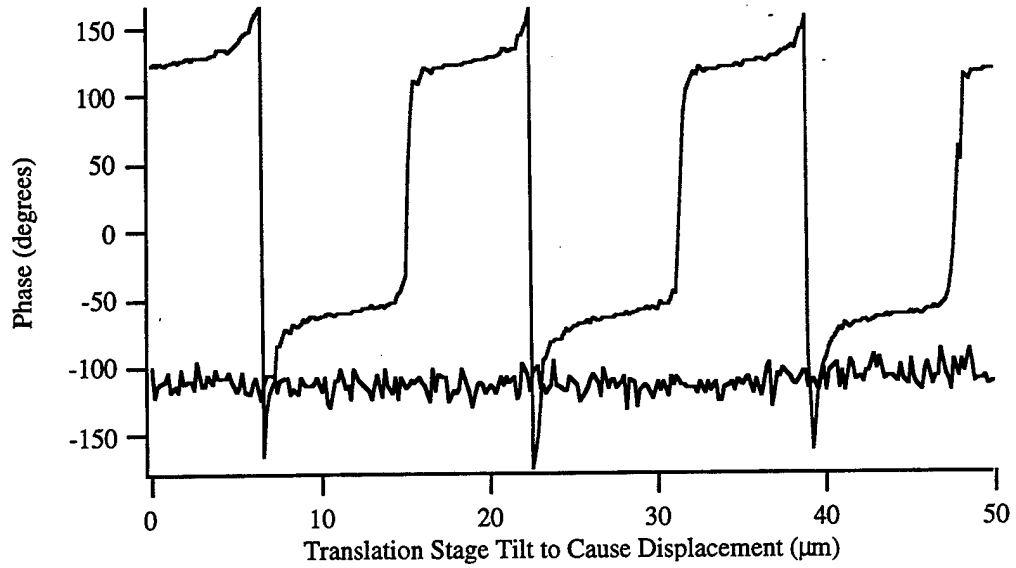

Figure 42. Phase of the interferometric signal as a function of tilt.

The uniformly decreasing amplitude of the interferometric peaks in Figure 41 is caused by the spot the heating beam hits shifting relative to the spot the probe

beam hits because the two beams are not incident on the specimen at the same angle.

The phase (Figure 42) varies by 180 degrees as the specimen is tilted from the positive to the negative slope of the interference curve. This is similar to the phase behavior of the interferometer when the specimen was excited using a piezo-electric transducer.

Since the magnitude and phase data demonstrate that the interferometer is operating as a classic Michelson interferometer, the displacement of the specimen surface due to thermal waves can be calculated. The maximum sensitivity of the interferometer was found to be 0.00245 V/nm. The maximum signal was 285 μV, which, upon dividing by the maximum sensitivity and a scaling factor for the lock-in amplifier, gives a maximum displacement of 116.1 pm. The Rosencwaig theory for thermal waves predicts a temperature rise of 101.5 °C which will generate a thermoelastic strain of 5.07×10^{-5} μm/m. Over a 200 nm specimen this strain will generate a displacement of 101.5 pm, which agrees quite well with the displacement measured interferometrically.

5.3.2 Aluminum

The piezoreflective signal for aluminum is typically 25% as high as the maximum interference signal, and the difference in height between successive peaks is typically 60% (Figure 43). By subtracting off the piezoreflective signal, these peaks can also be made to have the same height, the same as the data for

molybdenum. Since that has already been demonstrated, the response of the interferometer will be modelled instead.

The interferometer signal was modelled using a single complex amplitude for the piezoreflective signal, and a second complex number for the interferometric signal. For the piezoreflective signal, the magnitude and phase are simply the average value of the magnitude and phase for a tilt scan. The magnitude and phase of the interferometric signal are determined by vectorially subtracting the piezoreflective signal from the maximum value of the interferometric signal. The period of the interferometric signal (how many cycles occur across a tilt scan) was determined by the distance between the first and third minima. This was also used to set the period of the interferometer sensitivity curve (the middle plot in Figure 43). The interferometer signal was then modelled as a sensitivity times a complex interferometric signal, and added to the complex piezoreflective signal. The results show that both the magnitude and phase signals are accurately predicted.

The maximum displacement, 17.2 pm was calculated from the sensitivity of the interferometer, 0.00634 V/nm. Rosencwaig's theory predicts a temperature rise of 7.9 °C, which translates into a displacement of 36.5 pm over a 200 nm thick Al coating over AuPd. This is twice the displacement observed experimentally. This discrepancy is a result of the assumption that the substrate is a thermal insulator. For glass substrates this assumption is valid. Gold, however, is a very good conductor of heat, and can heat up almost as much as the aluminum coating.

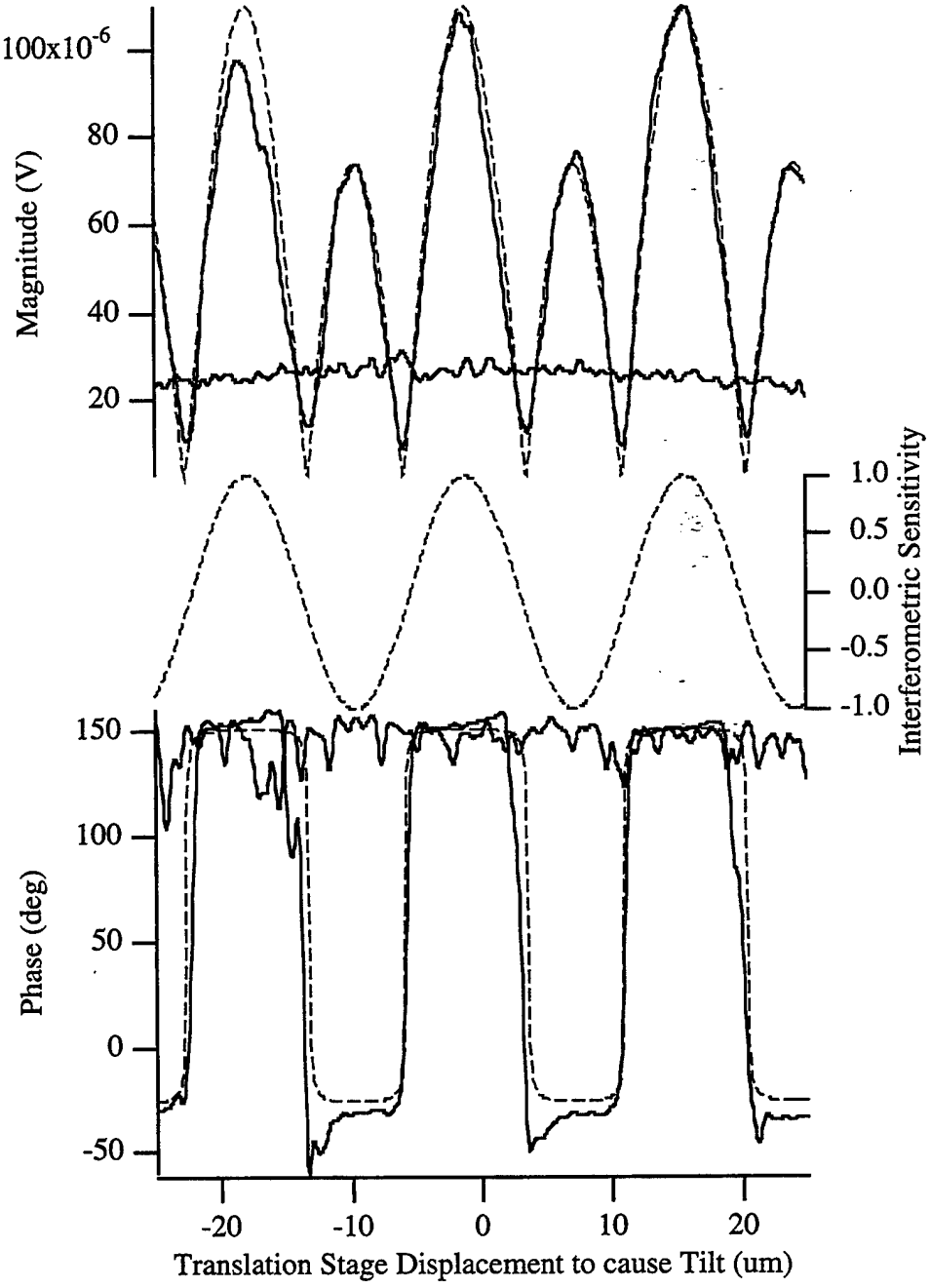

Figure 43. Tilt scan for an aluminum coating. The dashed lines are the modelled magnitude and phase.

5.4 Piezoreflective Detection of Ultrasound

5.4.1 Arsenic Telluride

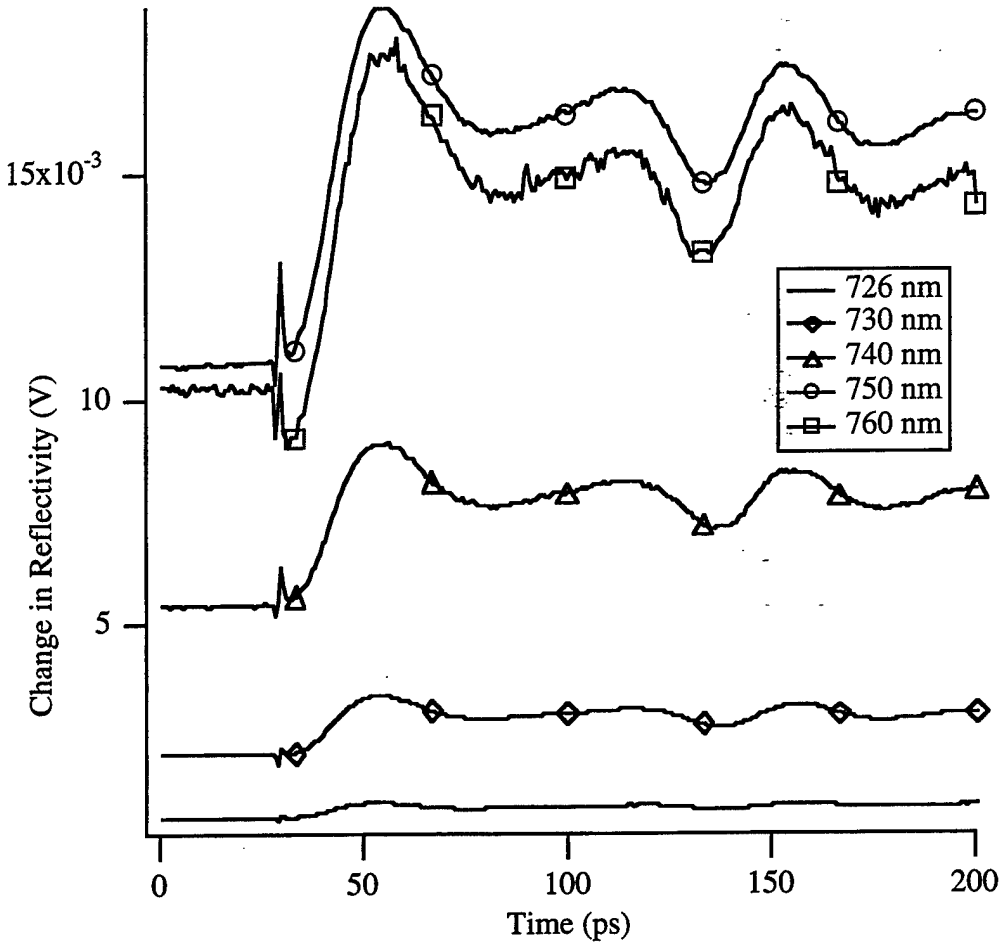

Figure 44. Piezoreflectivity of a 120 nm thick As_2Te_3 specimen.

The piezoreflective detection of ultrasound will be demonstrated to establish that the experiment is capable of reproducing the current state-of-the-art measurements. As_2Te_3 is a classic material to demonstrate piezoreflective detection

because ultrasonic echoes produce large reflectivity changes in it. The specimen, from Humphrey Maris and Guray Tas at Brown University, had a 120 nm thick layer of As_2Te_3 on a silicon substrate. The experiment was configured in the piezoreflective mode (with the reference beam blocked). Data were acquired at a number of wavelengths to determine whether the piezoreflectivity of As_2Te_3 is wavelength dependent.

The ultrasonic echoes are clearly visible in all but the shortest wavelength data in Figure 44. Notice that the ultrasonic echoes are bipolar, which is a result of the relatively low thermal conductivity of As_2Te_3.

The curves in Figure 44 replicate the published data for As_2Te_3 (Thomsen, 1986).

5.4.2 Aluminum

Initial experiments to detect ultrasonic echoes in aluminum coatings failed miserably. Upon further study, it was discovered that the acoustic impedances of aluminum and glass were so similar that only 14% of the ultrasonic energy incident on the interface was reflected back. To increase the reflected ultrasound, a layer of gold was placed between the aluminum and glass, which increased the amount of reflected ultrasound to 57%.

Scott Apt, of the Materials Laboratory Characterization Facility, produced specimens which had a 200 nm thick layer of aluminum evaporated on top a 300 nm thick layer of sputtered AuPd.

The ultrasonic echoes from this specimen are clearly visible in Figure 45.

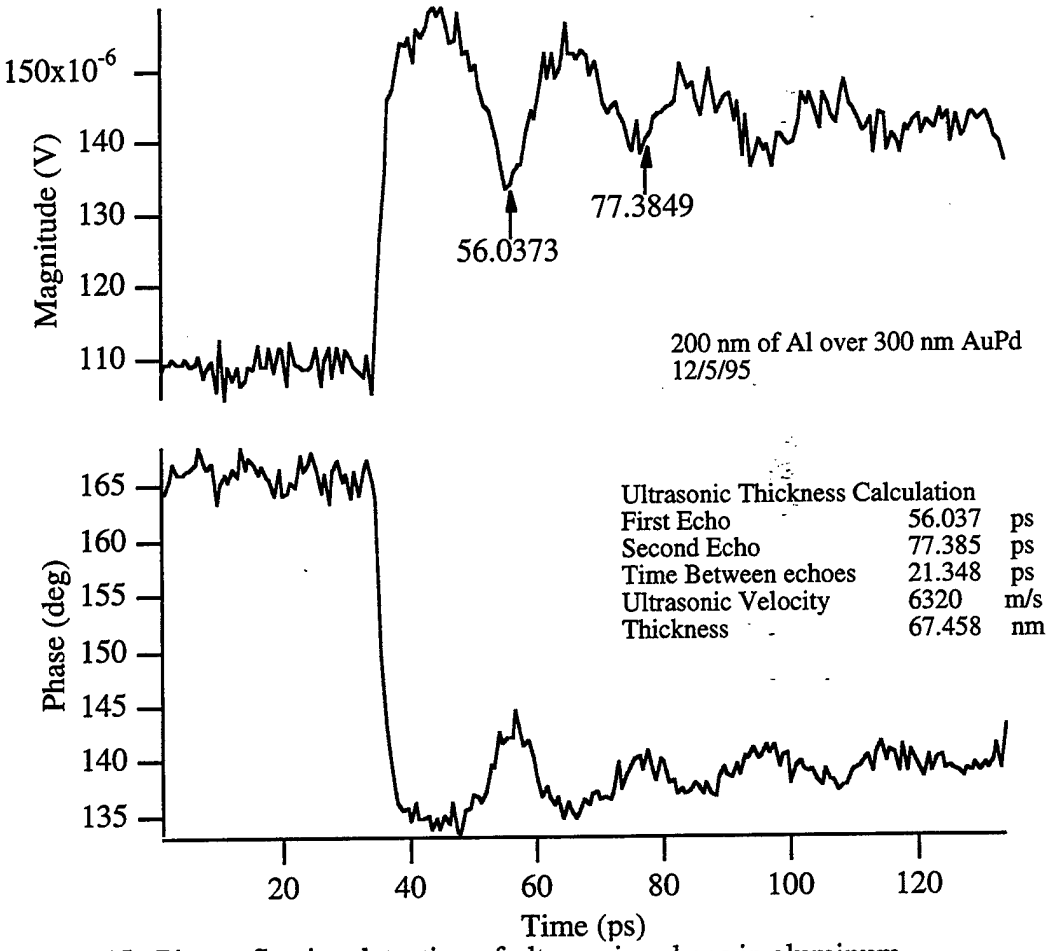

Figure 45. Piezoreflective detection of ultrasonic echoes in aluminum.

The phase data show the ultrasonic echoes with significantly less noise than the magnitude data. It is not currently understood why the ultrasonic echoes show up so well in the phase data, but it is suspected that this is due to the real and imaginary parts of the index of refraction varying differently as a function of strain.

Figure 45 shows a thickness of 70 nm for the aluminum coating. This is significantly thinner than the 200 nm nominal thickness of the coating. Until an independent measure of the film thickness is performed, it will be assumed that this error is due to a lack of process control on the evaporation process. Part of this discrepancy could be due to the fact that the properties of a thin coating (such as the ultrasonic velocity) are not the same as the properties for a bulk specimen of that material, but normally this effect only changes properties by a few percent.

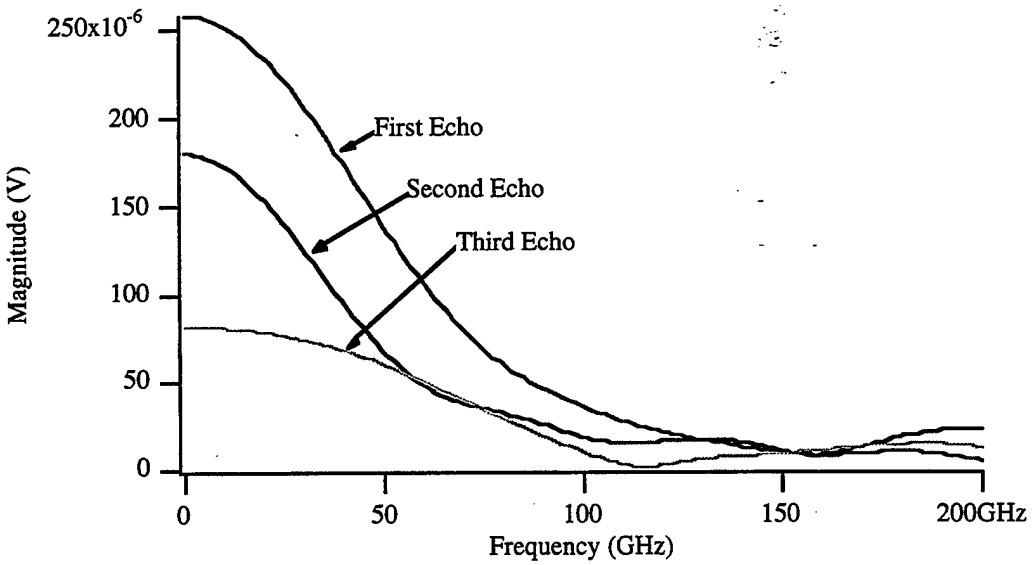

Figure 46. Frequency components of the ultrasonic echoes.

Ultrasonic attenuation measurements can be used to characterize the microstructure of materials. The higher the frequency of ultrasound, the smaller the microstructure that can be characterized. To determine how high a frequency the piezoreflective detection experiment can measure, the Fourier transform of the

first three ultrasonic echoes in Figure 45 were taken.

To take the Fourier transform, each echo was separated from the waveform, had the DC offset subtracted so that there would be no abrupt jump when the curve was padded with zeros to obtain 1024 points. The results, shown in Figure 46, demonstrate that experiment can generate and detect ultrasonic frequencies above 100 GHz, which corresponds to wavelengths of 63.2 nm and smaller.

5.5 Interferometric Detection of Ultrasound

5.5.1 Aluminum

The 200 nm of Al over 300 nm of AuPd specimen was used to test the interferometer first because it had produced well defined piezoreflective ultrasonic echoes. The beam block was removed from the reference beam to convert the experiment to interferometric detection. The interferometric fringe pattern was then measured by scanning the tilt of the specimen (Figure 47). The thermal wave experiments verified that the sensitivity of the interferometer was indeed proportional to the slope of the interference curve, and that the maximum sensitivity should occur at translation stage induced tilts of 16.0 μm, 23.9 μm and 32.5 μm. Furthermore, the sensitivity at 16.0 μm and 32.5 μm should be the negative of the sensitivity at 23.9 μm, which should show up in the phase data but not necessarily the magnitude data. The interferometer should not be sensitive to any displacements at 20.1 μm and 28.1 μm, because the slope is zero. To ensure that the inter-

ferometer was working correctly, data were taken at all nine angles shown in Figure 47, and piezoreflective data were taken. Because the experiment was automated, it was possible to acquire all ten scans automatically, and then repeat the process indefinitely. The plotting routines averaged all the scans at a particular angle together to increase the signal to noise ratio.

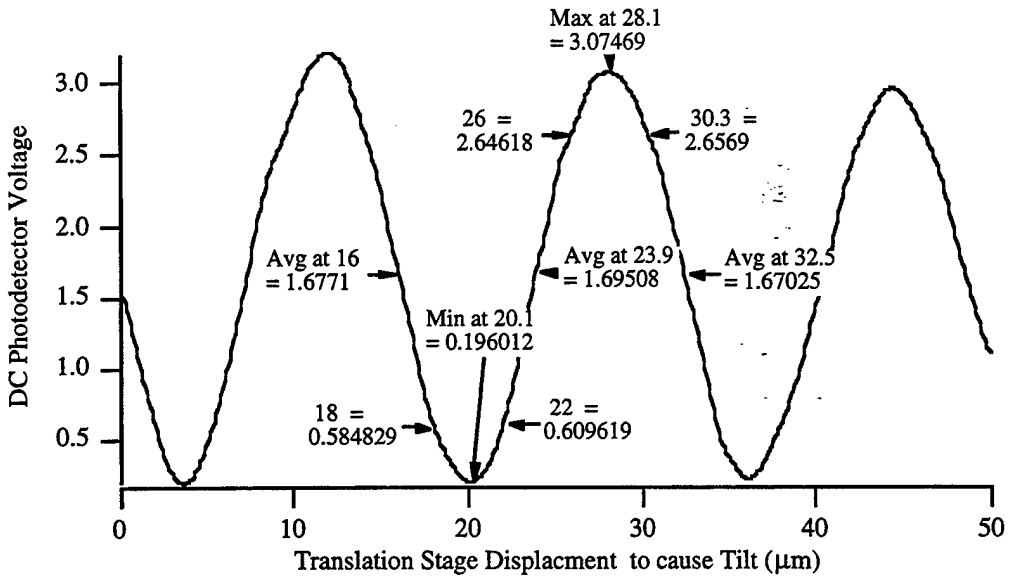

Figure 47. Fringe Scan for 200 nm of Al over 300 nm AuPd

The data for a translation stage displacement of 23.9 μm, maximum positive sensitivity, were plotted first. The curve, shown in Figure 48, has echoes in the same places as the piezoreflective data. Because the ultrasonic echoes are sharper in the interferometric data, it suggests that the interferometer may be better at picking up high frequencies than piezoreflective detection. The thickness of the aluminum layer was found from the ultrasonic echoes to be 67 nm.

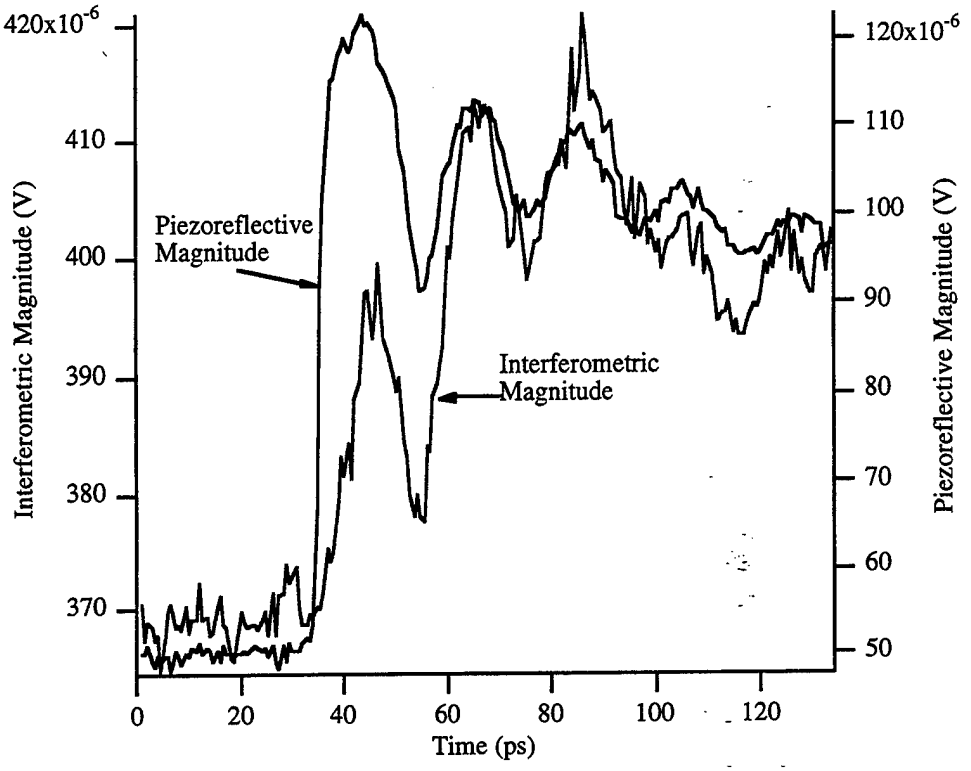

Figure 48. Interferometric vs. piezoreflective data, interferometer set for maximum positive signal.

To verify the interferometer performance, both sets of data from when the specimen was tilted to give the interferometer the maximum negative sensitivity was plotted with the piezoreflective scan in Figure 49. The echoes should look the same, but the phase should flip. Instead, the echoes vanished.

To determine the reason why the echoes vanished, all ten sets of magnitude data were plotted in Figure 50, and corresponding sets of phase data were plotted in Figure 51. In all of the figures in this dissertation where all ten plots are shown on the same graph, the very first plot, as listed in the legend, (c_0 in Figure 50, for

example) is the piezoreflective data. The other nine curves correspond to the nine tilt angles shown on the fringe scan (Figure 48), in the order of increasing tilt. The second curve, labeled with asterisks, would correspond to a translation stage displacement of 16 μm for a maximum negative slope. The fourth curve, labeled with triangles, corresponds to a translation stage displacement of 20.1 μm, and the interferometer set for maximum destructive interference, for example.

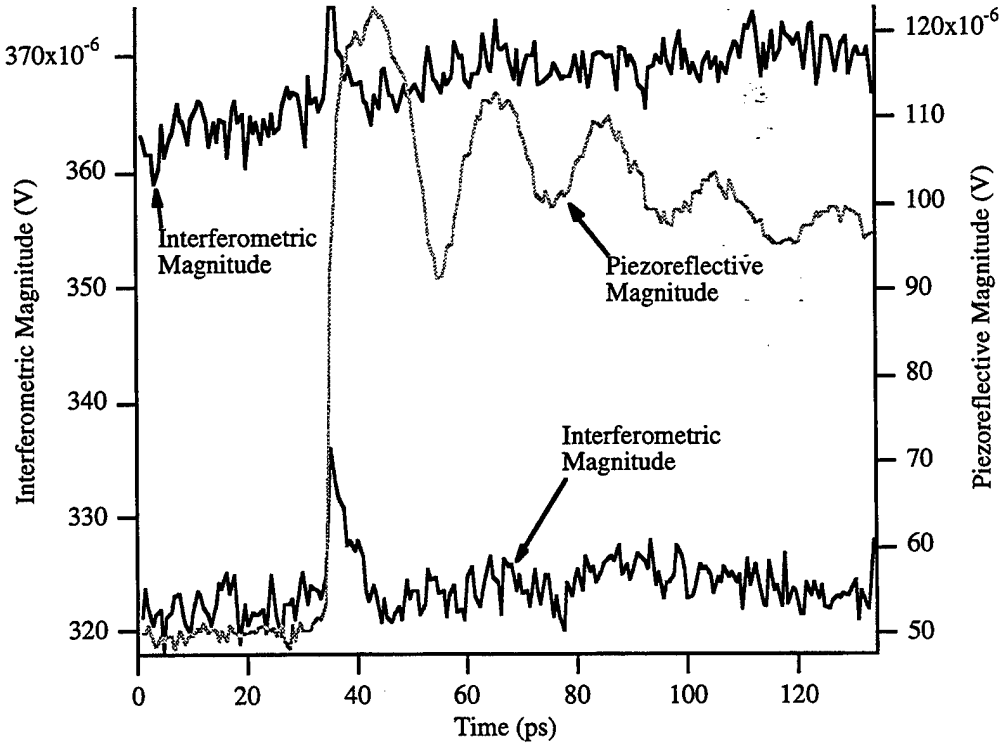

Figure 49. Interferometric vs. piezoreflective data, interferometer set for maximum negative signal.

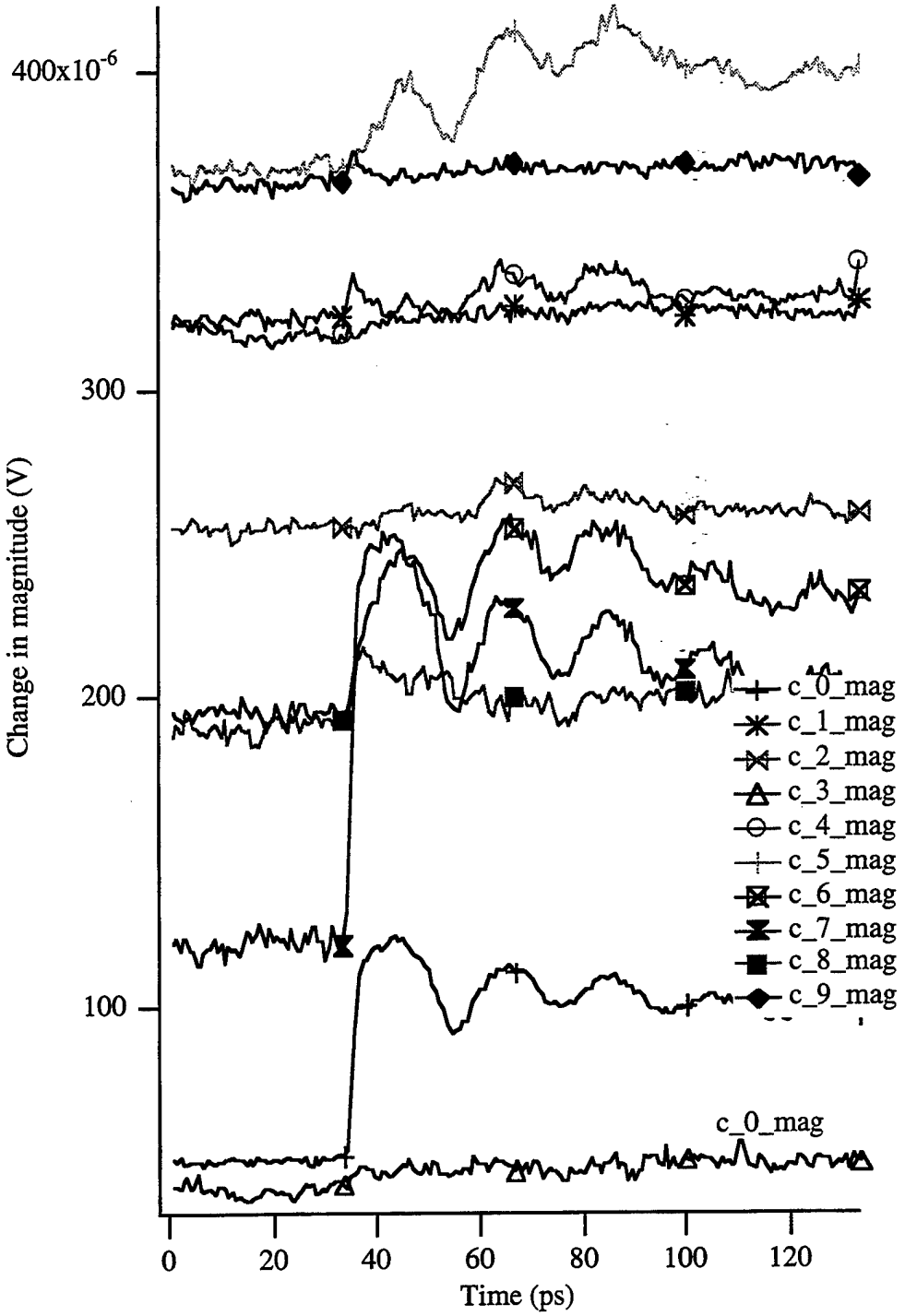

Figure 50. Magnitude of the interference signals for 200 nm of Al.

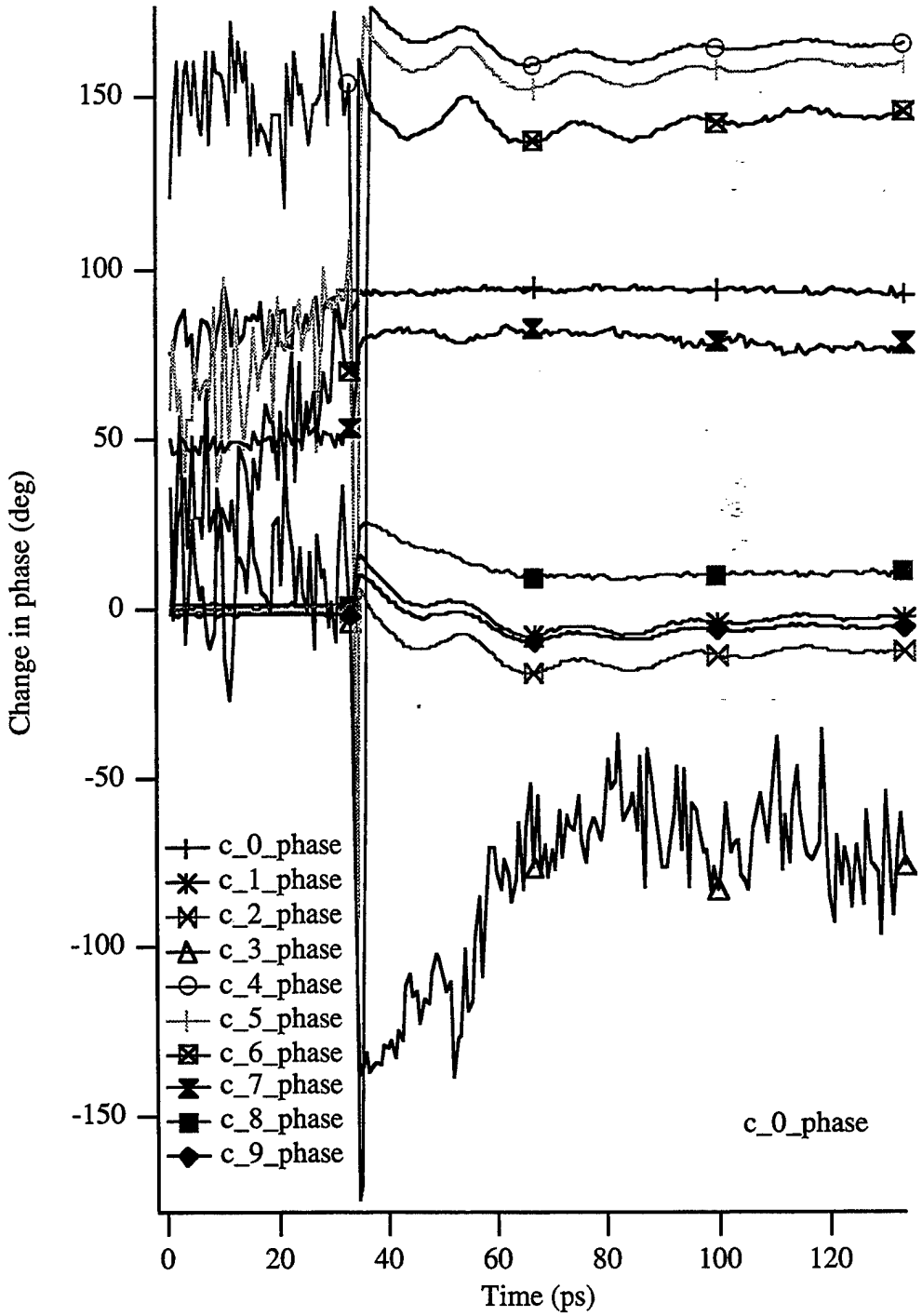

Figure 51. Interference scan phases for 200 nm of Al over AuPd, 10 angles.

According to the interferometer theory, the c_1, c_5 and c_9 curves should show the greatest interferometric sensitivity. These three curves do show the greatest sensitivity to the thermal wave signal (the portion of the curve before the heating pulse hits). The c_1 and c_9 curves are not, however, sensitive to the displacements caused by the ultrasonic echoes. Instead the c_6 and c_7 curves show the best sensitivity, and the c_4 and c_5 curves show some sensitivity. Curves c_4, c_5 and c_6 all occur when the interference curve has a positive slope. Curve c_7 occurs when the interferometer has no slope at all, and rather than showing no echoes like it should, it shows the best echoes.

This interferometer behavior is definitely anomalous. When the interferometer shows the best sensitivity to thermal wave displacements it should also show the best sensitivity to ultrasonic displacements. Moreover, when the interferometer is shifted from the maximum positive sensitivity to the maximum negative sensitivity, the ultrasonic echoes should still appear. Their disappearance suggests that the interferometric and piezoreflective effects have different phases, and can add together constructively when in phase, and can cancel each other when out of phase. To test this hypothesis, a specimen which exhibits neither piezoreflectance nor thermoreflectance is required. The displacement of the surface will then be the principal effect measured.

5.5.2 Gold

Gold is an ideal material to test the interferometer because it has a piezoreflective signal which is 15 times smaller than the interferometric signal. A specimen with a 30 nm layer of gold over a 500 nm layer of SiO_2 on top of silicon was obtained from Humphrey Maris and Chris Morath at Brown University.

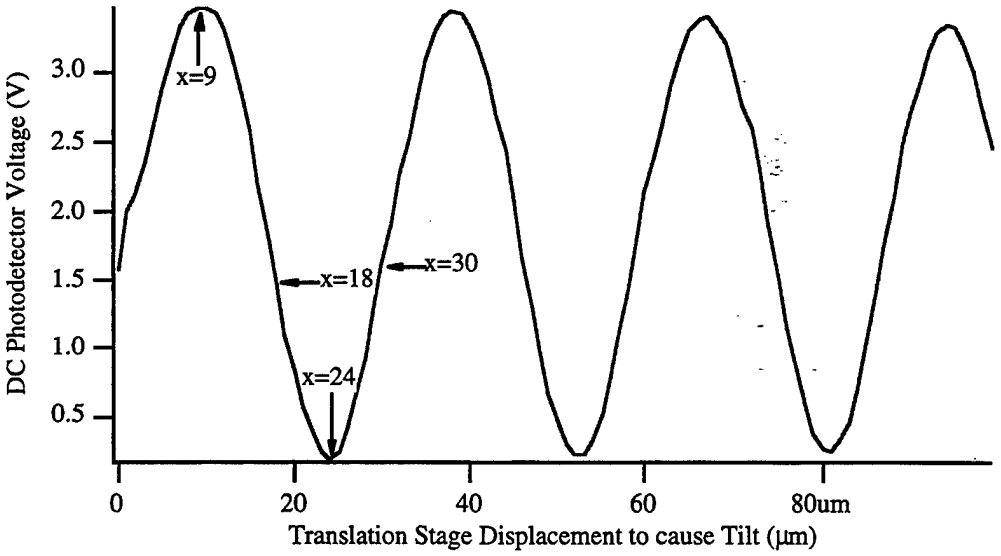

Figure 52. Fringe scan for 30 nm gold coating.

The difference between interferometric and piezoreflective detection is obvious in Figure 53. Both curves show a strong spike in the signal when the heating beam hits, but only the interferometric data show ultrasonic echoes. If the scale of the piezoreflective data is enlarged, it is possible to see a single echo (Figure 54).

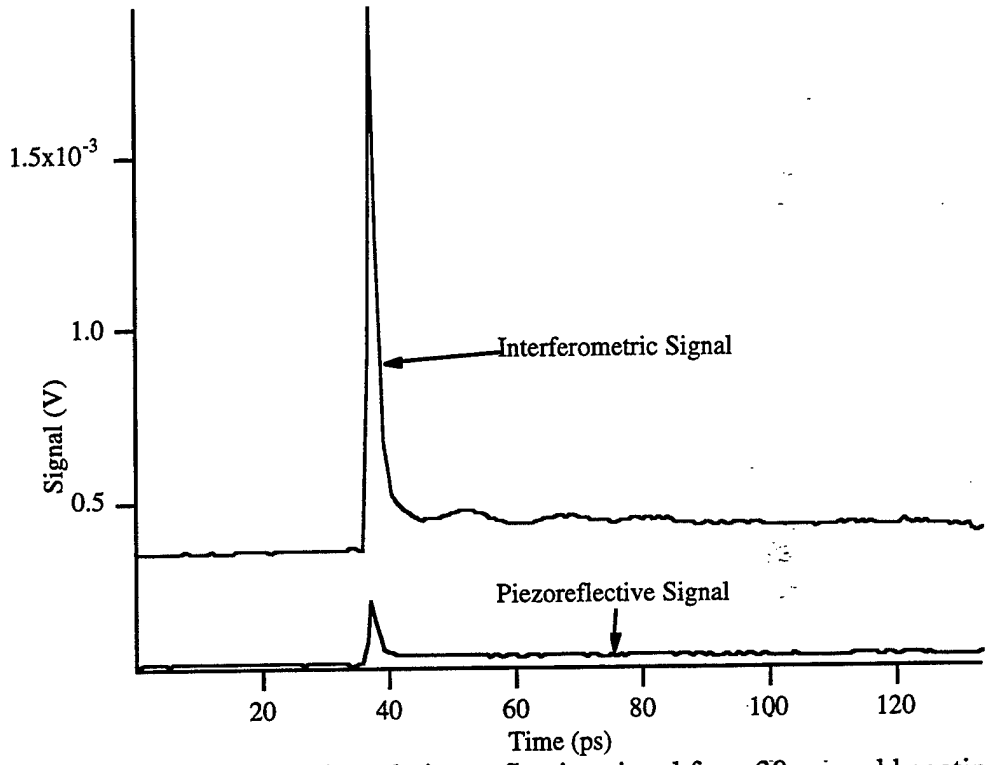

Figure 53. Interferometric and piezoreflective signal for a 30 nm gold coating

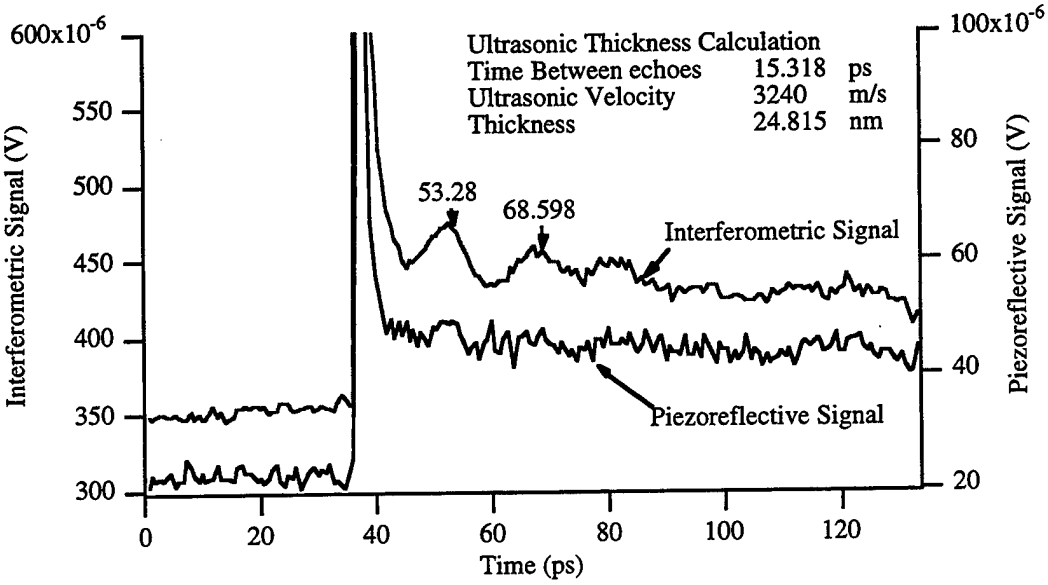

Figure 54. Interferometric vs. piezoreflective echoes - enlarged scale.

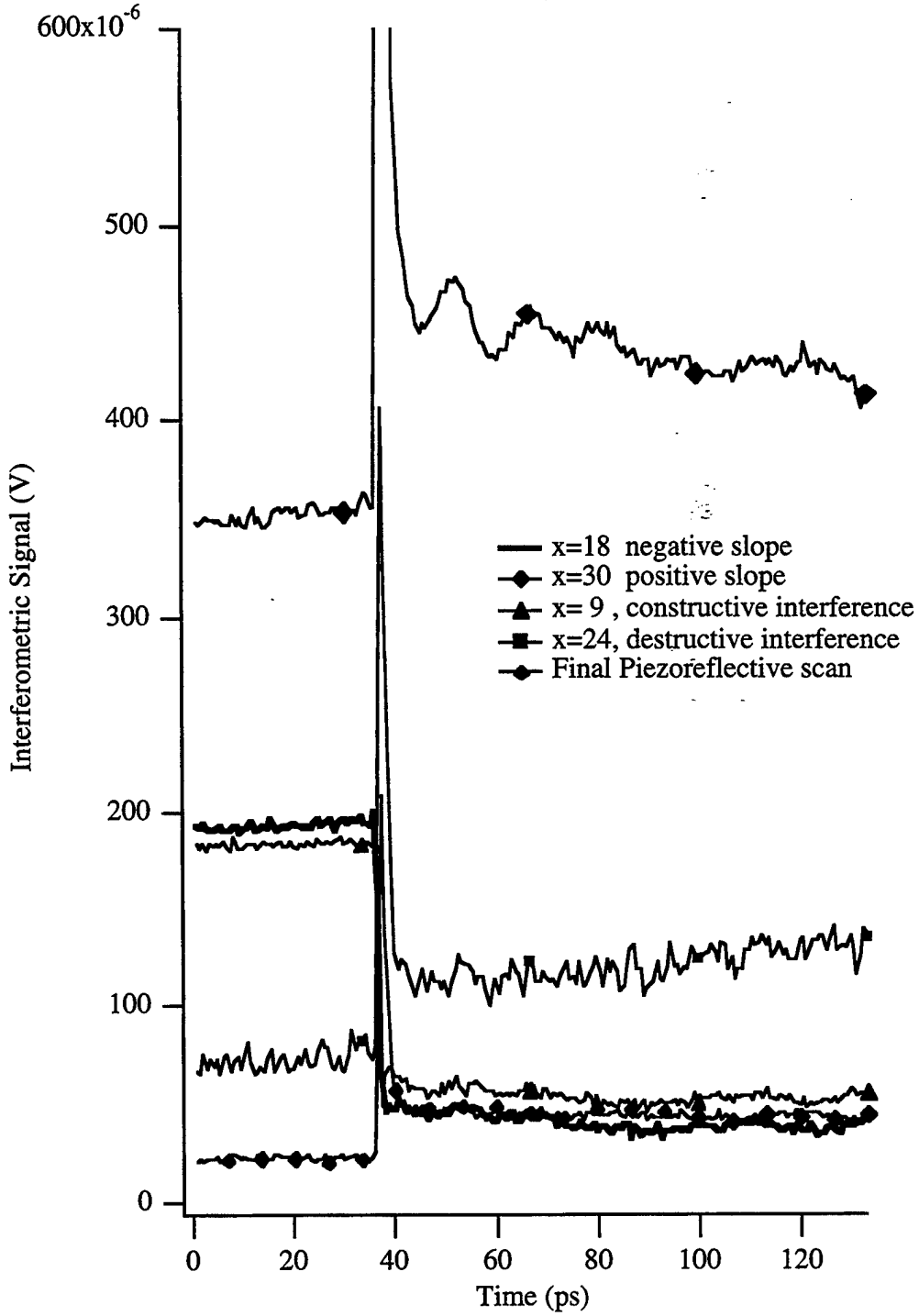

Figure 55. Magnitude data for the gold specimen.

Note that this is only a small echo, with a signal to noise ratio close to unity, and if the specimen had been thicker, not even that echo would have been visible. These two plots show that, for at least one material, interferometric detection is more sensitive than piezoreflective detection.

All the interferometric and piezoreflective data for the gold specimen are shown in Figure 55, and the ultrasonic echoes are clearly visible in the curve with the positive slope. It looks like there is an echo in the destructive interference curve, but it is not much larger than the noise. What is interesting is the way that the negative slope and destructive interference curves decrease in magnitude by approximately the same amount that the positive slope data increases in amplitude after the heating pulse hits. This is the behavior which was predicted for the interferometer. Unfortunately the ultrasonic echoes, which should also be inverted, do not appear. This is probably due to a weak piezoreflective effect canceling a weak interferometric effect.

The quality of an interferometer is determined by it's ability to detect a given displacement for a given frequency range. To determine the frequency response of the interferometer for this gold specimen, the Fourier transform of the ultrasonic echoes was taken (Figure 56). The displacement of the specimen is determined from the sensitivity of the interferometer. For this arrangement, the sensitivity was found to be 0.00580 V/nm. The first ultrasonic echo showed a change in voltage of 40 μV, and the second showed a change of 23 μV. The dis-

placement corresponding to a voltage change of 23 μV is 4.0 pm. This interferometer has a sensitivity of 4 pm for signals up to 100 GHz in frequency. For comparison, the properties of two reference beam interferometers are compared to the delay line based pulsed interferometer (Scruby, 1990).

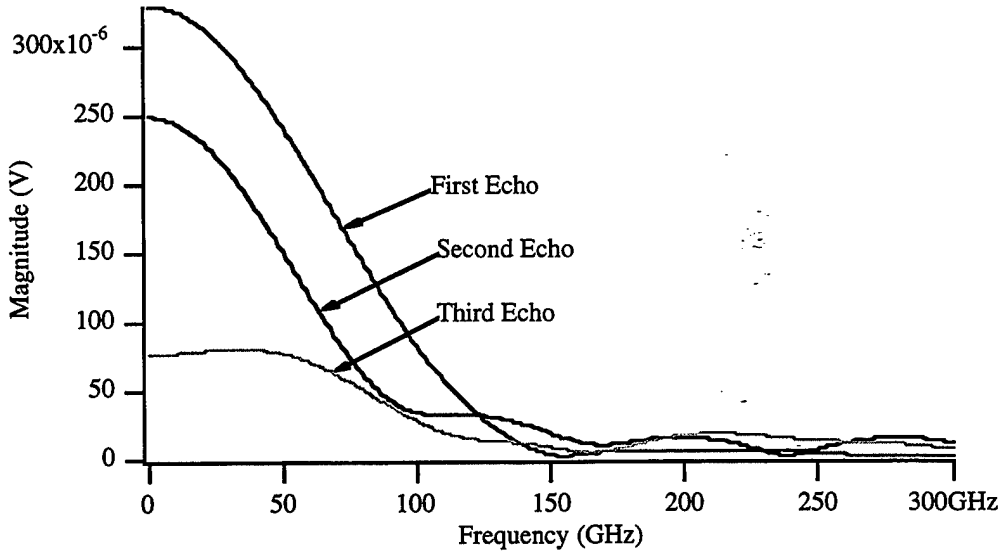

Figure 56. Fourier transform of the ultrasonic echoes detected interferometrically from a 50 nm layer of gold.

Table 6. Interferometer Frequency Range and Sensitivities.

Interferometer	Frequency Range MHz	Sensitivity pm
2 mW He-Ne RBI	10	3
1 W Argon Ion RBI	10	15
UF Pulsed Interferometer	100,000	4

The ultrafast interferometer has the same sensitivity as conventional interferometer, and a frequency range that is 10,000 times larger. The actual bandwidth of the pulsed interferometer is only 1 Hz, but the delay line technique gives the interferometer a frequency response (or effective bandwidth) of greater than 100 GHz.

5.5.3 Gold Palladium

Gold Palladium is also weakly piezoreflective, and specimens are readily available. AuPd is used to coat nonconductive specimens for examination under the scanning electron microscope.

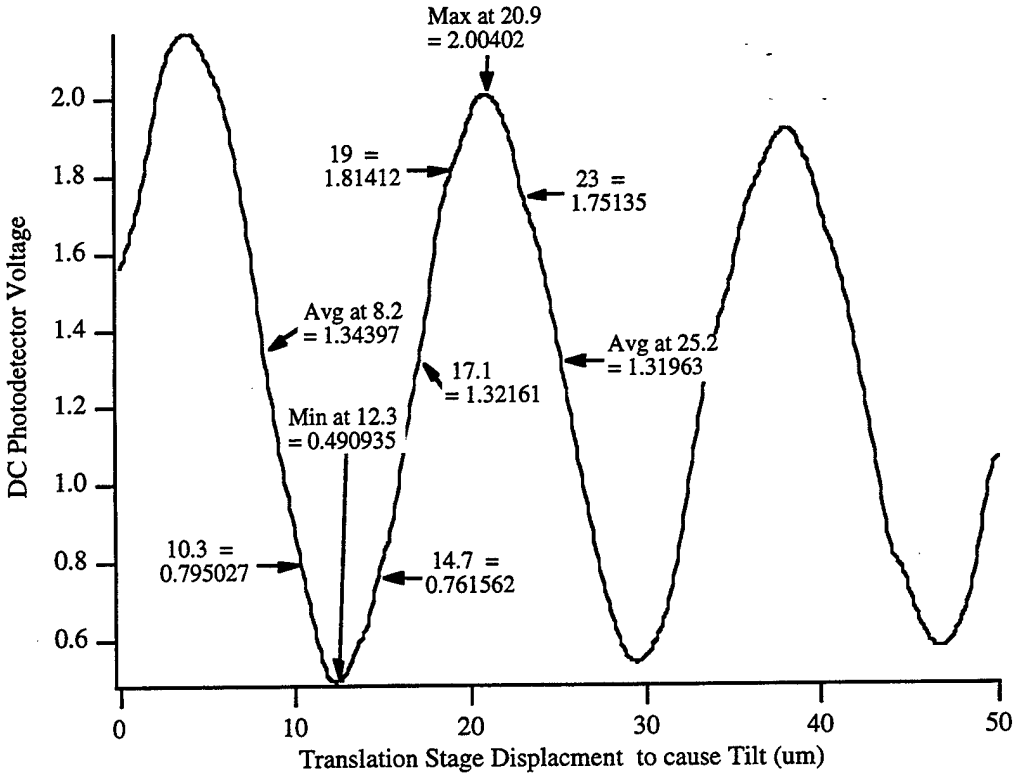

Figure 57. Fringe Scan for gold-palladium.

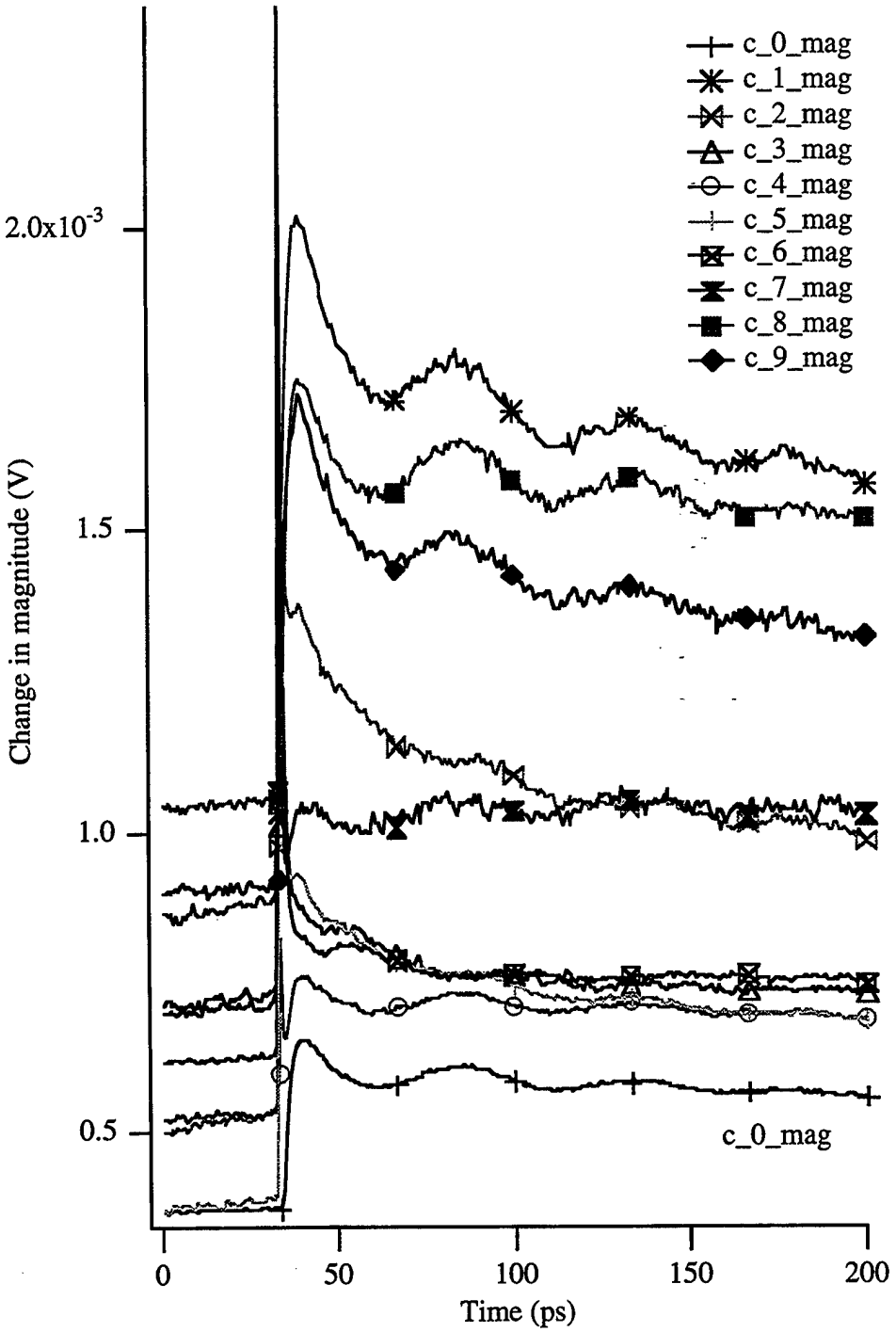

Figure 58. Magnitude data from 100 nm thick AuPd.

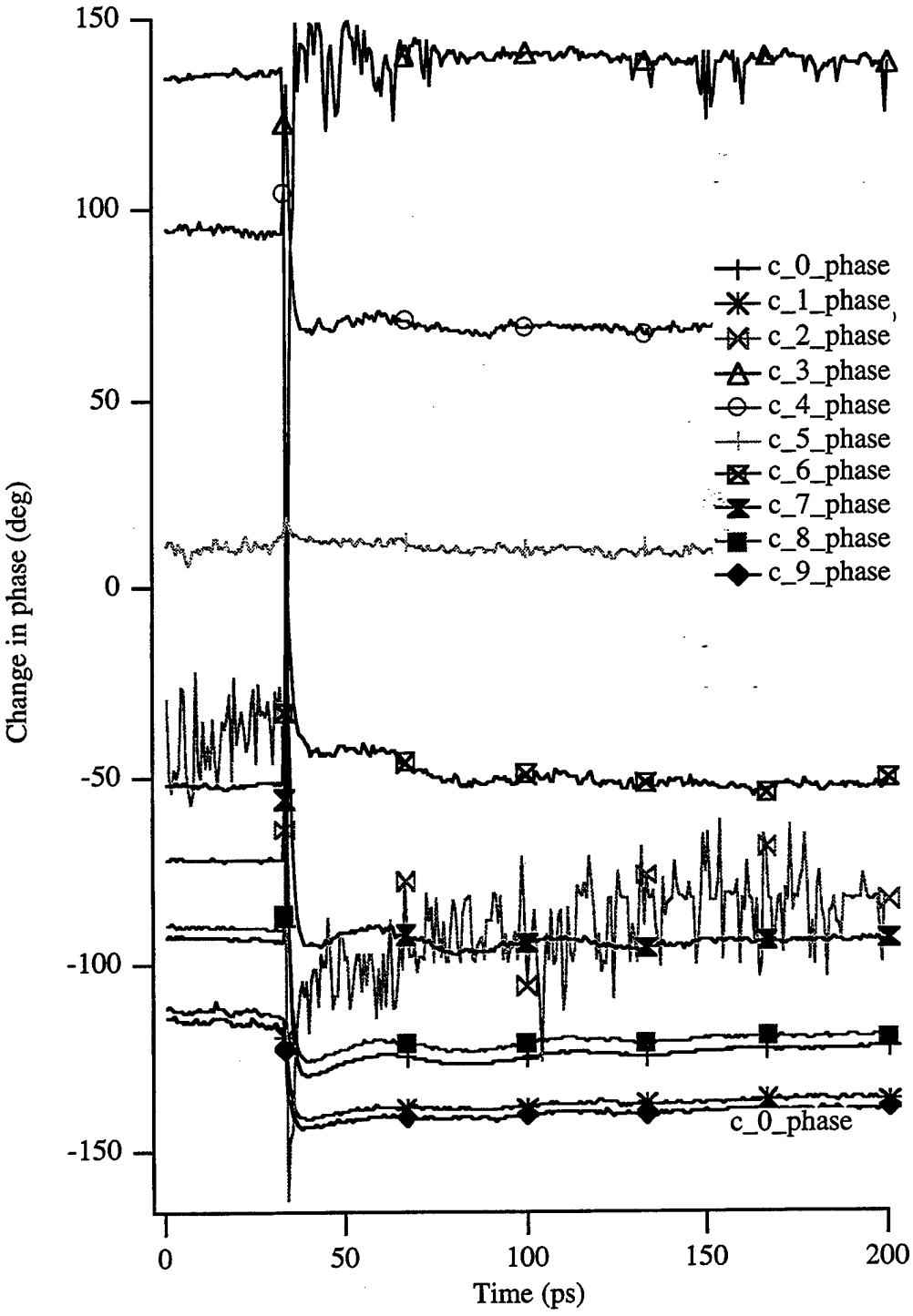

Figure 59. Phase data from 100 nm of AuPd

Scott Apt, of the Materials Lab Characterization Facility, prepared a number of specimens ranging in thickness from 100 to 600 nm. The following data were taken on a specimen with a 100 nm layer of AuPd on glass. The fringe scan is shown in Figure 57, the magnitude data in Figure 58, and the phase data in Figure 59.

The ultrasonic echoes are more visible in the piezoreflective data for AuPd than they are for the pure gold, but the interferometric signals still show about three times as much modulation as the piezoreflective signal. Signals c_1, c_8, and c_9 show the most amplitude modulation, and c_4 and the piezoreflective signal c_0 show about half as much modulation. Signals c_1, c_9 and c_8 occur when the interference curve has a negative slope, but signal c_2 shows a thermoreflectance drop, but virtually no ultrasonic modulation. Moreover, signal c_4 was acquired while the interferometer was set to a positive slope. The phase data for c_1, c_9, c_8, and c_0 (the piezoreflective scan) all show modulation due to the ultrasound, and have phases in the -140 degree range. While it is tempting to draw a conclusion from this, signal c_4 behaves completely differently. It has a phase of 70 degrees (or 180 degrees out of phase with the other signals) and also shows modulation due to the ultrasonic echoes. Unfortunately there is not enough data to draw a conclusion about how to maximize the ultrasonic signal. A model which predicts the signal of the interferometer as a function of tilt angle needs to be developed.

The calculation of the thickness of the specimen is shown in Figure 60, and the three measurements of the thickness agree to within 6%. The sensitivity of the interferometer was 0.00432 V/nm, and the amplitude of the first ultrasonic reflection was 900 μV which corresponds to a displacement of 2.1 nm. Unfortunately the optical, thermal and elastic constants are not available for AuPd, so that displacements cannot be compared to the models.

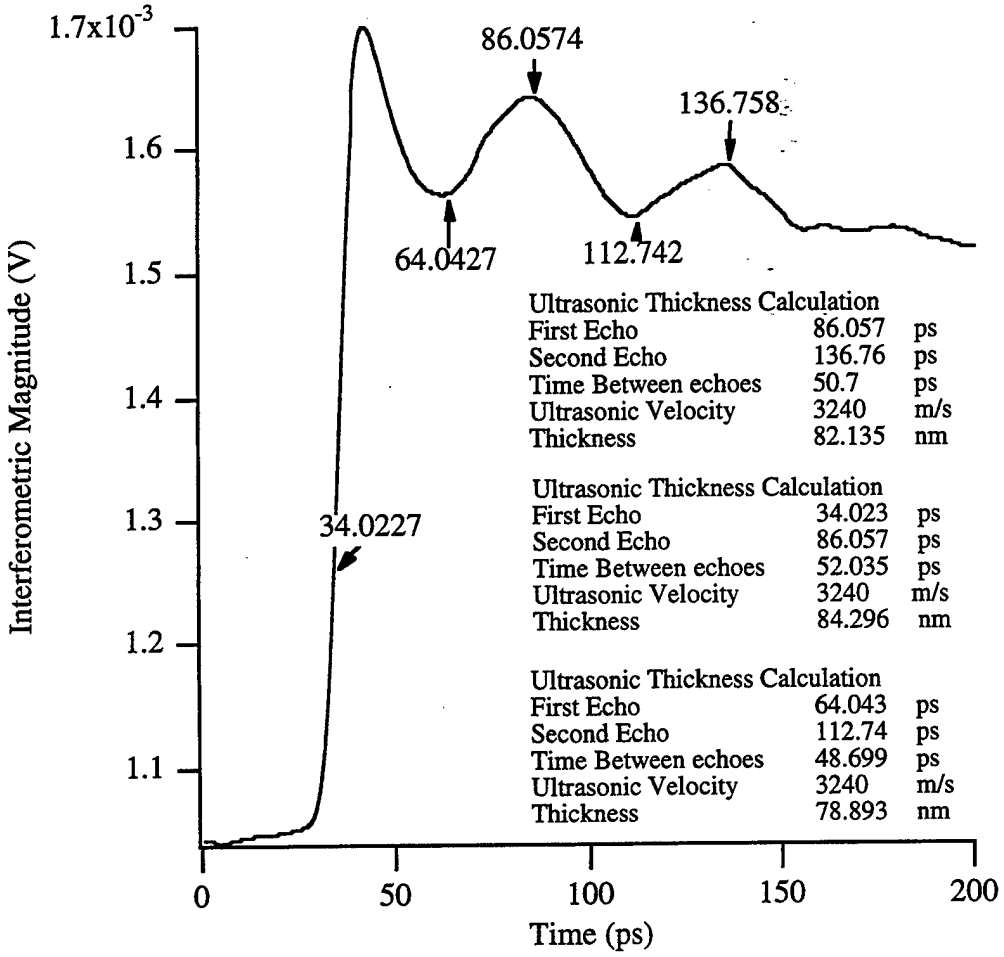

Figure 60. Thickness calculation for AuPd.

5.5.4 Molybdenum

Molybdenum was demonstrated to have a low piezoreflectivity (see Section 5.3.1), and will therefore be useful to test the interferometer. The specimen consisted of a 200 nm thick layer of molybdenum over glass, and was produced by Peter Shull at Johns Hopkins University. The magnitude data are shown in Figure 61 and the phase data in Figure 62.

The data are interesting, because the size of the step caused by the heating of the surface of the specimen is proportional to thermal wave signal (the height of the curve before the heating beam hits). This suggests that the value of the thermal wave signal in Figure 61 is proportional to the sensitivity of the interferometer for a given tilt angle of the specimen, and that this same sensitivity can then be used to calculate the height of the step caused by the absorption of the heating pulse.

A second feature to note is the flatness of the curves after the heating pulse is absorbed. Using a one dimensional heat propagation model in an infinite half space, once a heating pulse is absorbed by the film the displacement of the surface of the film should remain constant due to conservation of energy. This would be seen experimentally as a step increase in the displacement of the surface of the specimen, followed by no decrease in the signal. This is exactly what happens in Figure 61.

The thickness of the specimen, as measured from the interferometric data f1_mag, was 170 nm.

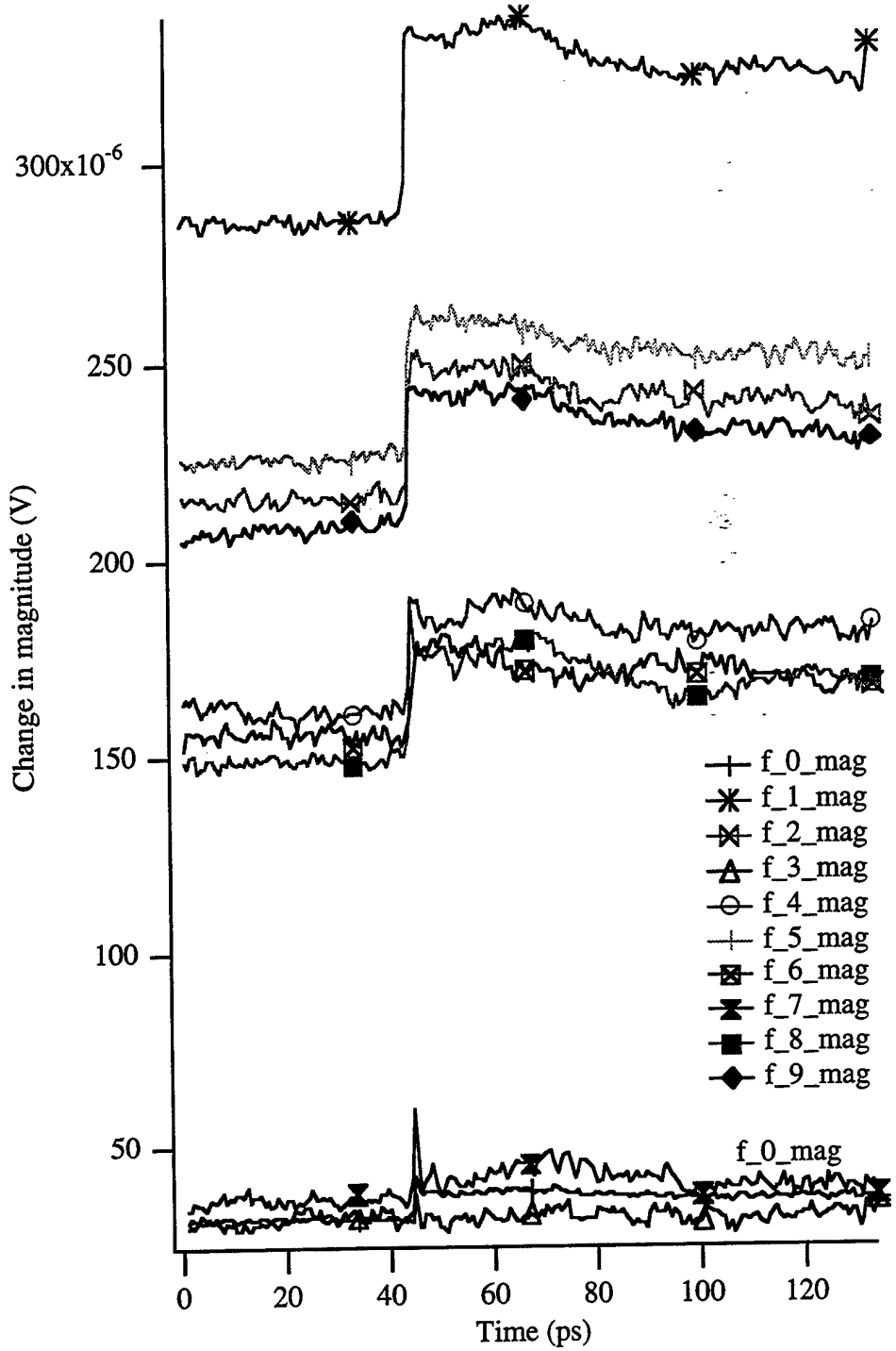

Figure 61. Magnitude data for molybdenum.

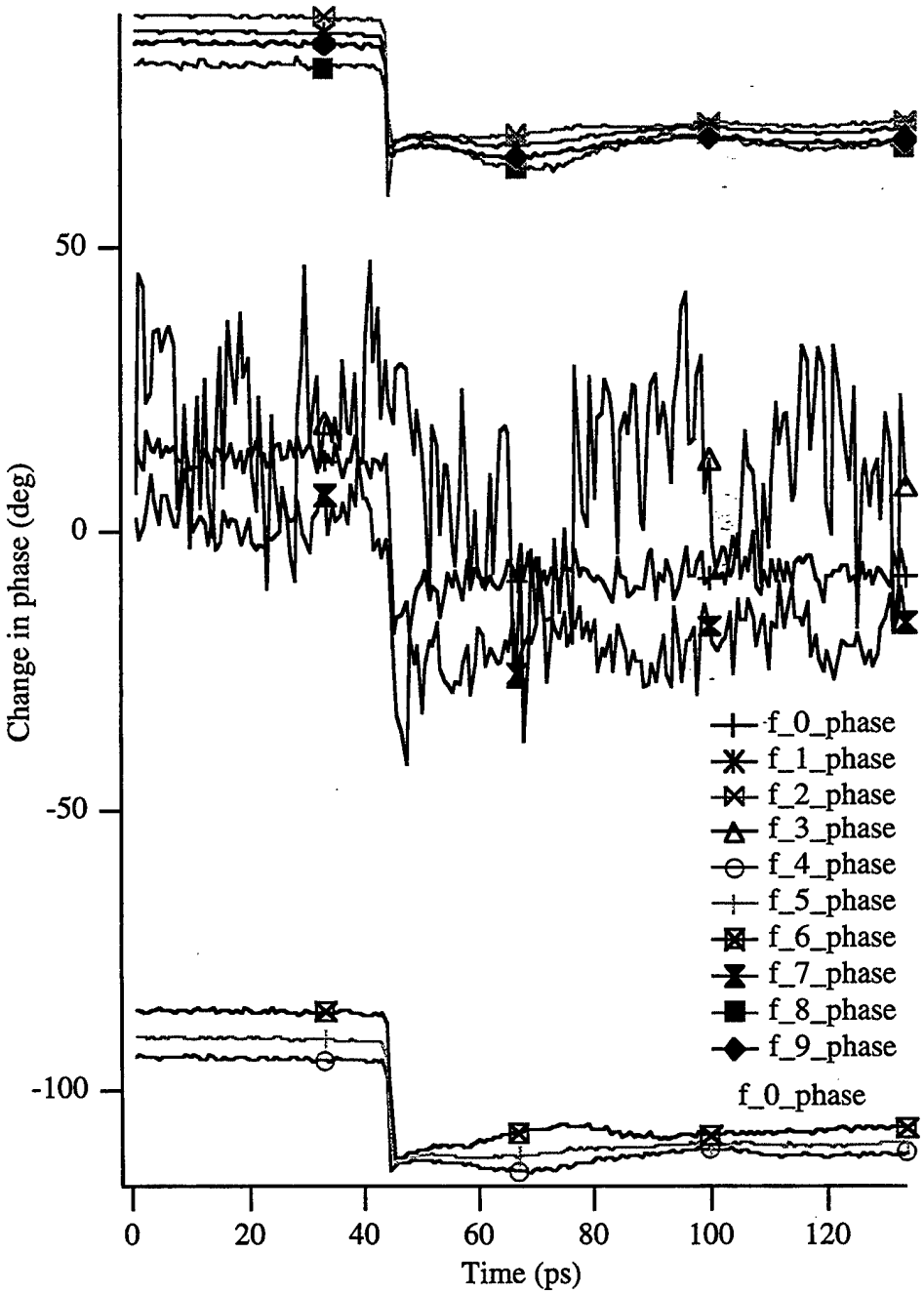

Figure 62. Phase data for Molybdenum.

The actual displacements of the specimen surface can be compared to the models developed in Chapter 4. The sensitivity of the interferometer was found to be 0.00580 V/nm. The interferometric signal due to thermal waves was 285 μV, which corresponds to a displacement of 49.1 pm. The Rosencwaig model predicts a temperature rise at the surface of the specimen of 50.7 °C, and a displacement of 50.7 pm (the reason the digits are the same is because when the thermal expansion coefficient of $5x10^{-6}$ is multiplied by the thickness of 200 nm a conversion factor of 1 pm/°C results for this special case). This is only a 3% difference, which is remarkably close considering all the likely errors in the material properties data.

The displacement due to the absorption of the ultrafast pulse can be compared to the displacement predicted by Maris's model. The interferometric signal immediately after the heating pulse hits is 331 μV, which corresponds to a displacement of 57.1 pm. The displacement due to the heating pulse alone is 7.9 pm. The displacement of the surface is calculated by integrating the exponentially decaying temperature profile predicted by Maris's model, and then multiplying the result by the thermal expansion coefficient. The displacement is predicted to be 7.0 pm, which is very close to the 7.9 pm which was observed experimentally.

The predicted displacement due to the ultrasonic wave is 3 times larger than the actual displacement. A displacement of 6 pm was predicted in Section 4.6. The actual displacement, as measured from the peak of f_0_mag at 65 ps to the valley at 100 ps is only 2.4 pm. This discrepancy is probably a result of

absorption of the ultrasound by the molybdenum. Further tests on specimens with a range of thicknesses are required to conclusively identify the source of this discrepancy.

5.6 Comparison of the Model to the Piezoreflective Data

A model, which was developed in Chapter 4, which describes the generation, propagation, and detection of ultrasound was used to simulate the piezoreflective data from a gold-palladium specimen. The specimen consisted of a 70 nm layer of aluminum over 300 nm of AuPd. To reduce the noise, the data were smoothed with a 25 point binomial (Gaussian) algorithm. Because the thermoreflectance coefficient and piezoreflectance coefficients were not known, they were be left as adjustable parameters. The two effects were combined using superposition (adding them together). The results of the model are shown in Figure 63. The surface temperature as a function of time is shown in the top curve, the displacement of the surface as a function of time is shown in the second curve, and the combined curves and the experimental data are shown in the bottom plot. The thermoreflectance coefficient was 5.0×10^7 volts of change at the photodetector per °C, and displacement was scaled using a piezoreflective constant of -100,000 volts per unit strain. The model agrees quite well with the experimental data. In fact, with some smoothing to take into account finite length of the probe beam, the model would agree even better. It is important to keep in mind, however, that the

model uses many simplistic assumptions, and ignores important effects such as ultrasonic attenuation due to the material. The model is, however, still very useful in helping to sort out the different physical effects and their influence on the experimental results.

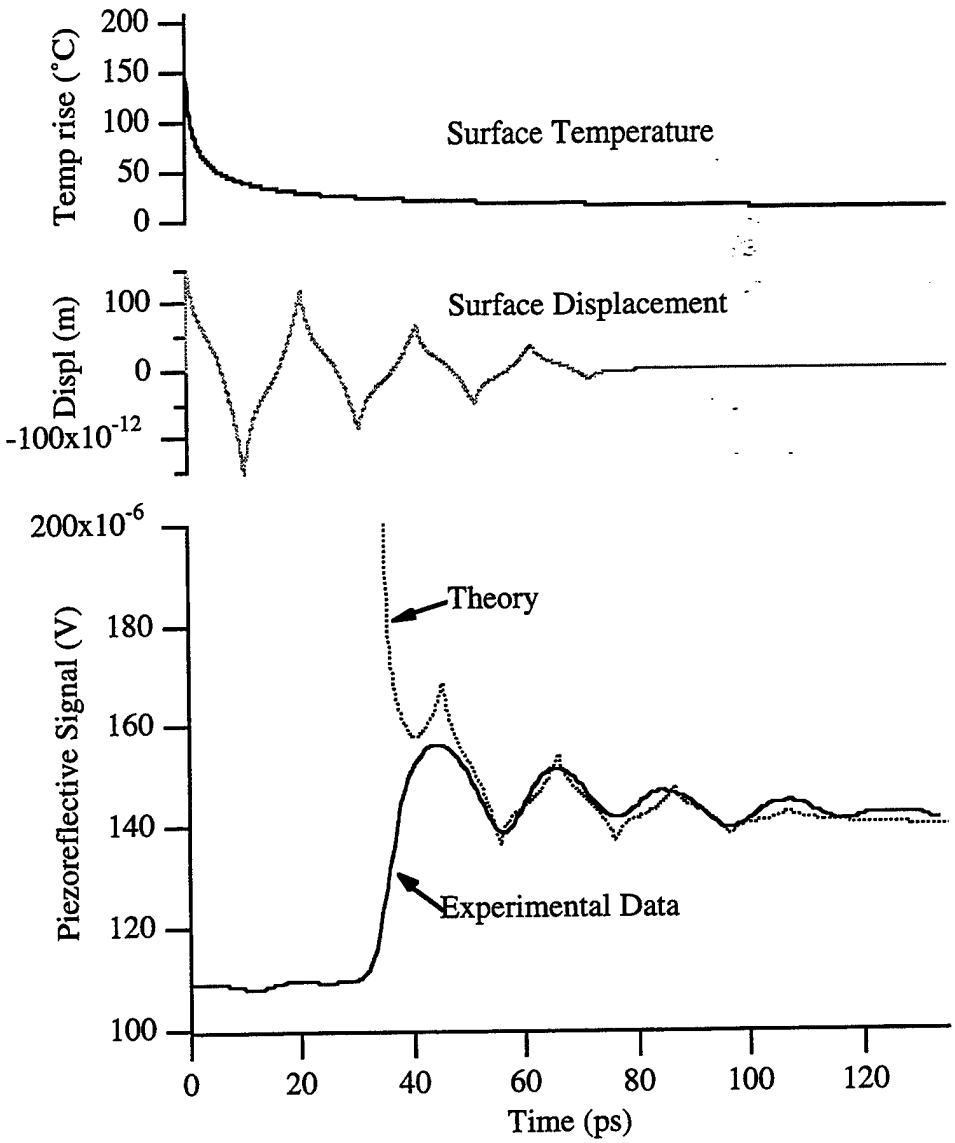

Figure 63. Theory vs. experiment for the 70 nm thick Al over AuPd.

6. CONCLUSIONS

6.1 Nondestructive Inspection Technique for Thin Coatings

The objective of this effort was to develop a nondestructive inspection technique to measure the thickness of thin films. The inspection technique, laser generated high frequency ultrasound with pulsed interferometric detection, has achieved this objective. Experimental results demonstrate that this technique measured the thickness of a 67 nm thick aluminum coating, a 25 nm thick gold coating, an 80 nm gold-palladium coating, and a 170 nm thick molybdenum coating.

A comparison of these results with the data from piezoreflective experiments demonstrated that this interferometric technique is indeed detecting the ultrasonic echoes. Moreover, the piezoreflective data from the 30 nm thick gold coating shows that one ultrasonic echo is only very weakly visible, and would disappear into the noise if the coating were thicker. The interferometric data, however, clearly shows three distinct echoes. In practice, to inspect gold coatings piezoreflectively, they would have to be coated with an aluminum transducer layer, which would render the technique destructive. For materials which are not piezoreflective, interferometrically detected ultrasound is the optimal method for nondestructively measuring the thickness or elastic properties of the coating.

6.2 The Interferometer

The delay line based pulsed interferometer has the same sensitivity as a

conventional interferometer, and a frequency range which is four orders of magnitude higher. Experiments using a piezoelectric transducer to generate ultrasound demonstrated that the light in ultrafast pulses from a Ti:sapphire laser was coherent enough to perform interferometry. These results also show that the sensitivity of the interferometer to small displacements is proportional to the slope of the interference curve, which demonstrates that the interferometer is operating in the same mode as a conventional Michelson interferometer. The frequency range of the interferometer was measured by transforming the ultrasonic echoes from a 30 nm thick gold coating into the frequency domain. Frequencies up to 100 GHz were observed for this displacements as small as 4 pm. Conventional shot noise limited interferometers have a frequency range of only 10 MHz for this sensitivity (Scruby, 1990).

6.3 Modelling

Models were developed which predicted the results of the inspection process with varying degrees of success. The thermal wave model predicted the displacement of the surface of the specimen due to thermal waves to within 3% for molybdenum. The model for the absorption of the laser pulse predicted a displacement of the surface of the molybdenum specimen to be 7.0 pm, which is within 12% of the 7.9 pm which was observed experimentally. The model for the piezoreflective detection of ultrasound predicted the qualitative shape of the signal.

6.4 Directions for Future Work

This thesis has demonstrated the feasibility of interferometrically detecting high frequency ultrasound, but there are still many questions which must be answered before this technique can be optimized for production inspections.

To develop this technique, a better understanding of the inspection process is required. A model which describes the interaction of the thermoreflective, piezoreflective and interferometric signals is necessary to optimize the detection of ultrasonic echoes. A complete understanding of the phase signal is required to compare its sensitivity to that of the magnitude signal. A comprehensive model is also required to search for data fusion opportunities, such as determining the elastic properties and hence the ultrasonic velocity of the material from thermal wave or surface wave measurements so that the actual thickness of the material can be determined from the ultrasonic echoes.

A comprehensive model of the inspection process will also demonstrate where the experimental configuration should be enhanced. Obvious enhancements include increasing the chopping frequency of the heating beam to reduce thermal wave signals, using frequency doubled light to double the sensitivity of the interferometer, and using a high speed delay line.

REFERENCES

Auld, B.A., *Acoustic Fields and Waves in Solids*, Vol. 2., Sydney, John Wiley and Sons, (1973).

Batz, B., "Reflectance Modulation at a Germanium Surface." *Solid State Communications* **4** (5) 241-243 (1966).

Bolz, R.E & Tuve, G.L., *Handbook of Tables for Applied Engineering Science*, Second ed., CRC Press Cleveland, Ohio, (1973).

Born, M. & Wolf, E., *Principles of Optics*, 4th ed., Pergamon Press, London (1970) 615-624.

Cardona, M., *Modulation Spectroscopy*, Academic Press, New York (1969), 117-136.

Carslaw, H.S. & Jaeger, J.C., *Conduction of Heat in Solids*, Second ed. Oxford Press, London, (1959).

Chapman, A.J., *Heat Transfer*, Fourth ed., Macmillan Publishing, New York (1984).

Chimenti, D.E. & Crane, R.L., *Elastic Wave Propagation Through Multilayered Media.*, Air Force Materials Laboratory, Dayton (1979).

Demczyk, B. G., Garfunkel, E. & Clemens, B. M., *Evolution of Thin Film and Surface Structure and Morphology*, Materials Research Society, (1994).

Eckertova, L., *Physics of Thin Films*, Plenum, London, (1986).

Eesley, G.L., Clemens, B.M. & Paddock,C.A., "Generation and Detection of Picosecond Pulses in Thin Metal Films." *Applied Physics Letters* **50** (12) 717-719 (1987).

Engeler, W.E., Fritzsche, H., Garfinkel, M. & Tiemann, J.J., "High-Sensitivity Piezoreflectivity" *Physical Review Letters* **14** (26) 1069-1072 (1965).

Feldman, A., "Piezo-Optical Effects in Solids by Sample Rotation." *Physics Letters* **23** (12) 627-628 (1966).

Gerhardt, U., Beaglehole, D. & Sandrock, R., "Piezo-Optical Constants, Deformation Potentials, and the Electronic Structure of Copper.", *Physical Review Letters* **19** (6) 309-311 (1967).

Gobeli, G.W. & Kane, E.O., "Dependence of the Optical Constants of Silicon on Uniaxial Stress." *Physical Review Letters* **15** (4) 142-146 (1965).

Grahn, H.T., Maris,H.J., Tauc, J. & Hatton, K.S., "Elastic Properties of Silicon Oxynitride Films Determined by Picosecond Acoustics." *Applied Physics Letters* **53** (23) 2281-2283 (1988).

Grahn, H.T., Young, D.A., Maris, H.J., Tauc, J., Hong, J.M., & Smith, T.P., "Sound Velocity and Index of Refraction of AlAs Measured by Picosecond Ultrasonics." *Applied Physics Letters* **53** (21) 2023-2024 (1988).

Grahn, H.T., Maris, H.J. & Tauc, J., "Time Resolved Study of Vibrations of a-Ge:H/a-Si:H Multilayers." *Physical Review B* **38** (9) 6066 (1988) .

Gray,D.E., *American Institute of Physics Handbook.*, 3rd ed., McGraw-Hill, New York, (1972).

Heavens,*Thin Film Physics*, Methuen & Co, London (1970).

Kakac, S. & Yener, Y., *Heat Conduction.*, Third ed. Taylor and Francis, Washington DC, (1993).

Kittel, C., *Introduction to Solid State Physics*, Sixth ed. Singapore, John Wiley & Sons, (1986).

Kressel, H., *Characterization of Epitaxial Semiconductor Films*, Elsevier Scientific, New York, (1976).

Lin, H. N., Stoner,R.J., Maris,H.J. & Tauc,J., "Phonon Attenuation and Velocity Measurements in Transparent Materials by Picosecond Acoustic Interferometry." *Journal of Applied Physics* **69** (7) 3816-3822 (1991).

Lin, H.N., Stoner,R.J., & Maris,H.J., "Ultrasonic Experiments at Ultra-High Frequency with Picosecond Time-Resolution." *Ultrasonics Symposium* 1301-1307 (1990).

McKie, D.W. & Addison, R.C., "A Laser-Based Ultrasound System Incorporating a Long Pulse Probe Laser for Increased Sensitivity." *Review of Progress in Quantitative Nondestructive Evaluation.* Ed. Thomson, D.O & Chimenti, D.E., Plenum,New York, (1994) Vol. 13.

Ozisik, M.N., *Heat Conduction*, Wiley and Sons, Brisbane (1980).

Paddock, C.A., & Eesley,G.L., "Transient Thermoreflectance from Thin Metal Films." *Journal of Applied Physics* **60** (1) 285-290 (1986).

Pease,J., "Phone conversation.", Palo Alto Research Corporation, (1994).

Rosencwaig.A, *Photoacoustics and Photoacoustic Spectroscopy*, Wiley & Sons,Toronto, (1980).

Rosencwaig, A., Opsal,J., Smith,W.L, & Willenborg, D.L. "Detection of Thermal Waves Through Optical Reflectance." *Appl Phys Lett* **46** (11) 1013-1015 (1985).

Rosencwaig, A. & Busse, G., "High Resolution Photoacoustic Thermal-wave Microscopy." *Appl. Phys. Lett* **36** (9) 725-727 (1980).

Scruby, C.B. & Drain L.E., *Laser Ultrasonics: Techniques and Applications*, Adam Hilger,Bristol, (1990).

Spicer, J.B., "Phone Conversation." Johns Hopkins University, (1996).

Stoner, R.J., Maris, H.J., Anthony, T.R. & Banholzer, W.F., "Measurements of the Kapitza Conductance between Diamond and Several Metals." *Physical Review Letters* **68** (9) 1563-1566 (1992).

Tas,G., Stoner,R.J., Maris, H.J., Rubloff, G.W., Oehrlein, G.S. & Halbout, J.M., "Noninvasive Picosecond Ultrasonic Detection of Ultrathin Interfacial Layers: CFx at the Al/Si Interface." *Applied Physics Letters* **61** (15) 1787-1789 (1992).

Thomsen, C., Grahn,H.T., Maris, H.J. & Tauc, J., "Picosecond Interferometric Technique for the Study of Phonons in the Brillouin Frequency Range." *Optics Communications* **60** (1) 55-58 (1986).

Thomsen, C., Grahn, H.T., Maris, H.J. & Tauc, J., "Surface Generation and Detection of Phonons by Picosecond Light Pulses." *Physical Review B* **34** (6) 4129 (1986).

Verdeyen, J.T., *Laser Electronics*, Prentice-Hall Inc, New York (1981) 75-76.

Wagner, J.W., "Optical Detection of Ultrasound." *Physical Acoustics*. Ed. W.P. Mason. Academic Press,Toronto, (1990) 201-266. Vol. 19.

Wright, O.B., "Thickness and Sound Velocity Measurement in Thin Transparent Films with Laser Picosecond Acoustics." *Journal of Applied Physics* **71** (4) 1617-1628 (1992).

Wright, O.B. & Hyoguchi, T., "Ultrafast Vibration and Laser Acoustics in Thin Transparent Films." *Optics Letters* **16** (19) 1529-1531 (1991).

Wright, O.B., Hyoguchi, T. & Kawashima, K., "Laser Picosecond Acoustics in Thin Films: Effect of Elastic Boundary Conditions on Pulse Generation." *Japanese Journal of Applied Physics* **30** (1) L131-L133 (1991).

VITA

Curtis Jon Fiedler was born on March 28, 1960 in Brookings, South Dakota. He received a Bachelor of Science degree in Engineering Science in 1982 from Iowa State University at Ames, Iowa. During 1982 and 1983 he developed techniques to quantify crack closure at the Ames Laboratory. Curtis earned a Master of Science degree in Engineering Mechanics from The Ohio State University, Columbus, Ohio in 1985 and developed a ray tracing simulation of ultrasound for the Center for Welding Research. Since 1986 he has conducted research for the Nondestructive Evaluation Branch, Wright-Patterson Materials Directorate, US Air Force in Dayton, Ohio as a Materials Research Engineer. While working for the Air Force he also studied nondestructive evaluation in the Department of Materials Science and Engineering at The Johns Hopkins University, Baltimore, Maryland starting in 1989.